

## MALS SALT-NOT survey of MIR-selected powerful radio-bright AGN at $0 < z < 3.5$

N. GUPTA,<sup>1</sup> G. SHUKLA,<sup>1</sup> R. SRIANAND,<sup>1</sup> J.-K. KROGAGER,<sup>2</sup> P. NOTERDAEME,<sup>2</sup> A. J. BAKER,<sup>3</sup> F. COMBES,<sup>4</sup> J. P. U. FYNBO,<sup>5,6</sup> E. MOMJIAN,<sup>7</sup> M. HILTON,<sup>8</sup> T. HUSSAIN,<sup>1</sup> K. MOODLEY,<sup>8</sup> P. PETITJEAN,<sup>2</sup> H.-W. CHEN,<sup>9</sup> P. DEKA,<sup>1</sup> R. DUTTA,<sup>10</sup> J. JOSE,<sup>11</sup> G. I. G. JÓZSA,<sup>12,13,14</sup> C. KASKI,<sup>11</sup> H.-R. KLÖCKNER,<sup>15</sup> K. KNOWLES,<sup>16</sup> S. SIKHOSANA,<sup>16</sup> AND J. WAGENVELD<sup>15</sup>

<sup>1</sup>*Inter-University Centre for Astronomy and Astrophysics, Post Bag 4, Ganeshkhind, Pune 411 007, India*

<sup>2</sup>*Institut d'Astrophysique de Paris, UMR 7095, CNRS-SU, 98bis bd Arago, 75014 Paris, France*

<sup>3</sup>*Department of Physics and Astronomy, Rutgers, the State University of New Jersey, 136 Frelinghuysen Road, Piscataway, NJ 08854-8019, USA*

<sup>4</sup>*Observatoire de Paris, Collège de France, PSL University, Sorbonne University, CNRS, LERMA, Paris, France*

<sup>5</sup>*Cosmic Dawn Center (DAWN), University of Copenhagen, Jagtvej 128, DK-2200, Copenhagen N, Denmark*

<sup>6</sup>*Niels Bohr Institute, University of Copenhagen, Jagtvej 128, DK-2200, Copenhagen N, Denmark*

<sup>7</sup>*National Radio Astronomy Observatory, P.O. Box O, Socorro, NM 87801, USA*

<sup>8</sup>*Astrophysics Research Centre and School of Mathematics, Statistics and Computer Science, University of KwaZulu-Natal, Durban 4041, South Africa*

<sup>9</sup>*Department of Astronomy & Astrophysics, The University of Chicago, 5640 S Ellis Ave., Chicago, IL 60637, USA*

<sup>10</sup>*Dipartimento di Fisica G. Occhialini, Università degli Studi di Milano Bicocca, Piazza della Scienza 3, 20126 Milano, Italy*

<sup>11</sup>*ThoughtWorks Technologies India Private Limited, Yerawada, Pune 411 006, India*

<sup>12</sup>*South African Radio Astronomy Observatory, 2 Fir Street, Black River Park, Observatory 7925, South Africa*

<sup>13</sup>*Department of Physics and Electronics, Rhodes University, P.O. Box 94, Makhanda, 6140, South Africa*

<sup>14</sup>*Argelander-Institut für Astronomie, Auf dem Hügel 71, D-53121 Bonn, Germany*

<sup>15</sup>*Max-Planck-Institut für Radioastronomie, Auf dem Hügel 69, D-53121 Bonn, Germany*

<sup>16</sup>*Astrophysics Research Centre and School of Mathematics, Statistics and Computer Science, University of KwaZulu-Natal, Durban 4041, South Africa*

Submitted to ApJ

## ABSTRACT

We present results of an optical spectroscopic survey using SALT and NOT to build a WISE mid-infrared color-based, dust-unbiased sample of powerful radio-bright ( $>200$  mJy at 1.4 GHz) AGN for the MeerKAT Absorption Line Survey (MALS). Our sample has 250 AGN (median  $z = 1.8$ ) showing emission lines, 26 with no emission lines, and 27 without optical counterparts. Overall, our sample is fainter ( $\Delta i=0.6$  mag) and redder ( $\Delta(g-i)=0.2$  mag) than radio-selected quasars, and representative of fainter quasar population detected in optical surveys. About 20% of the sources are narrow line AGN (NLAGN) – 65% of these, at  $z < 0.5$  are galaxies without strong nuclear emission, and 10% at  $z > 1.9$ , have emission line ratios similar to radio galaxies. The farthest NLAGN in our sample is M1513–2524 ( $z_{em} = 3.132$ ), and the largest radio source (size $\sim$ 330 kpc) is M0909–3133 ( $z_{em} = 0.884$ ). We discuss in detail 110 AGN at  $1.9 < z < 3.5$ . Despite representing the radio loudest quasars (median  $R=3685$ ), their Eddington ratios are similar to the SDSS quasars having lower  $R$ . We detect 4 C IV BALQSOs, all among AGN with least  $R$ , and highest black hole masses and Eddington ratios. The BAL detection rate ( $4^{+3}_{-2}\%$ ) is consistent with that seen in extremely powerful ( $L_{1.4\text{GHz}} > 10^{25}$  W Hz $^{-1}$ ) quasars. Using optical light-curves, radio polarization and  $\gamma$ -ray detections, we identify 7 high-probability BL Lacs. We also summarize the full MALS footprint to search for H I 21-cm and OH 18-cm lines at  $z < 2$ .

*Keywords:* quasars: absorption lines — interstellar medium

## 1. INTRODUCTION

Active Galactic Nuclei (AGN) radiate across the entire electromagnetic spectrum but in their early phases of evolution the thermal emission from the accretion disk especially at UV to optical wavelengths can be obscured by the dusty material fueling the central engine. Subsequently, as the radiative and mechanical feedback clears the obscuring material the central AGN can become observable as optically selected AGN (e.g., Sanders & Mirabel 1996). The direct view of the accretion disk may also be blocked by a dusty ‘torus’ which has been postulated to explain the appearances of different types of AGN through orientation-based unification schemes (e.g., Urry & Padovani 1995). In this paradigm, type I and type II AGN appear different merely due to varying amounts of dust along the observer’s line of sight. The redder AGN are then more obscured simply because they are being viewed at inclinations closer to the equatorial plane of the torus.

In principle, AGN can also be obscured by dust from high-column density H I absorbers such as damped Ly $\alpha$  systems (DLAs), which are defined to have  $N(\text{H I}) > 2 \times 10^{20} \text{ cm}^{-2}$  (Wolfe & Prochaska 2000) and associated with intervening galaxies intercepting the line of sight. Despite the availability of large samples of intervening DLAs (e.g., Noterdaeme et al. 2009; Parks et al. 2018) and the fact that they trace the bulk of neutral hydrogen in the Universe (Wolfe et al. 2005), the detected DLAs show little dust (e.g. Murphy & Liske 2004) and only a small fraction exhibit the presence of molecular hydrogen (Petitjean et al. 2000; Ledoux et al. 2003; Noterdaeme et al. 2008; Srianand et al. 2012; Noterdaeme et al. 2015; Muzahid et al. 2015; Balashev & Noterdaeme 2018; Zahedy et al. 2020; Boettcher et al. 2021).

Interestingly, none of the DLAs detected to date have properties similar to dense molecular clouds in the Galaxy. In fact, PKS 1830-211 which exhibits extreme reddening (visual extinction,  $A_V > 5.8$ ; Mathur & Nair 1997) due to an intervening absorber at  $z = 0.89$  with properties similar to dense molecular clouds, was identified on the basis of its peculiar radio spectrum and morphology (Pramesh Rao & Subrahmanyan 1988; Jauncey et al. 1991). The redshift  $z = 0.89$  of the lensing galaxy responsible for the intervening absorption was discovered through a spectroscopically blind search of molecular absorption at millimeter wavelengths (Wiklind & Combes 1996). A dust-unbiased census of DLAs is required to correctly estimate the key observables such as H I and metal mass densities of the Universe, and the extent of dust-obscured AGN missed in UV-optical colour based surveys (e.g., Pei et al. 1991; Srianand & Kemb-

havi 1997; Ellison et al. 2001; Pontzen & Pettini 2009; Frank & Péroux 2010; Krogager et al. 2019).

Regardless of the origin of obscuration, it is desirable to build dust-unbiased samples of AGN to distinguish between competing paradigms based on evolution or orientation to understand the AGN population itself and its impact on galaxy evolution via feedback (e.g., Fabian 2012; Heckman & Best 2014). The most effective techniques to achieve this are naturally based on photometric selection at hard X-ray, mid-infrared (MIR) or radio wavelengths. In recent years the AllWISE catalog from the Wide-field Infrared Survey Explorer (WISE; Wright et al. 2010; Cutri & et al. 2014) in its four bands, namely  $W_1$  ( $3.4 \mu\text{m}$ ),  $W_2$  ( $4.6 \mu\text{m}$ ),  $W_3$  ( $12 \mu\text{m}$ ), and  $W_4$  ( $22 \mu\text{m}$ ), has emerged as an excellent resource to identify obscured AGN across the full sky. The  $5\sigma$  point-source sensitivities of the WISE All-Sky release in the four bands in Vega-based magnitudes are 16.83, 15.60, 11.32 and 8.0, respectively.

The MIR selection of AGN works exactly in the same manner as the traditional optical color selection except that it is less susceptible to dust extinction. The near-IR spectrum of an AGN is simply an extension of the UV-optical power law. The MIR and longer wavelength IR emission comes from the hot dust in the ‘torus’ which absorbs UV-optical emission and reprocesses it (Netzer et al. 2007). All these give rise to a power law spectrum which dominates at wavelengths longer than  $\sim 1 \mu\text{m}$  and is easily distinguishable from a declining Rayleigh-Jeans spectrum of galaxies and stars in MIR color space up to  $z \sim 3$ . Thus, the MIR color selection can potentially detect obscured AGN missed in UV-optical and even X-ray selections over a wide redshift range (e.g., Lacy et al. 2004; Stern et al. 2005; Mateos et al. 2012; Stern et al. 2012).

Taking advantage of the segregation of various classes of objects i.e., stars, early-type and spiral galaxies, brown dwarfs and AGN in the WISE color space (see Fig. 12 of Wright et al. 2010), several AGN identification techniques based on the ALLWISE data release have been proposed in the literature. The majority of these are based on the  $W_1$  and  $W_2$  i.e., the two most sensitive bands of WISE (see Assef et al. 2018, for a large all sky catalog of AGN), and have been shown to yield AGN space density much higher than those from the optical and X-ray surveys (Stern et al. 2005; Assef et al. 2010). The MIR colors corresponding to *Fermi* detected AGN have been used to build large samples ( $\sim 15,000$ ) of blazars (D’Abrusco et al. 2019). The MIR color diagnostic has also been applied to identify dual AGN candidates which represent a crucial and rare stage in the galaxy evolution (e.g., Satyapal et al. 2017).

In this paper, we present a MIR-color scheme based on  $W1$ ,  $W2$  and  $W3$  that efficiently selects quasars at  $z > 1.4$ . We have also carried out a large spectroscopic campaign using the Nordic Optical Telescope (NOT) and the Southern African Large Telescope (SALT) to measure the redshifts and confirm the nature of a subset of AGN candidates identified using our MIR-color scheme. The NOT component of the survey has already been presented by Krogager et al. (2018). Here we present the complete SALT–NOT catalog of the 303 AGN at  $0 < z < 3.5$  that constitutes radio sources brighter than 200 mJy at  $\sim 1.4$  GHz in the NRAO VLA Sky Survey (NVSS; Condon et al. 1998) and at declination,  $\delta < +20^\circ$ .

The SALT-NOT sample represents a small minority of AGN that are extremely powerful in radio with 1.4 GHz spectral luminosity,  $L_{1.4\text{GHz}} > 10^{24} \text{ W Hz}^{-1}$ . In past many studies have attempted to isolate the physical mechanisms responsible for the quasar radio-loudness dichotomy. The massive black holes (BHs) in radio loud AGN are found to be systematically a few times heavier than those in their radio quiet counterparts (e.g., Laor 2000). A further interesting trend that has emerged from these studies is the anti-correlation between the Eddington ratio and radio loudness (e.g., Sikora et al. 2007). The physical parameters such as BH mass, spin and accretion rate along with the in situ magnetic field are believed to determine the extent of radio loudness and overall appearance of the AGN (e.g., Sikora & Begelman 2013). The SALT-NOT sample offers an opportunity to revisit these issues for extremely radio loud quasars selected through MIR colors.

This paper is organized as follows. In Section 2, we present details of radio-infrared-optical cross-matching to select candidates for the SALT-NOT survey and the sample selection criteria. The latter is based on the requirements of the MeerKAT Absorption Line Survey (MALS; see Gupta et al. 2017, for key science objectives), an ongoing large survey at the South African precursor (Jonas & MeerKAT Team 2016) of the upcoming Square Kilometer Array (SKA). In Section 3, we present the details of SALT observations and data analysis. These details for the NOT component of the survey are available in Krogager et al. (2018). The details of emission line identification, redshift measurement and AGN classifications based on the SALT-NOT spectra are provided in Section 4. Section 5 presents selected results based on radio continuum and optical emission line properties. For AGN at  $1.9 < z < 3.5$ , we also estimate BH masses, accretion rates and the occurrence of broad absorption lines, and revisit the issue of their dependence on radio loudness. We also discuss emission

line less AGN with highest optical photometric variability and the targets with no optical counterparts. Finally, in Section 6 we summarize the results and complement the SALT-NOT catalog with AGN from the literature to assemble a target list of  $\sim 650$  AGN defining the MALS footprint to search for cold atomic and molecular gas at  $z < 2$ .

Throughout this paper we use the  $\Lambda$ CDM cosmology with  $\Omega_m=0.315$ ,  $\Omega_\Lambda=0.685$  and  $H_0=67.4 \text{ km s}^{-1} \text{ Mpc}^{-1}$  (Planck Collaboration et al. 2020).

## 2. SAMPLE SELECTION

The SALT-NOT sample definition is based on the requirements of MALS. MALS is using MeerKAT’s L and UHF bands covering 900–1670 and 580–1015 MHz to carry out a sensitive search for H I 21-cm (OH 18-cm) absorbers at  $0 \leq z \lesssim 0.6$  ( $0 \leq z \lesssim 0.9$ ) and  $0.4 \lesssim z \lesssim 1.4$  ( $0.6 \lesssim z \lesssim 1.9$ ), respectively (see Gupta et al. 2017, for key science objectives). In order to ensure reasonable observability with the MeerKAT telescope located in South Africa, the majority of MALS pointings will be at  $\delta < +20^\circ$ . The survey is well underway and the first L- and UHF-band spectra based on the science verification data are presented in Gupta et al. (2021a) and Combes et al. (2021), respectively.

Each MALS pointing is centered at a radio source brighter than 200 mJy at  $\sim 1$  GHz. For L-band we require these bright AGN to be at  $z > 0.6$  whereas for the UHF-band all must be at  $z > 0.4$  and a significant fraction at  $z > 1.4$ , i.e., the H I 21-cm line redshift corresponding to the lower frequency edge of the band.

Since dust bias can be very significant towards sight lines with cold atomic and molecular gas, it is also desirable that the central targets for MALS are selected without any bias towards dust extinction. Thus, to efficiently identify quasars that can be used for both the L- and UHF-bands we have developed a selection scheme optimized to identify  $z > 1.4$  quasars based primarily on MIR colors from the AllWISE catalog. The WISE color space of radio sources identified as quasars in the SDSS spectroscopic catalog is presented in Fig. 2 of Krogager et al. (2018). This figure shows that low- and high- $z$  quasars are separated in  $W1$ ,  $W2$  and  $W3$  color space, and the following color cuts:

$$W1 - W2 < 1.3 \times (W2 - W3) - 3.04; \\ W1 - W2 > 0.6, \quad (1)$$

can be used to efficiently select high- $z$  quasars.

To summarize, SALT-NOT sample is based on the following three criteria: (i) flux density  $> 200$  mJy at  $\sim 1$  GHz, (ii)  $\delta < +20^\circ$ , and (iii) MIR colors consistent

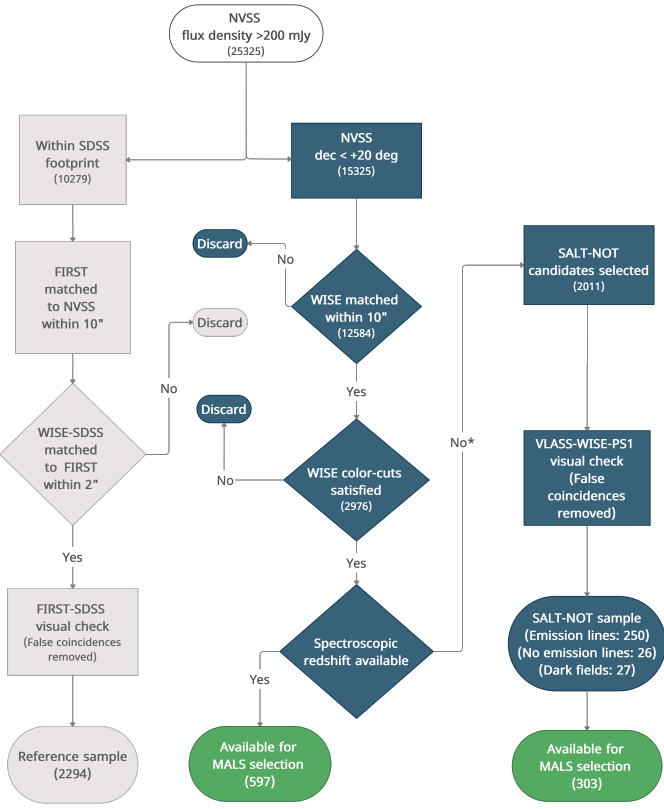


**Figure 1.** Schematic illustration of the selection process for the quasar *reference* sample and SALT–NOT targets. The numbers refer to sources at each step. The ‘\*’ indicates that a handful of targets with spectra in SDSS were included in the SALT–NOT survey to verify our selection and observational strategy. See Sect. 4 for more details.

with Equation 1. The last condition requires that the object is detected in the first three WISE bands. Note that only  $\sim 10\%$  of 747 million objects are detected in all three bands. We revisit the efficacy of the MIR-color selection scheme in subsequent sections.

### 2.1. Cross-matching and reference sample

Cross-matching multi-wavelength datasets poses multiple challenges. Firstly, not all objects may be detected in all the datasets. Secondly, due to different spatial resolutions of datasets, an object in one dataset may have multiple counterparts in the other. This is particularly relevant for radio sources which often display extended emission made up of components such as core, jets and lobes. Depending on the frequency the strongest radio component may be far away from the optical or IR counterpart. For reliable cross-matching it is desirable to have radio data with a spatial resolution of few arcseconds or better.

Another major challenge is that each selection method has its own systematics. For quasars, it is quite possible that selections using different methods may lead to objects with different characteristics such as different Eddington ratios, clustering properties and host galaxy masses. The selected quasars may then be intrinsically different, therefore comparison with samples from other selection approaches ought to be done with caution.

Concerning our sample definition, only<sup>1</sup> the NRAO VLA Sky Survey (NVSS; Condon et al. 1998) and the Sydney University Molonglo Sky Survey (SUMSS; Mauch et al. 2003) at 1.4 GHz and 0.843 GHz, respectively, have the sensitivity, positional accuracy and the sky coverage required to perform cross-matching with the AllWISE catalog (Cutri & et al. 2014) at MIR wavelengths. But the spatial resolution offered by NVSS is typically  $45''$ . In comparison, the angular resolutions in the four WISE bands are  $6.1'', 6.4'', 6.5'',$  and  $12.0''$ , respectively. The coarse resolution at radio wavelength might then lead to a bias against extended lobe-dominated quasars: either they will be assigned a wrong WISE counterpart or completely missed. To quantify the impact of this and the other above-mentioned challenges in our selection process, we start with constructing a *reference* sample.

The process of building the *reference* sample is shown in Fig. 1. We start with NVSS which has 25,325 radio sources brighter than 200 mJy at 1.4 GHz and  $\delta > -40^\circ$ . We use optical data from SDSS and higher spatial resolution (i.e.  $\sim 5''$ ) radio data from the Faint Images of the Radio Sky at Twenty-Centimeters (FIRST; Becker et al. 1995) to examine our selection process. The FIRST survey has observed  $\sim 10,000$  square degrees of the North and South Galactic Caps at 1.4 GHz, which overlaps very well with the SDSS sky coverage. These two surveys provide the best available radio-optical data covering a large area of the sky. Since the bulk of FIRST-SDSS coverage is at positive declination, we do not apply any declination cuts to the *reference* sample.

We cross-match 10,279 NVSS sources which are within the SDSS footprint with FIRST. We adopt a search radius of  $30''$ . Since FIRST has a spatial resolution of  $5''$  and positional accuracy of  $0.1''$ , it will allow us to identify the resolved radio source components associated with the NVSS sources. Next, we cross-match FIRST radio source components with SDSS (DR14 photometry) and AllWISE catalogs to identify the closest match. Note that we require a valid WISE match to have detec-

<sup>1</sup> The Rapid ASKAP Continuum Survey (McConnell et al. 2020) was unavailable at the time of planning this project.

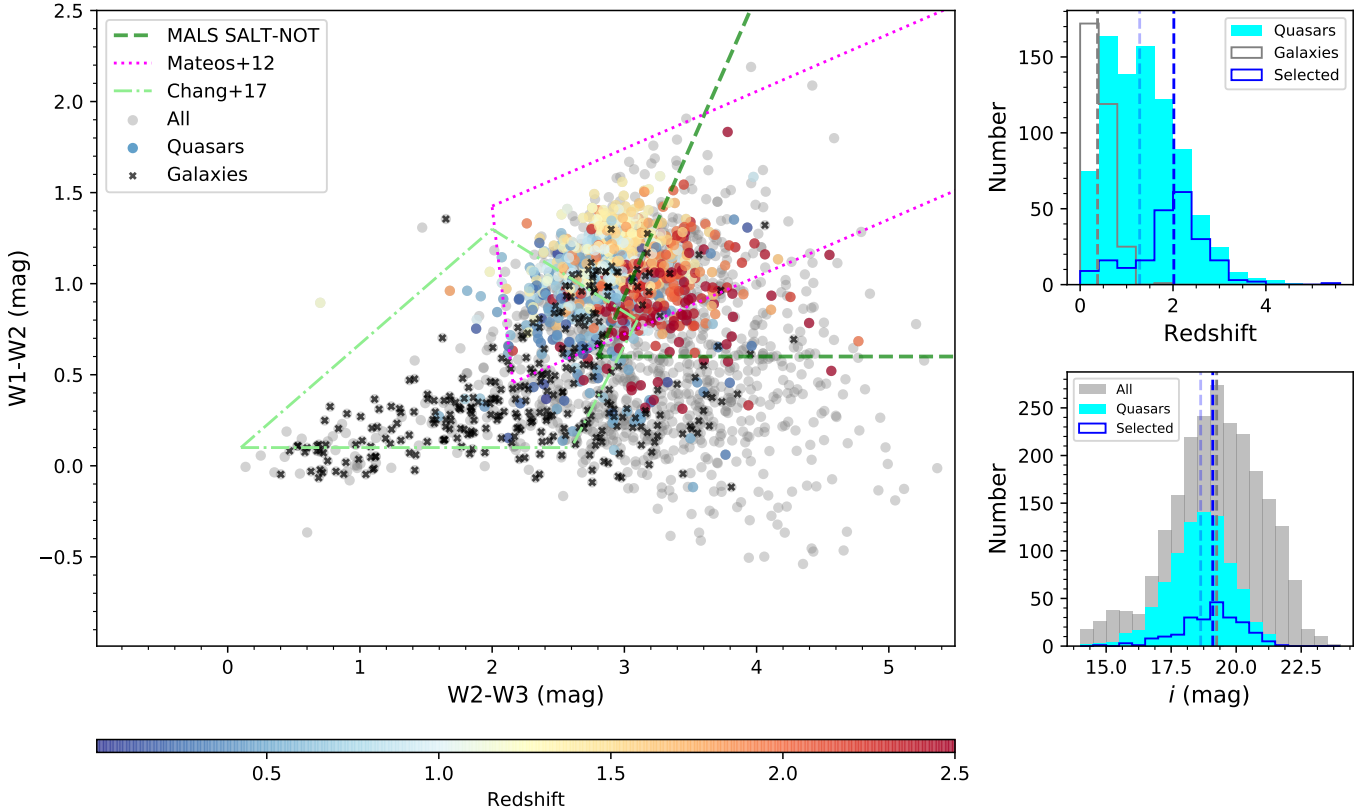


**Figure 2.** Left: WISE color-color plot in Vega magnitudes for radio bright sources in the quasar *reference* sample. Sources with known spectroscopic redshifts are color-coded according to redshift. The AGN wedges of Mateos et al. (2012), Chang et al. (2017) and our SALT-NOT criteria are shown using dotted, dash-dotted and dashed lines, respectively. Right, top panel: Redshift distributions of quasars, galaxies and WISE-selected quasars (i.e., quasars satisfying SALT-NOT WISE color cuts). Right, bottom panel: Distributions of SDSS  $i$ -band AB magnitude for all sources, quasars and WISE-selected quasars are shown. The vertical dashed lines indicate the median for each distribution. Note that SDSS  $5\sigma$  depth for the  $i$ -band is 22.2 mag.

tions in all three bands, i.e.,  $W1$ ,  $W2$  and  $W3$ . For this we adopt a search radius of  $2''$ , which has been shown to provide a good compromise between completeness and random association for FIRST–SDSS quasars (e.g., Lu et al. 2007). We visually examined all 2327 FIRST–SDSS associations using the FIRST and SDSS  $i$ -band images, and excluded: (i) 8 unreal radio source components: these are due to an artefact in the FIRST image; and (ii) 12 radio sources with complex morphology: for these it is not possible to reliably assign an optical–MIR counterpart to the radio source. Spectra of 1164 sources are available in SDSS. We inspect these and reject 13 cases with false spectral line identifications. Finally, we have a *reference* sample of 2294 sources from NVSS, with WISE detections in  $W1$ ,  $W2$  and  $W3$  bands, and cross-matching further refined by FIRST and SDSS.

The WISE colors of the *reference* sample are shown in the *left* panel of Fig. 2. Among 1151 reference sample sources with SDSS spectra, 834 are identified as quasars and 317 as galaxies. Clearly, as expected the majority of radio bright quasars have red  $W1 - W2$  colors. Only

beyond  $z \sim 3$ , the rest frame  $1\,\mu\text{m}$  minimum would shift into the  $W2$  band causing the color to turn blue (see Stern et al. 2012). But for high- $z$  quasars this can be compensated by even small amounts of dust, allowing the method based only on  $W1 - W2$  color to perform rather well even at high redshifts. However, significant host galaxy contribution can also turn  $W1 - W2$  blue. In the figure, we show the color wedge of Mateos et al. (2012) defined based on X-ray selected AGN. The additional constraint based on  $W2 - W3$  allows the wedge of Mateos et al. (2012, also see their Fig. 5) to efficiently identify AGN as long as the host galaxy contribution is less than 20%. Indeed the wedge efficiently identifies the bulk of powerful *reference* quasars.

In Fig. 2, we also demarcate the region corresponding to Equation 1. The redshift and  $i$ -band magnitude distributions of the reference sample are shown in the *right* panels of Fig. 2. The median redshift and  $i$ -band magnitude are 0.9 and 18.6 mag, respectively. If we consider only quasars, these values are 1.3 and 18.6 mag, respectively. For quasars within our MIR-wedge these values

are 2.0 and 19.1 mag, respectively (see vertical dashed lines in Fig. 2). Also, within the wedge the fraction of AGN classified as quasars increases to  $94\pm6\%$  (214/228) whereas for the full sample it is  $73\pm3\%$  (834/1151). The fraction of  $z > 1.4$  quasars also increases from 30% (full sample) to 75% (within the wedge). Thus, our MIR-wedge preferentially selects more powerful and higher redshift quasars.

## 2.2. SALT-NOT candidate sample

The process of identifying candidates for SALT-NOT survey is shown in Fig. 1. We start with 25,325 sources brighter than 200 mJy in NVSS but first restrict ourselves to 15,325 at  $\delta < +20^\circ$  and then to 12,584 with WISE matches within  $10''$ . Since we use NVSS all the candidates are at  $\delta > -40^\circ$ . Next we consider only 2976 sources that satisfy our WISE-color cuts. Of these, 597 sources ( $\sim 340$  at  $z > 1.4$ ) have spectroscopic redshifts from the literature<sup>2</sup>, and will be used later for MALS target selection (see Section 6). For the SALT-NOT survey, we exclude these and consider the remaining 2011 radio sources which have a high probability of being a quasar at  $z > 1.4$ .

Next, targets were drawn from the pool of 2011 candidates to fill the allocated and observable local sidereal time (LST) ranges at the NOT and SALT locations. The final sample of 303 candidates which could be observed in the allocated time is presented in Table 3. The sample has been subjected to visual checks using the quick look radio images at 2–4 GHz from the Very Large Array Sky Survey (VLASS; Lacy et al. 2020). These quick look images have a spatial resolution of  $\sim 2.5''$  but are not the final data products meeting the overall survey requirements. The positional accuracy is limited to  $\sim 0.5''$ . Therefore, we used these images only to verify the coincidence between the MIR source and the radio peak. In the cases where a VLASS image was unavailable or not of reasonable quality, the corresponding candidate was assigned a lower priority. Following the process described in Sect. 2.1, we have rejected dubious coincidences which primarily meant rejecting sources with complex radio morphologies. It was straightforward to verify and accept the compact radio sources (i.e., single component in VLASS), and indeed our overall selection process preferentially picks quasars associated with compact radio emission. But wherever possible we also included targets with clear core-jet or compact symmetric object (CSO) type morphology. In both these cases it is possible to identify the location of MIR/optical AGN.

<sup>2</sup> Nasa/IPAC Extragalactic Database (NED) and the Million Quasars (Milliquas) Catalog v4.0

The details of radio structure of AGN observed with SALT-NOT are presented in Sect. 5.

For candidates at  $\delta > -30^\circ$ , we have also examined the *i*-band images from the Panoramic Survey Telescope and Rapid Response System (PanSTARRS; Chambers et al. 2016) by considering the nearest match within  $2''$ . Ideally, in the pursuit of dust-obscured quasars one does not include any criteria based on optical wavelengths. Therefore, we limited the majority of our targets to those that could be successfully observed with SALT and NOT in a modest amount of observing time but included a small ( $\sim 10\%$ ) fraction with very faint ( $i > 22$  mag) optical counterparts. Note that in Table 3 we have excluded 7 targets (list provided in the notes to Table 3) from the NOT sample presented in table 1 of Krogager et al. (2018). The VLASS-WISE-PS1 visual check revealed that the lack of spectroscopic outcome in these cases is due to the misidentification of the optical/IR source associated with the radio source. Such misidentifications have already been removed from the sample for the SALT component.

The sample presented in Table 3 is split into three categories: (i) with emission lines in the optical spectrum (250 objects), (ii) with no emission lines in the optical spectrum i.e., emission line less (ELLs; 26), and (iii) dark fields (DFs; 27) i.e., neither emission line nor a continuum source in optical spectra and images, respectively despite being detected in WISE images. The distributions of 1.4 GHz flux density,  $W1$  and *i*-band magnitudes are shown in Fig. 3. Further details and comparison with the *reference* sample are provided in subsequent sections.

## 2.3. Efficacy of selection process

As previously mentioned, our target selection process is optimized for identifying powerful quasars at  $z > 1.4$ . We have therefore included a set of criteria on the WISE photometry (see Eq. 1). The mere fact that we require detections in all three WISE bands might introduce a bias in the resulting quasar sample, and the subsequent color criteria might further affect their optical properties. In this section, we aim to quantify any such selection effects.

For this purpose, we compile a highly complete spectroscopic sample of 10,498 quasars from the SDSS (DR16) in the so-called ‘Stripe 82’ region where the spectroscopic completeness is the highest in SDSS. We then cross-match this sample with the AllWISE catalog to produce our optical comparison sample. We note that although no radio flux density limits have been applied here, only 347/10,498 are detected in FIRST,

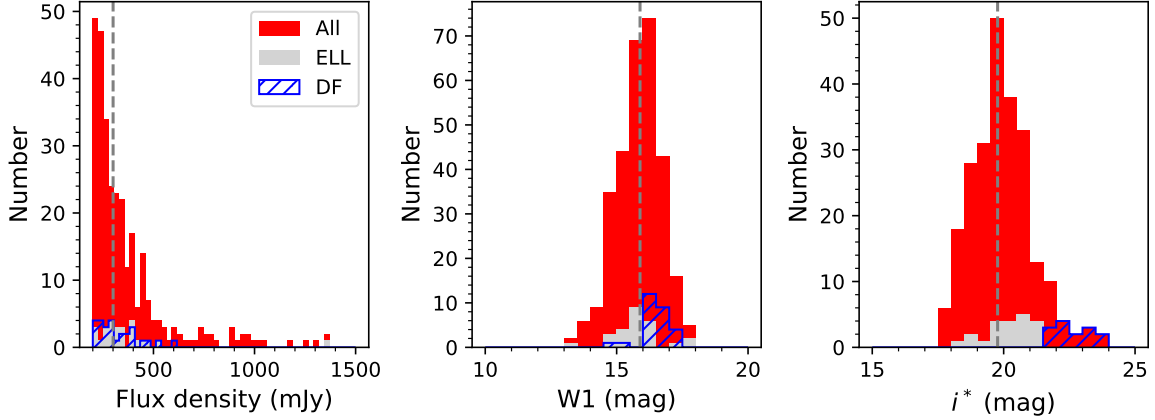


**Figure 3.** Distribution of flux density at 1.4 GHz,  $W_1$  and  $i$ -mag for our MIR selected sample. The gray and blue-hashed distributions show objects with no clear emission lines (emission line less, ELL) and objects with no detected spectrum (dark field, DF), respectively. The vertical dashed lines mark the median for all the sources in each panel. In the first panel, four targets brighter than 1500 mJy are out of frame. Note that for DFs, the  $i$ -band magnitudes are from the more sensitive PS1 stack catalog (Waters et al. 2020).

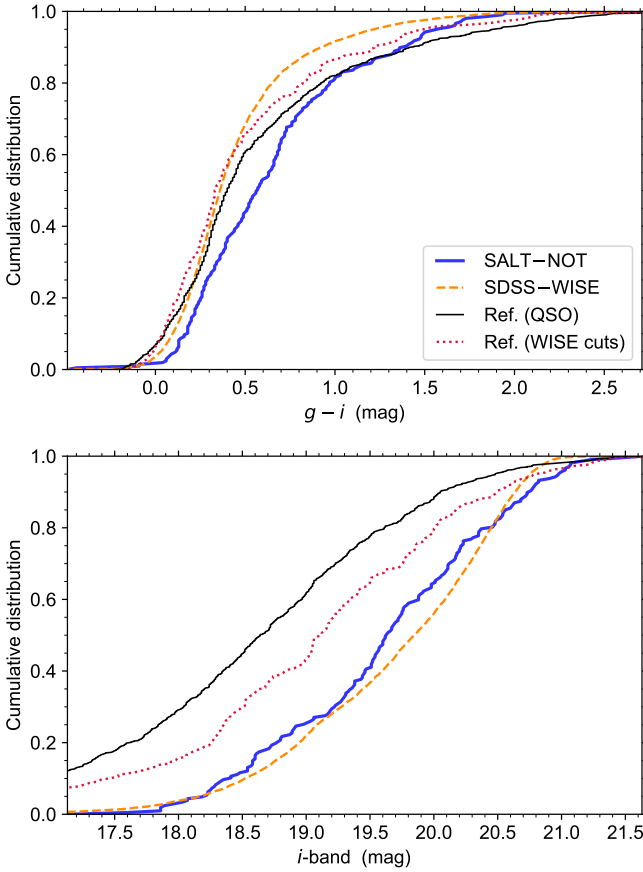


**Figure 4.** Comparison of the MALS SALT-NOT sample (blue, thick line) with the full quasar *reference* sample (black, thin line), the quasar *reference* sample that fulfills Eq. (1; red, dotted line), and the SDSS+WISE quasar comparison sample (orange, dashed line).

and only 7 of these are brighter than 200 mJy. We will ignore this distinction in our statistical analysis.

We first check the effect of requiring detections in all three WISE bands used in our criteria. We find that out of the 10,498 quasars, only 56% have WISE photometry in all three bands. Overall, the quasars *with* WISE detections are brighter and have slightly redder colors compared to the quasars without WISE detections in all three bands. The median  $i$ -band brightness is 19.9 and 20.4 mag for quasars with and without WISE detections, respectively, and the median  $g - i$  color differs by 0.034 mag (Fig. 4). When restricting the color comparison to quasars with the same brightness ( $i < 20$  mag), the color difference diminishes to 0.023 mag; i.e., at the order of the photometric uncertainty.

The average redshift of quasars with WISE detections is lower ( $< z > = 1.48$ ) than quasars without WISE detections ( $< z > = 1.86$ ), which is in line with the brighter  $i$ -band magnitudes for quasars with WISE detections. Yet, there are no significant color differences as a function of redshift.

The next step is to quantify the effect of our WISE color criteria. We use the same optical comparison sample as defined above to check the optical brightness and colors of those quasars that meet the criteria in Eq. (1) and those that do not. Our WISE criteria have been designed to reduce the number of  $z < 1.4$  quasars, and as shown in Fig. 2, our sample effectively reduces the number of low-redshift quasars. Due to the largely different redshift-distributions, it is not surprising to find that the quasars that follow Eq. (1) are 0.4 mag fainter on average. Considering only quasars at  $z > 2$ , the quasars that follow our WISE criteria Eq. (1) are on average only 0.2 mag fainter. We find no significant difference

in optical color between quasars that meet our criteria and those that do not.

Lastly, we compare the SALT–NOT sample with the *reference* sample of quasars as well as the optically-selected SDSS quasar sample. In Fig. 4, we show the cumulative distributions of  $g-i$  color and  $i$ -band brightness. We find that the SALT–NOT sample has on average redder colors than the other samples, with the optically-selected sample showing the bluest colors. The median color difference is 0.2 mag. On the other hand, the SALT–NOT sample is fainter than the *reference* quasar sample and shows a distribution of optical brightness similar to the SDSS quasar sample.

In conclusion, we find that our imposed WISE criteria result in a sample of radio-bright quasars that is fainter and slightly redder than radio-selected (*reference*) quasars. Part of this difference in color and brightness can be attributed to the difference in the respective redshift distributions. Nonetheless, our sample is representative in terms of redder optical colors commonly observed in radio-selected samples while probing fainter quasars more representative of deep, optically-selected samples.

### 3. OBSERVATIONS AND DATA ANALYSIS

We observed 255 and 99 targets with SALT and NOT, respectively. Of these, 40 targets, labelled as SUGAR (NOT-SALT) in column 7 of Table 3, are common to both the sub-surveys. In this section, we present details of SALT observations and data analysis. The corresponding details for NOT observations carried out in 2016 August (P53-012) and 2017 February (P54-005; PI: Krogager et al. (2018)).

We used the Robert Stobie Spectrograph (RSS; Burgh et al. 2003; Kobulnicky et al. 2003) on SALT to obtain optical spectra of 255 targets. These service mode observations were carried out between November 2014 and April 2017 through the programmes: 2014-2-SCI-027, 2015-1-SCI-012, 2015-2-SCI-030, 2016-1-SCI-022 and 2016-2-SCI-17 (PI: N. Gupta). Each observing block typically contained two  $\sim$ 10 minutes science exposures, in the long-slit mode having a slit width of  $2''$ . We note that the calibration lamp and the flat field images required for the wavelength calibration and flat fielding were obtained separately, as part of 2015-1-SCI-012. The detector in RSS consists of a mosaic of three CCDs with a total size of  $3171 \times 2052$  pixels. The pixel size is  $15\mu\text{m}$  which corresponds to a spatial sampling of  $0.1267''$  per pixel. We opted for  $2 \times 2$  pixel binning to improve the signal-to-noise ratio (SNR). We used RSS PG0900 grating with a grating tilt angle of  $15.875^\circ$ . This provides a wavelength coverage

of  $4486\text{--}7533\text{\AA}$ , but with gaps at  $5497\text{--}5551$  and  $6542\text{--}6589\text{\AA}$ . The resulting spectral resolution is  $R = 1064$  at  $6041\text{\AA}$ . The observations were performed on clear nights with a median seeing of  $\sim 1.5''$ . The fainter targets were assigned higher priority for observations on dark and gray nights.

The preliminary data reduction, i.e., gain correction, overscan bias subtraction, cross-talk correction and amplifier mosaicing were performed by the SALT observatory staff using the semi-automated pipeline PySALT<sup>3</sup>, the Python/PyRAF software package for SALT data reduction (Crawford et al. 2010). Using IRAF<sup>4</sup> packages, we further removed cosmic rays and applied the flat-field correction. The wavelength calibration was performed using a Xenon arc lamp and the spectrophotometric standard star L377 was used for flux calibration. We extracted 1D spectra from individual exposures after subtracting the background. We also corrected the 1D spectra for atmospheric extinction and applied the air to vacuum correction to the wavelengths. The final 1D spectra of the quasars used for analysis is the combination of all the available exposures (typically  $\sim$ 20 min on-source).

### 4. SPECTRAL ANALYSIS

We visually examined all the spectra for the presence of emission lines. In Fig. 5, we show 5 representative SALT spectra. These represent: low- $z$  ( $z < 1.0$ ; top two panels), intermediate- $z$  ( $1.0 < z < 1.9$ ; middle panel), high- $z$  ( $z > 1.9$ ; second panel from the bottom) and the emission line less (ELL; bottom panel) AGN. Flux scale for each spectrum is corrected for slit losses using the PS1 photometry. Here, we have ignored the possibility of continuum variability between our spectra and the PS1 observations.

For the spectra exhibiting two or more emission lines, the line identifications are robust, and hence the redshifts estimated are also correct within the wavelength uncertainty. However, the line identification is more challenging in the cases with very faint trace/emission lines or with only single emission line detection (see second panel from top in Fig 5 for example). For such sources the identification is based on line widths, expected relative strengths and the absence of other lines within the observed wavelength range. We also used var-

<sup>3</sup> <http://pysalt.salt.ac.za>

<sup>4</sup> IRAF is distributed by the National Optical Astronomy Observatories, which are operated by the Association of Universities for Research in Astronomy, Inc., under cooperative agreement with the NSF.

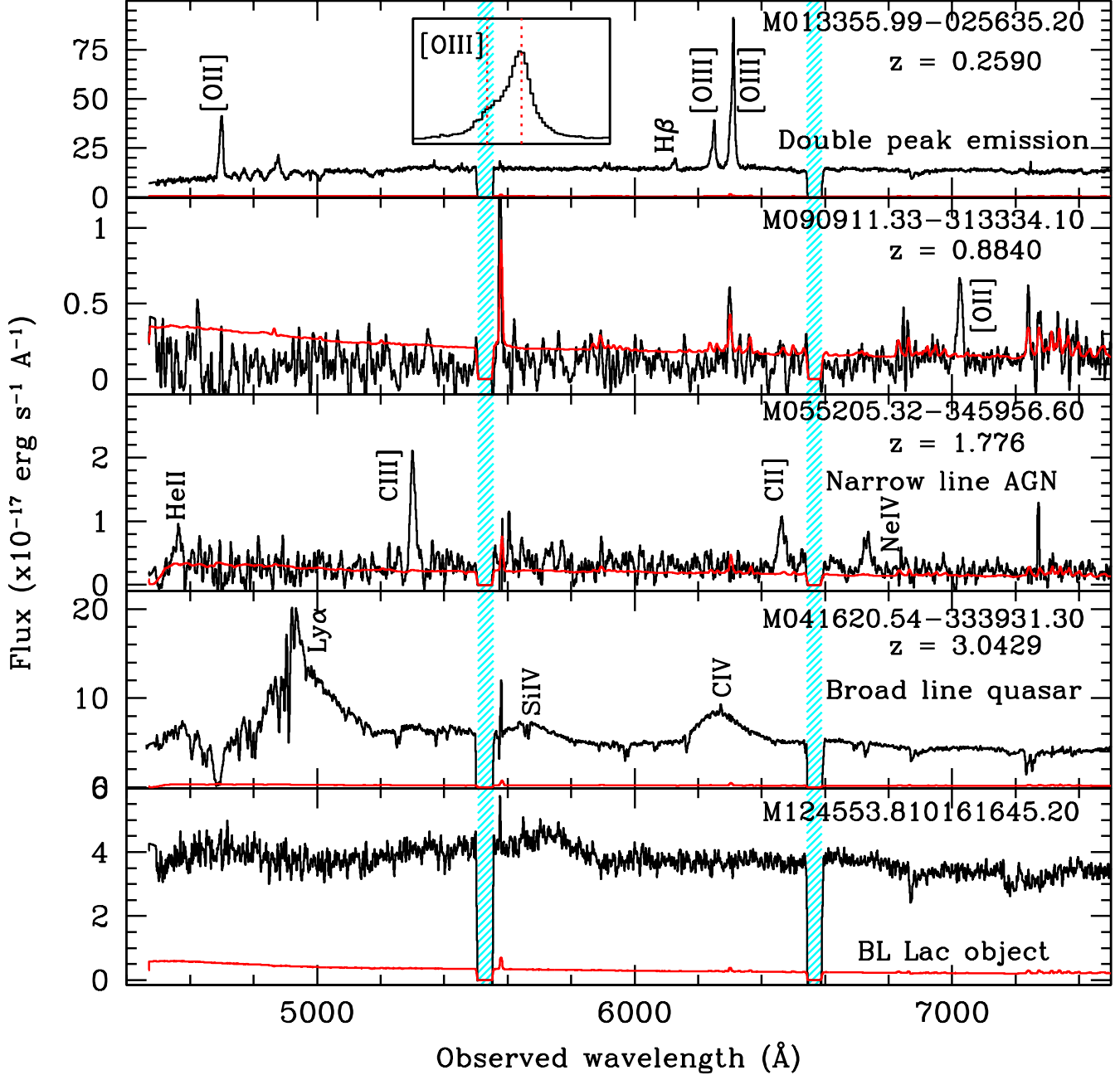


**Figure 5.** Spectra of five representative AGN from our sample at increasing redshifts from top to bottom. Different emission lines based on which the redshift was determined are identified. All the spectra are smoothed by 3 to 7 pixels for visual clarity. The error spectra are shown in red in each panel. The hashed regions mark the spectral range falling in the CCD gaps. Inset in the top most panel shows the double peak  $[\text{O III}]\lambda 5007$  profile. In the bottom panel an example of AGN without detectable emission lines is shown. We use photometric variability to identify such objects as BL Lacs (see Section 5.7).

ious AGN (QSO, Seyfert1 and Seyfert2) templates from the literature<sup>5</sup> to aid the process of line identification.

After line identification, we used peaks of prominent lines, i.e., Ly $\alpha$  for  $z > 2.66$ , C IV for  $1.87 < z < 3.86$ ,

Mg II for  $0.58 < z < 1.69$ , C III for  $1.328 < z < 2.938$ ,  $[\text{O II}]$  for  $0.19 < z < 1.01$  and,  $[\text{O III}]$  and H $\beta$  for  $z < 0.50$ , to measure the redshifts. The rest wavelengths are taken from the SDSS emission line list<sup>6</sup>. In the cases where the peak of the prominent emission line is affected

<sup>5</sup> <https://archive.stsci.edu/hlsp/references/atlas/cdbs/grid/agn>

<sup>6</sup> <http://classic.sdss.org/dr6/algorithms/linstable.html>

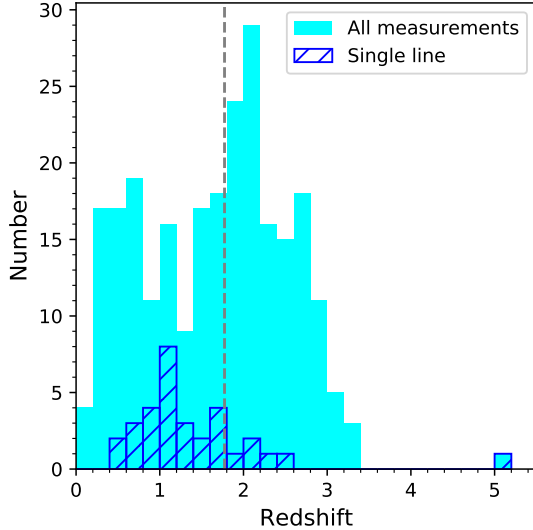


**Figure 6.** Redshift distribution for all the SALT-NOT targets with spectroscopic redshifts. The vertical dashed lines mark the median value. The distribution of redshifts based on single emission line (blue-hashed histogram) is also shown. The redshifts based on a single emission line should be treated with caution. The correct redshift of AGN marked at  $z \sim 5$  is  $z = 0.977$  (see Section 5.6 for details).

by absorption or it falls in the CCD gap, we fit the emission line avoiding these regions and take the centroid of the fit to estimate the redshift. The overall uncertainty in redshift ( $\Delta z$ ) that is introduced due to wavelength calibration issues and uncertainty in measuring the peak is roughly  $\Delta z \approx 0.005$ .

The redshift distribution of all the AGN (250) with emission line identifications is shown in Fig. 6. In 32 cases the redshift is based on a single emission line assumed to be C IV, C III, Mg II, [O II] or Ly $\alpha$ . In Table 3, these are marked with \*a, \*b, \*c, \*d and \*f, respectively. In 26 cases, no emission lines (i.e., ELLs) are detected in the spectra. In 27 cases, no continuum or emission lines are detected (i.e., DFs).

## 5. RESULTS

The properties of the SALT-NOT sample consisting of 250 quasars with emission lines, 26 ELLs and 27 DFs are provided in Table 3. In this section, we present selected results based on continuum and emission lines detected in our optical spectra. It is well beyond the scope of this paper to discuss all the aspects in detail. Hence, we present overall properties of the observed sample and comparison with the *reference* sample in Sect. 5.1. This is followed by short overviews of AGN detected at  $z < 3.5$  split across Sections 5.2 to 5.5 on the basis of different groups of observable emission lines. For AGN at  $z < 1.9$ , we discuss only the fraction of narrow emission

line objects (type II quasars or radio galaxies) found in different redshift intervals and the morphology of associated radio emission. For quasars at  $1.9 < z < 3.5$ , we also present the distribution of BH masses and the fraction of broad absorption line (BAL) quasars. The farthest narrow line AGN in our sample is M1513–2524 ( $z_{em} = 3.132$ ), and the one with largest projected linear size of radio emission (size $\sim$ 330 kpc) is M0909–3133 ( $z_{em} = 0.884$ ). For some individual objects the details, such as the morphology of associated radio emission, host galaxy and emission line properties, relevant to the discussion presented in these sections are provided in Appendix B. The properties of M1312-2026, the potential highest redshift AGN in the sample, are discussed in Sect. 5.6. In Sections 5.7 and 5.8, we discuss AGN with no optical emission lines and dark fields, respectively.

### 5.1. Overall properties

The basic properties, i.e., redshift, W1 and *i*-band magnitudes of the SALT-NOT sample are summarized in Fig. 7. We have also used emission lines detected in our spectra to classify objects as narrow-line (NL) or broad-line (BL) AGN. In Table 3, these are labeled as ‘G’ and ‘Q’, respectively. In total, 51/250 objects are NLAGN and 33 of these are at  $z < 0.5$ . As expected the fraction of NLAGN in our sample falls off at higher redshifts.

Fig. 7 also provides a comparison with the *reference* sample of quasars satisfying our MIR cut (see Section 2.1). The median redshift of the SALT-NOT sample is only slightly lower but a deficit of lower redshift AGN in the *reference* sample is apparent. A two-sample Kolmogorov-Smirnov (KS) test shows that there is a less than 1 percent chance (p-value = 0.008) that the two samples are different purely by chance. Related to this, we also note that in the SALT-NOT sample,  $20 \pm 3\%$  objects are NLAGN whereas based on the *reference* sample only  $6^{+2.1}_{-1.6}\%$  are expected.

In Fig. 7, we also compare W1 and *i*-band magnitudes of the two samples. Clearly, the SALT-NOT sample corresponds to a population of fainter AGN. We note that the probabilities of two samples being drawn from the sample populations are  $1.7 \times 10^{-4}$  for W1 brightness and  $1.6 \times 10^{-8}$  for *i*-band brightness. This further confirms the assertion made in Sect. 2.3 that the inclusion of W3, the less sensitive WISE band, in our target selection has not biased our sample towards brighter objects. In particular, the *i*-band magnitudes of AGN in our sample at  $z < 0.5$  and  $z > 0.5$  are similar. Therefore, the excess of NLAGN at  $z < 0.5$  in our sample is intriguing. It is likely a direct consequence of the selection of optically fainter targets through MIR color selection. Excluding

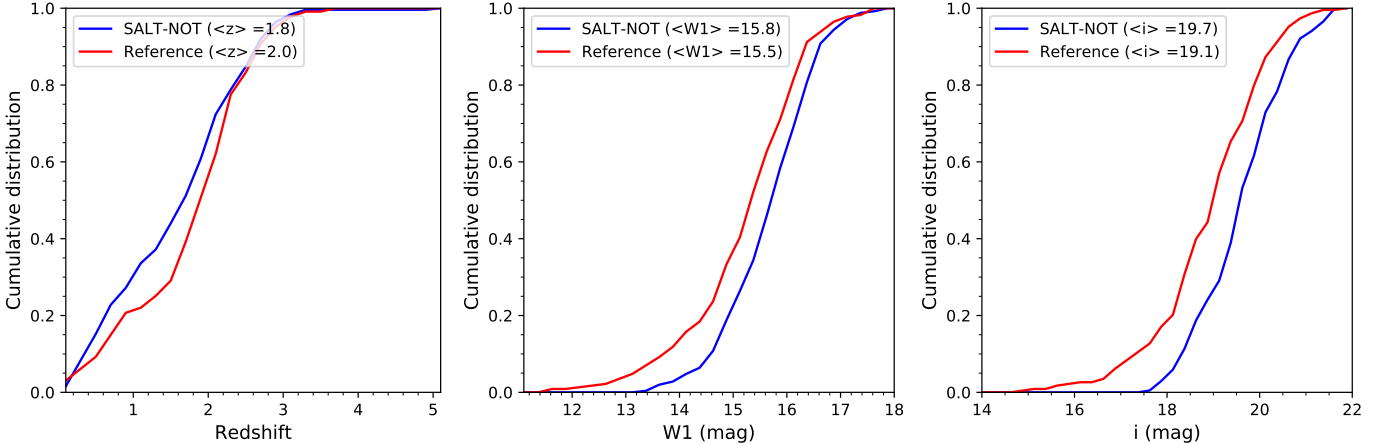


**Figure 7.** Comparison of our SALT–NOT sample and the subset of the *reference* sample satisfying our WISE criteria. The median values are also provided.

these  $z < 0.5$  NLAGN renders the  $z$ -distributions of the SALT–NOT sample and the *reference* sample statistically identical.

### 5.2. AGN at $z < 0.5$

For  $z < 0.5$  AGN, our SALT spectra cover [O II], [O III] and H $\beta$  emission lines. The NOT spectra additionally cover the Mg II emission line as well. Overall, the SALT–NOT sample has 33/303, i.e., 11% AGN in our sample are at  $z < 0.5$ . We find the spectra in all the 33 cases to be mostly dominated by narrow permitted emission lines (with  $\text{FWHM} < 2000 \text{ km s}^{-1}$ ). The available optical images are also consistent with their hosts being galaxies with weak or no nuclear emission. Compared to this, in the *reference* sample (SDSS), only  $\sim 32\%$  (6/19) of the  $z < 0.5$  AGN satisfying our MIR wedge are classified as galaxies. As mentioned above, this difference with respect to the *reference* sample is most likely due to the optical faintness of the SALT–NOT sample and the specific goal to reject low-redshift AGN (Barrows et al. 2021).

The radio emission associated with these NLAGN is often extended, the largest projected linear size being  $\sim 250$  kpc (details in Appendix B). An examination of optical emission lines led to identification of 2 dual AGN showing double peaked spectra (an example is shown in top panel of Fig. 5; more details in Appendix B). Our detection rate of  $6^{+8\%}_{-4\%}$  is marginally higher, but only at  $1\sigma$ , than the detection rate (1%) of dual AGN in SDSS (Liu et al. 2010).

### 5.3. AGN at $0.5 < z < 1.0$

For AGN at  $0.5 \leq z \leq 1.0$  (35/303), the SALT–NOT spectra cover both Mg II and [O II] emission lines. About  $32^{+13\%}_{-10\%}$  (12/35) of these show emission lines of [O II], Ne IV and Ne V without (or narrow) Mg II broad emis-

sion lines. The fraction of NLAGN (8/28 i.e.,  $29^{+14\%}_{-9\%}$ ) is consistent with the reference sample.

In VLASS 3 GHz images, 8/12 ( $75^{+25\%}_{-23\%}$ ) of the NLAGN in the SALT–NOT sample exhibit extended radio emission with lobes, the largest projected linear size being 330 kpc. Among BLAGN, as expected, a much smaller fraction ( $\sim 40\%$ ) is associated with extended radio emission (Padovani et al. 2017; Hickox & Alexander 2018). The largest extent is only 180 kpc (see Appendix B for details). We also examined the radio morphology and optical emission line profiles for evidences of interaction between radio jet and the host galaxy emission (see e.g., Mullaney et al. 2013). In three cases, the radio morphology is distorted. But only in one of these (details in Appendix B), the [O II] line is asymmetric, which may be an indication of radio jet-ISM interaction (e.g., Gupta et al. 2005).

### 5.4. AGN at $1.0 < z < 1.9$

At  $1.0 \leq z \leq 1.9$ , our sample has 71 AGN. Only two of these are possibly NLAGN and the radio emission in both the cases has a double lobed morphology (details in Appendix B). This low fraction (3%; 2/71) of NLAGN is consistent with the *reference* sample, which has 0/53 such AGN in this redshift range.

### 5.5. AGN at $1.9 < z < 3.5$

As previously mentioned, for these redshifts the SALT–NOT spectra of 110 AGN in our sample allow detection of C IV emission lines. Based on the width of C IV emission line (i.e  $\text{FWHM} < 2000 \text{ km s}^{-1}$ ) we identify 4 of these objects to be the NLAGN. In comparison, the *reference* sample has no NLAGN (0/128) at  $z > 1.9$ , which is consistent at  $2\sigma$  considering one-sided Poissonian statistics. The details of NLAGN at  $1.9 < z < 3.5$  in our sample are provided in Appendix B). The emis-

sion line ratios are typical of what is observed in high- $z$  radio galaxies. Two of these i.e., M1315–2745 and M1513–2524 are among the largest radio galaxies at these redshifts (see figure 13 of Shukla et al. 2021a, for the latest compilation). In the rest of this section, we discuss BH masses, Eddington ratios and BALs associated with the BLAGN.

### 5.5.1. BH masses and Eddington ratios

Under the assumption that broad line region (BLR) clouds are in virial equilibrium, the mass of the black hole,  $M_{\text{BH}}$ , is given by

$$M_{\text{BH}} = f \frac{R_{\text{BLR}} \text{ FWHM}^2}{G} \quad (2)$$

where  $G$  is the gravitational constant and  $f$  is the virial coefficient that depends on the geometry and kinematics of the BLR. The radius of the BLR,  $R_{\text{BLR}}$ , is generally estimated using empirical relations between continuum or line luminosity (e.g., Kaspi et al. 2000). The value of  $f$  is also empirically determined (e.g., Onken et al. 2004). Following Shen et al. (2011), we estimate virial BH masses for quasars with the C IV emission line using a relation of the form

$$\log \left( \frac{M_{\text{BH}}}{M_{\odot}} \right) = a + b \log(\lambda L_{\lambda}) + 2 \log(\text{FWHM}) \quad (3)$$

where  $a$  and  $b$  are calibrated from reverberation mapping for a particular emission line (e.g., Denney et al. 2010). The broad line FWHM is in  $\text{km s}^{-1}$  and the continuum luminosity,  $\lambda L_{\lambda}$ , which is a proxy for  $R_{\text{BLR}}$ , is in units of  $10^{44} \text{ erg s}^{-1}$ . We adopt  $a = 0.660$  and  $b = 0.53$  for equation 3 based on the empirical relationship provided by Vestergaard & Peterson (2006) to estimate BH mass for our sample.

Further, to place our SALT-NOT sample in the broader context of the overall quasar population, we compare our measurements to the compilation of 105,783 SDSS DR7 quasars provided by Shen et al. (2011). For direct comparability of the measurements, we largely follow the method of Shen et al. (2011) to measure C IV FWHM and  $\lambda L_{\lambda}$  at 1350 Å. In short, we fit a power law to the continuum in the rest wavelength ranges of 1445 – 1465 and 1700 – 1705 Å. Prior to continuum fitting we mask any unwanted spikes stronger than  $5\sigma$ . Then, we fit the continuum subtracted emission line in the wavelength range 1500 – 1600 Å using three Gaussians. The FWHM of the emission line, referred to as the *full* line FWHM, is then estimated from the fit after rejecting any individual components with strength  $< 5\%$ . The continuum luminosity at 1350 Å ( $L_{1350}$ ) is estimated using the same power law used to fit the continuum underlying the C IV emission line. We are able

to reliably estimate *full* C IV line FWHM, continuum luminosity at 1350 Å and BH mass of 86/110 quasars ( $z > 1.9$ ) from our sample. We have excluded 24 AGN with low SNR profiles or lines affected by the CCD edge. Similar to Shen et al. (2011), the bolometric luminosity ( $L_{\text{Bol}}$ ) have been estimated by applying the bolometric correction factor of 3.81 to  $L_{1350}$  (Richards et al. 2006). The Eddington ratio ( $\lambda_{\text{Edd}}$ ) is estimated as  $L_{\text{Bol}}/L_{\text{Edd}}$ , where  $L_{\text{Edd}}$  is the Eddington luminosity.

The compilation of Shen et al. (2011) consists of 11,840 non-BAL quasars at  $1.9 < z < 3.5$  (median  $z = 2.29$ ), the redshift range covered by our sample (median  $z = 2.34$ ). We have restricted the sample of Shen et al. (2011) to the subset that has been identified by a uniform target selection algorithm and flux limited to  $i = 19.1$  at  $z < 2.9$  or  $i = 20.2$  at  $z > 2.9$  (Richards et al. 2002). A distinguishing feature of the SALT-NOT sample is the high radio brightness of quasars. In particular, the  $z > 1.9$  quasars in SALT-NOT sample have predominantly flat radio spectra. The median spectral index<sup>7</sup>,  $\alpha_{0.4}^{1.4}$ , derived using the NVSS 1420 MHz and the uGMRT 420 MHz total flux densities is  $\sim -0.38$  (Gupta et al. 2021b). In the uGMRT images, 79/88 of these are represented by a single Gaussian component. Therefore, we further restrict the sample of Shen et al. (2011) to 786 core-dominated quasars, hereafter *Shen11-core* in short, detected in FIRST.

In left panel of Fig. 8, we show the distributions of *full* C IV FWHM and 1350 Å luminosity for SALT-NOT and *Shen11-core* quasars. The SALT-NOT sample extends about 0.5 dex fainter in 1350 Å luminosity. The two-sample KS test probability of these two samples being drawn from the same parent sample is extremely small (p-value =  $4 \times 10^{-13}$ ). The C IV FWHM of the SALT-NOT sample (median FWHM =  $4445 \text{ km s}^{-1}$ ) is marginally smaller than the *Shen11-core* sample (median FWHM =  $4660 \text{ km s}^{-1}$ ), and this difference is statistically insignificant. We note that if the C IV profiles are affected by non-virial motions such as outflows (Coatman et al. 2016), the influence ought to be similar in both the samples. Due to the luminosity dependence of  $\lambda L_{\lambda}^{0.66}$  in the virial mass estimator, the overall BH masses estimated using equation 3 are lower for the SALT-NOT sample (see right panel of Fig. 8). The KS test probability of two  $M_{\text{BH}}$  distributions being drawn from the same parent sample is extremely small (p-value =  $3 \times 10^{-5}$ ; see left panel of Fig. 9).

In the middle panel of Fig. 9, we show the radio-loudness parameter ( $R = f_{5\text{GHz}}/f_{2500}$ ), defined as the

<sup>7</sup> Spectral index  $\alpha$  is defined by the power law,  $S_{\nu} \propto \nu^{\alpha}$

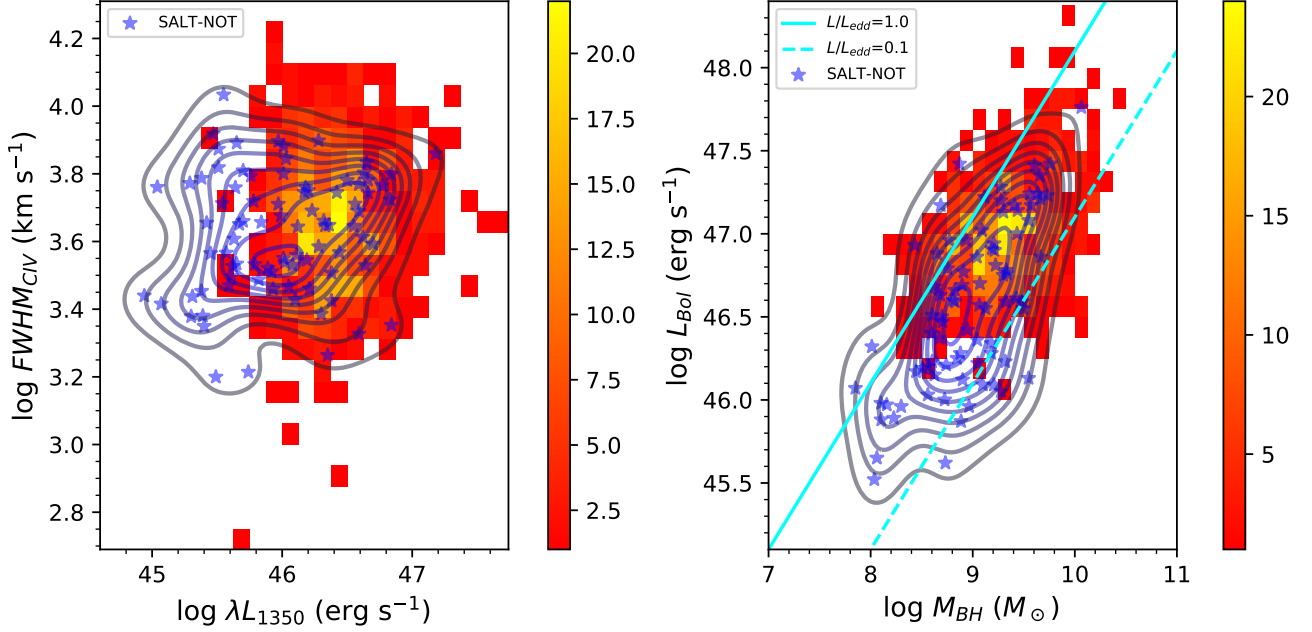


**Figure 8.** Comparison of luminosity  $\lambda L_{1350}$  vs. full CIV FWHM (left), and  $L_{Bol}$  vs.  $M_{BH}$  (right). In both the panels, the core-dominated quasars from from (Shen et al. 2011) are shown as 2D histogram, and SALT-NOT quasars are  $\star$  and contours.

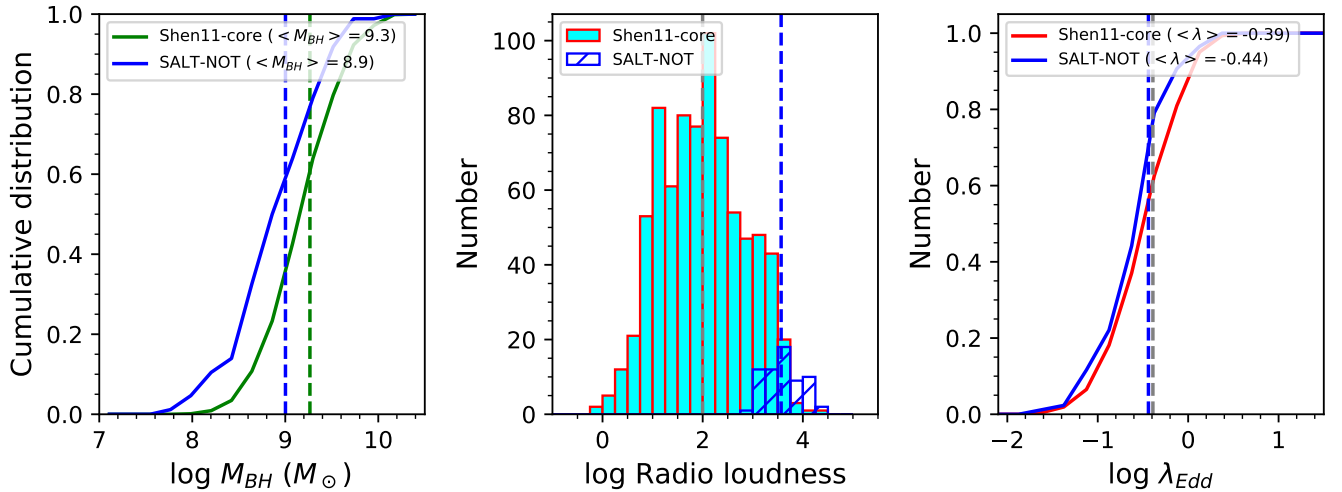


**Figure 9.** Comparison of BH mass (left), Radio loudness (middle) and Eddington ratios (right) for quasars from (Shen et al. 2011) and SALT-NOT sample. The vertical lines represent median values.

ratio of the rest-frame flux densities at 5 GHz ( $f_{5GHz}$ ) and at 2500 Å ( $f_{2500}$ ), for the two samples. For SALT-NOT quasars, the values of  $f_{5GHz}$  have been estimated using the flux density at 1.4 GHz from NVSS using the spectral slopes  $\alpha_{0.4}^{1.4}$  from Gupta et al. (2021b). In cases where  $\alpha_{0.4}^{1.4}$  is unavailable, we have used the median  $\alpha_{0.4}^{1.4}$  of  $-0.38$  instead. The values of  $f_{2500}$  have been estimated by interpolating the PS1 photometry. Clearly, the SALT-NOT sample represents extremely radio-loud quasars (median  $R = 3685$ ). The corresponding Eddington ratio is only slight smaller (median  $\log \lambda_{Edd} = -0.44$

vs.  $-0.39$ ) as compared to the *Shen11-core* sample and the difference is statistically insignificant ( $p$ -value = 0.02). Thus, over four orders of magnitude covered by the radio-loudness in the SALT-NOT and *Shen11-core* quasars, we see no dependence of radio-loudness on the accretion rate. This confirms the saturation of radio-loudness observed at low Eddington ratios (see Fig. 3 of Sikora et al. 2007).

### 5.5.2. BAL occurrence

We focus now on the 105 SALT-NOT AGN showing CIV emission at  $z_e \geq 1.9$  to search for broad absorption

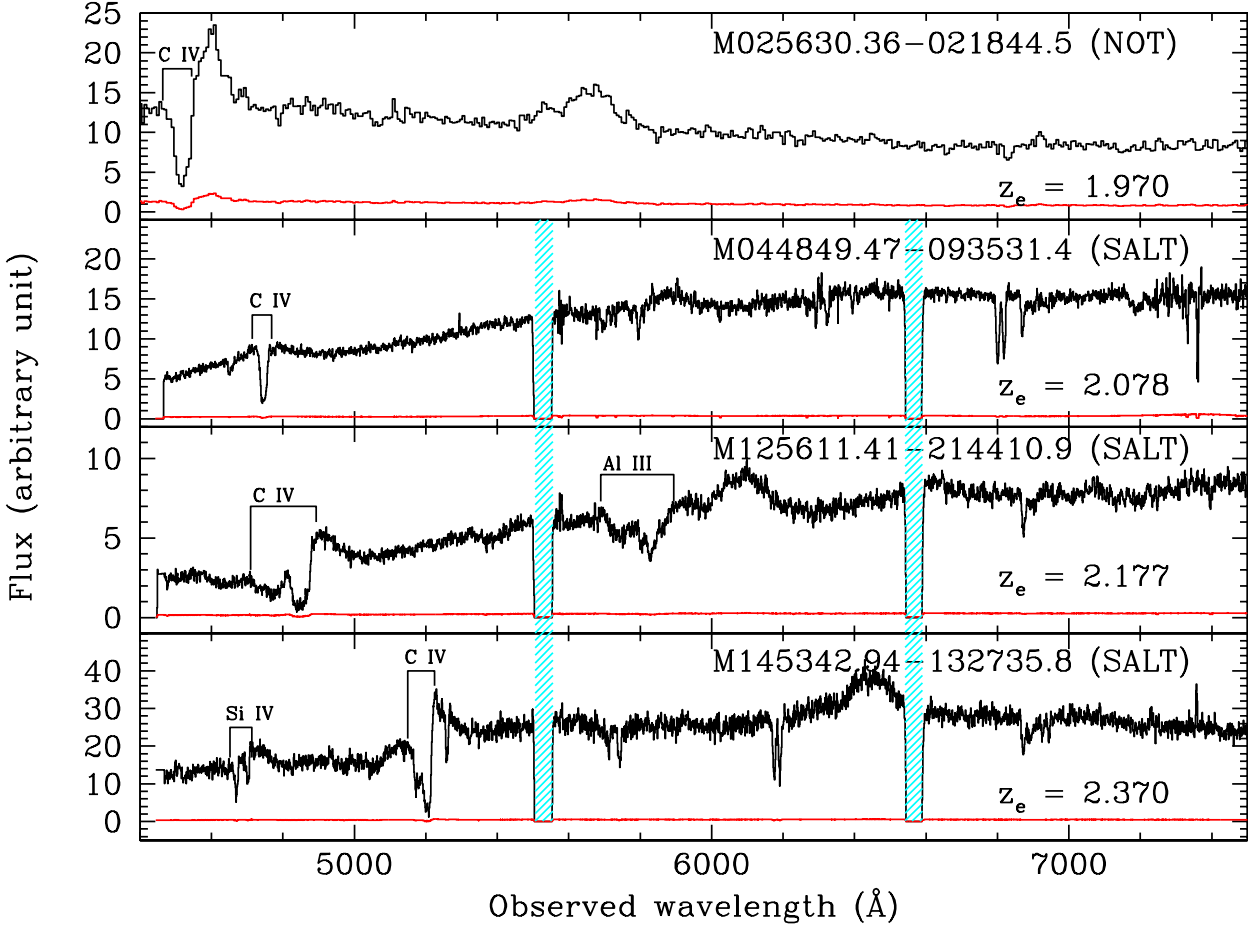


**Figure 10.** Spectra of four BAL QSOs found in our sample and associated error spectra (in red) are shown. Different BAL absorption are marked in each panel. Hashed regions are the CCD gaps in our SALT observations.

lines (BALs) representing outflowing gas. We exclude 7 cases at  $z \sim 2.6$  where the blue wing of CIV emission line falls in the CCD gap. In the remaining, we detect 4 CIV BAL quasars (see Fig. 10), i.e., an overall BAL detection rate of  $4/98 = 4_{-2}^{+3}\%$ . We find a consistent BAL fraction in our *reference* sample, without any MIR cut, where 9 out of 175 quasars at  $z \geq 2.0$  show CIV BALs ( $5\pm2\%$ ).

Typically, 10-20% of radio sources are detected as BALQSOs. Becker et al. (2000) studied the properties of radio selected BAL quasars from First Bright Quasar Survey sample. They also noticed that while the BAL detection rate is high among radio loud quasars their dependence on the radio luminosity is complex. In particular, the authors find a deficiency of BALQSOs among very radio bright quasars. Specifically, the BAL fraction drops from  $20.5_{-5.9}^{+7.3}\%$  at  $L_{1.4\text{GHz}} \sim 10^{25} \text{ W Hz}^{-1}$  to  $< 8\%$  at  $L_{1.4\text{GHz}} \sim 3 \times 10^{26} \text{ W Hz}^{-1}$  (Shankar et al. 2008). The low BAL detection rate in the SALT-NOT sample which has  $L_{1.4\text{GHz}} > \sim 10^{27} \text{ W Hz}^{-1}$  is consistent with this trend in luminosity.

The radio emission associated with M1453–1327 is extended (largest angular size, LAS $\sim 17.1''$ ) with a projected linear size of 140 kpc. In the other three cases, the radio emission is dominated by a compact component (projected linear size  $< 5$  kpc). This is consistent with the previous results that the radio emission associated with BALQSOs is compact (Becker et al. 2000). Notably, the 4 BALQSOs have  $R_{5\text{GHz}/2500\text{\AA}}$ ,  $\lambda_{\text{Edd}}$  and  $M_{\text{BH}}$  in the range of  $10^{2.9-3.2}$ ,  $10^{0.2-0.5}$  and  $10^{9.1-9.8} \text{ M}_{\odot}$ , respectively, which correspond to objects with least radio loudness, and highest BH mass and Eddington ratios.

### 5.6. M1312–2026: a powerful AGN at $z \sim 5$ ?

The bright radio sources at high- $z$  are extremely rare. This is partly due to the interaction between the emitting electrons and the cosmic microwave background (CMB) which makes AGN less luminous in radio (Ghisellini et al. 2014). In the SALT spectrum of M1312–2026 (Fig. 11), we identify only a single narrow emission line over the wavelength range covered. If this emission line is Ly $\alpha$ , then the corresponding redshift will be

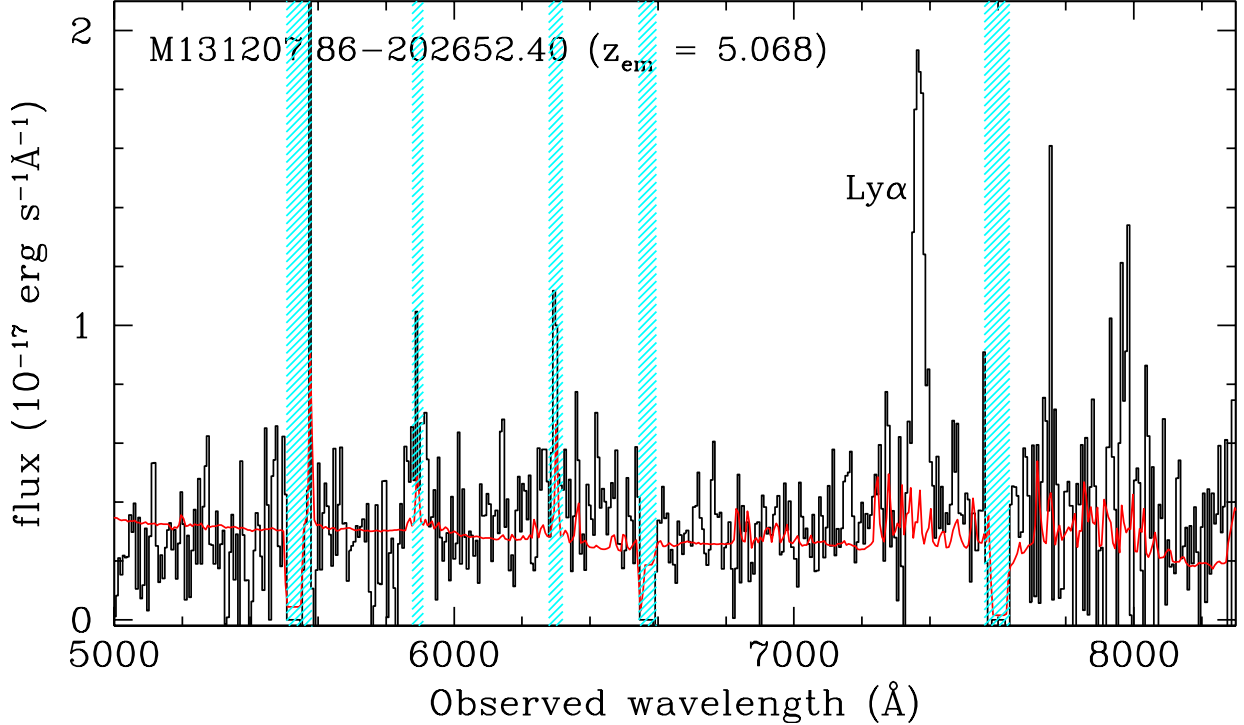


**Figure 11.** The SALT spectrum of M1312-2026. The overall SALT spectrum and the single emission line assumed to be Ly $\alpha$  at  $z = 5.068$  have been consistently reproduced in four individual exposures, two of which were taken using a different spectral set-up. The error spectrum is shown in red. The shaded regions (cyan) mark the spectral gap and spectral range affected by sky subtraction residuals. The VLT X-shooter spectrum shows that the actual  $z_{\text{em}} = 0.977$  (see text for details).

**Table 1.** Flux densities of M1312-2026.

Frequency (GHz)	Flux (mJy)	Deconvolved Size	Ref.
0.23	2577	$7.1'' \times 3.3'', 0.0^\circ$	(1)
1.39	677	$0.8'' \times 0.2'', 5.0^\circ$	(2)
1.40	778	$< 17.9''$	(3)
4.86	233	$< 2''$	(4)

**References:** (1) Gupta et al. (2021b); (2) This work. Observed on 2018 July 14 for 10 mins (on-source time) using uGMRT with 200 MHz wideband covering 1260-1460 MHz.; (3) NVSS; (4) Kapahi et al. (1998).

$z = 5.068$ . At 4.86 GHz, the radio source has a flux density of 233 mJy and a size of  $< 2''$  (Table 1), and is unambiguously identified with a WISE and PS1 object with colors that are consistent with it being a high- $z$  radio loud quasar.

In order to confirm the redshift of M1312-2026, we re-observed the object with X-shooter of the Very Large Telescope on 2022 February 01. In the X-shooter spectrum, we do not detect expected Mg II, C III] and C IV lines corresponding to the presumed Ly $\alpha$  at  $z=5.068$ . Instead, the detection of [O III], H $\alpha$  and H $\beta$  emission lines confirm the above identified line to be [O II] and

the systemic redshift of the quasar to be  $z = 0.977$ . Further details of the X-shooter spectrum of this highly reddened object will be presented in a future paper.

### 5.7. Objects without emission lines

In recent times, the locus of MIR colors of known *Fermi* detected AGN have been used to build large samples of blazars (e.g., Chang et al. 2017; D’Abrusco et al. 2019). These MIR color-selection techniques use the first three or all four bands of WISE, and typically extract  $\sim 0.5\%$  ( $< 0.001\%$ ) of the overall radio<sup>8</sup> (WISE) source population as blazars. They include both classes of blazars: (i) BL Lacs with featureless optical spectra, i.e., no emission lines (equivalent width  $< 5 \text{ \AA}$ ; Stickel et al. 1991), and (ii) flat spectrum, radio-loud quasars (FSRQs) with quasar-like emission lines. In the recent literature, these two classes are also referred to as BZBs, i.e., blazars of BL Lac type and BZQs, i.e., blazars of quasar type, respectively (Massaro et al. 2009).

In the following, we focus on the 26 objects without emission lines (emission line less; ELL) in our sample that can be considered candidate BZBs. The median

<sup>8</sup> Based on the NVSS sensitivity.

$q_{12}$  parameter which is defined as the logarithm of the ratio of flux densities measured in  $W3$ -band and at 20cm of ELL targets is  $-2.8$ . This is well outside the range of  $(-1.85, -1)$  for BZB candidates based on the locus of *Fermi* detected BL Lacs (D'Abrusco et al. 2019, see also Fig. 2). The SALT-NOT ELLs thus represent a population of candidate BL Lacs that is under-represented in the MIR selected population.

The most crucial and somewhat controversial aspect of establishing the BL Lac nature of AGN is to confirm its featureless optical spectra. Our SALT/NOT spectra are adequate to detect the broad emission lines from AGN but weak lines may be missed due to the poor spectral resolution and noisy data. This is illustrated by the case of two ELL candidates, M0051+1747 and M0105+1845, for which no redshift determination could be established based on the NOT spectra alone. However, these targets have later been observed as part of SDSS and have been identified as  $z_{\text{em}} = 1.536$  and  $1.074$ , respectively. We note that these redshifts are consistent with weak and narrow emission lines in the NOT spectra, which were originally marked tentative. Thus, the objective of the analysis presented here is to identify BL Lac candidates based on the general properties of blazars: large time variability at all wavelengths and timescales, polarized emission, and a flat or inverted radio spectrum (e.g., Rector & Stocke 2001a).

We evaluate the variability of ELLs using the data from the Zwicky Transient Facility (ZTF; Masci et al. 2019). The  $r$ -band light curves are available for 15 AGN (median PS1  $r = 19.9$  mag; see Fig. A.1 in the Appendix A). The remaining targets are either not covered (only 3) in ZTF or are fainter (median PS1  $r = 20.9$  mag) and have time series with less than 10 data points. From the light curves, we estimate the variability amplitude ( $\sigma_{\text{rms}}^2$ ) and error ( $S_D^2$ ) on it using the normalized excess variance method described in Nandra et al. (1997) and Vaughan et al. (2003). The variability amplitude strength, VAS =  $\sigma_{\text{rms}}^2/S_D^2$ , is provided in Fig. A.1.

We also estimate the observed  $\chi_{\text{obs}}^2$  using  $\chi_{\text{obs}}^2 = \sum_{i=1}^N (m_i - \bar{m})^2/\sigma_i^2$ , where  $m_i$  are  $N$  measured fluxes with individual error  $\sigma_i$  and mean  $\bar{m}$ . The hypothesis of the AGN being intrinsically non-variable can be rejected at 99% confidence level for 11/15 targets. The remaining 4 targets are among the faintest (PS1  $r$ -band:  $20.3 - 21.7$  mag) and the conclusion is likely influenced by the low SNR of the light curve. Rejecting these and considering objects with  $\text{VAS} > 3.0$ , we obtain a sample of 4 promising (M0022+0608, M0029–1740, M1245–1616 and M2142–2444) and two marginal (M0010–2157 and M0824–1029) BL Lac candidates (see Fig. A.1). Op-

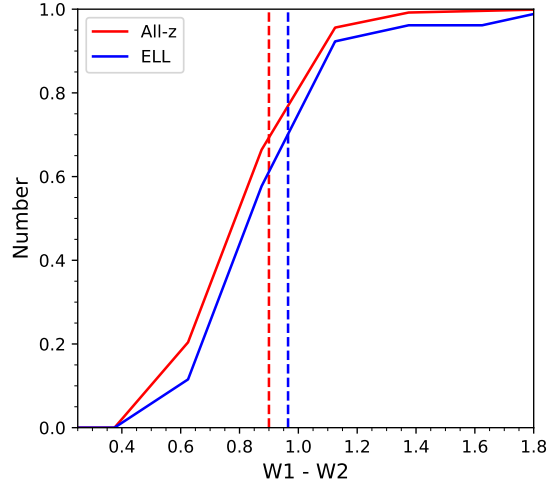


**Figure 12.**  $W1 - W2$  color distribution for SALT-NOT targets with and without redshift determinations. The median values are marked using dashed and dotted lines, respectively.

tical spectrum of M1245–1616 obtained with SALT is shown in Fig. 5.

Interestingly, the candidate with the highest VAS (M0022+0608; see Fig. A.1) is in fact a bona fide  $\gamma$ -ray emitting BL Lac (Massaro et al. 2009). Further, the candidates M0010–2157, M0029–1740, M1245–1616 and M2142–2444 are also identified in the blazar catalog of D'Abrusco et al. (2019) but as BZQ candidates on the basis of their position in the three dimensional ( $W1-W2-W3-W4$ ) WISE color-space based on the locus of confirmed *Fermi* blazars (Massaro et al. 2009; Acero et al. 2015). Further, 4/6 candidates are also polarized at 2–4% level in NVSS (Taylor et al. 2009), and except one (M0029–1740) all are core-dominated in VLASS 3 GHz images. Note that it is not unusual for BL Lacs to exhibit extended radio emission (Rector & Stocke 2001b).

If the BL Lacs are similarly represented in the 11 remaining ELLs not analysed due to the lack of ZTF light curves, then we expect another 4 candidates. In this context, it is also useful to cross-correlate all 26 ELLs with the latest *Fermi* data release (4FGL DR2; Ballet et al. 2020). We recover previously noted M0022+0608, and find two new matches corresponding to M0010–2157 and M0553–0840.

In summary, we have 7 high-probability BL Lac candidates; 6 identified on the basis of variability analysis and 1 through cross-matching with  $\gamma$ -ray sources, i.e., a detection rate of 7/303 ( $2 \pm 1\%$ ). Stickel et al. (1991) used 1 Jy sample to estimate the surface density (0.005 for  $>1$  Jy at 5 GHz) of radio selected BL Lacs. The fraction of BL Lacs in the 1 Jy sample of radio sources brighter than 20 mag ( $r$ -band) is 15%. Therefore, we expect that

better quality data through a targeted optical follow-up will confirm more of these ELLs as BL Lacs.

### 5.8. Dark fields

The 27 targets for which there are no firm optical identifications, i.e., dark fields (DFs), are also presented in Table 3. For 14 of these, the stacked PS1 catalog implies optical counterparts with a median  $i$ -band magnitude of 22.5 mag (Waters et al. 2020). Clearly, these represent the faintest targets in our sample (see last panel of Fig. 3). On average they are also fainter in WISE (see last panel of Fig. 3). But the  $W1$  magnitudes are still well within the range over which we have successfully obtained optical spectra (middle panel of Fig. 3). Thus, misidentifications due to errors in radio–MIR cross-matching is unlikely to significantly contribute to DFs. This is also confirmed by the VLASS–PS1 overlays of 24 DFs covered in PS1 (see Fig. A.2). In 20/24 cases, the radio source is compact and coincides ( $< 1''$ ) with the MIR position marked by the cross. In the remaining 4 cases, the radio emission is extended, exhibits a double-lobe morphology and the MIR source is located between them, i.e., at the expected location of the AGN.

The above implies that DFs are truly fainter than the implicit magnitude limit of SALT–NOT observations and barely detectable in PS1<sup>9</sup>. Thus, it is reasonable to assume that these have the same redshift distribution (median  $z = 1.8$ ) as the other SALT–NOT targets. The basic statistics of MIR-wedge implies that 5% of these are low-redshift radio galaxies. Indeed, upon careful inspection of the PS1 images, we identify diffuse, low-surface brightness emission associated with two targets: M0959–0236 and M1144–1455. These two targets could plausibly be radio galaxies at  $z < 1$ .

The optical faintness of the remaining DFs, presumably quasars, could be due to (i) an intrinsically low luminosity; (ii) very large amounts of dust in the foreground (intrinsic or intervening) or (iii) a very high redshift ( $z > 5$ ) such that the detectable continuum and emission lines are redshifted into the near-infrared; or (iv) a non-quasar origin of the radio/MIR emission. There is already a tentative indication of a slight excess of intervening and associated DLAs towards optically faint quasars (Ellison et al. 2008; Gupta et al. 2021b). Thus, the identified DFs in our survey may be hiding a small but important population of dusty H I absorbers. The MALS observations of these central DF targets and the other optically faint AGN in the MeerKAT field-of-view will reveal any such absorbers at  $z < 2$ .

<sup>9</sup> Note that the  $5\sigma$  depth of PS1  $i$ -band stack images is 23.1 mag.

**Table 2.** Summary of SALT-NOT and MALS (central AGN) sample.

	SALT-NOT	MALS <sup>a</sup>
Number of AGN	303	650 <sup>b</sup>
Median flux density (mJy)	300	340 <sup>c</sup>
Median $W1$ (mag)	15.9	15.6
Median $i$ (mag)	19.8	19.4 <sup>d</sup>
Inside MIR wedge (equation 1)	100%	70%
With spectroscopic redshift	83%	79%
Median spectroscopic- $z$	1.8	1.7

NOTE—*a*: Includes SALT-NOT sample. *b*: 70 at  $\delta < -40^\circ$  selected using SUMSS. The remaining at  $\delta > -40^\circ$  are based on NVSS. *c*: Estimated at 1.4 GHz. SUMSS 0.850 MHz flux densities computed at 1.4 GHz assuming  $\alpha = -0.8$ . *d*: Only  $\sim 550$  targets overlapping with PS1 considered. Note slight increase in the  $i$ -band brightness due to the inclusion of redshifts from the literature.

## 6. SUMMARY AND OUTLOOK

In this paper, we describe a large spectroscopic survey of radio bright AGN selected based on the following criteria: (i) radio flux density at 1.4 GHz  $> 200$  mJy; (ii)  $\delta < +20^\circ$ ; and (iii) WISE MIR-colors:  $W1 - W2 < 1.3 \times (W2 - W3) - 3.04$  and  $W1 - W2 > 0.6$ . These criteria are optimized to select powerful quasars at  $z > 1.4$ . Starting from 25,325 sources brighter than 200 mJy in NVSS we identify 2011 candidate quasars, of which 303 were observed with SALT (180 hrs) and NOT (6 nights; Krogager et al. 2018).

The SALT–NOT sample of 303 objects presented in this paper consists of (i) AGN with emission lines in the optical spectrum (250); (ii) objects with no emission lines in the optical spectrum, i.e., emission line less (ELLs; 26); and (iii) dark fields (DFs; 27), i.e., neither emission lines nor a continuum source in the optical spectra or photometry (also see Table 2).

We compare the SALT–NOT sample with the highly complete spectroscopic sample of 10,498 quasars from the SDSS (DR16) in the so-called ‘Stripe 82’ region, and with a *reference* sample of 2294 AGN from SDSS selected by applying the same constraints on the radio flux density and MIR colors as the SALT–NOT sample. We show that our imposed WISE criteria has lead to a sample of radio-bright quasars which are fainter ( $\Delta i = 0.6$  mag) and redder ( $\Delta(g - i) = 0.2$  mag) than radio-selected quasars in the *reference* sample, and rep-

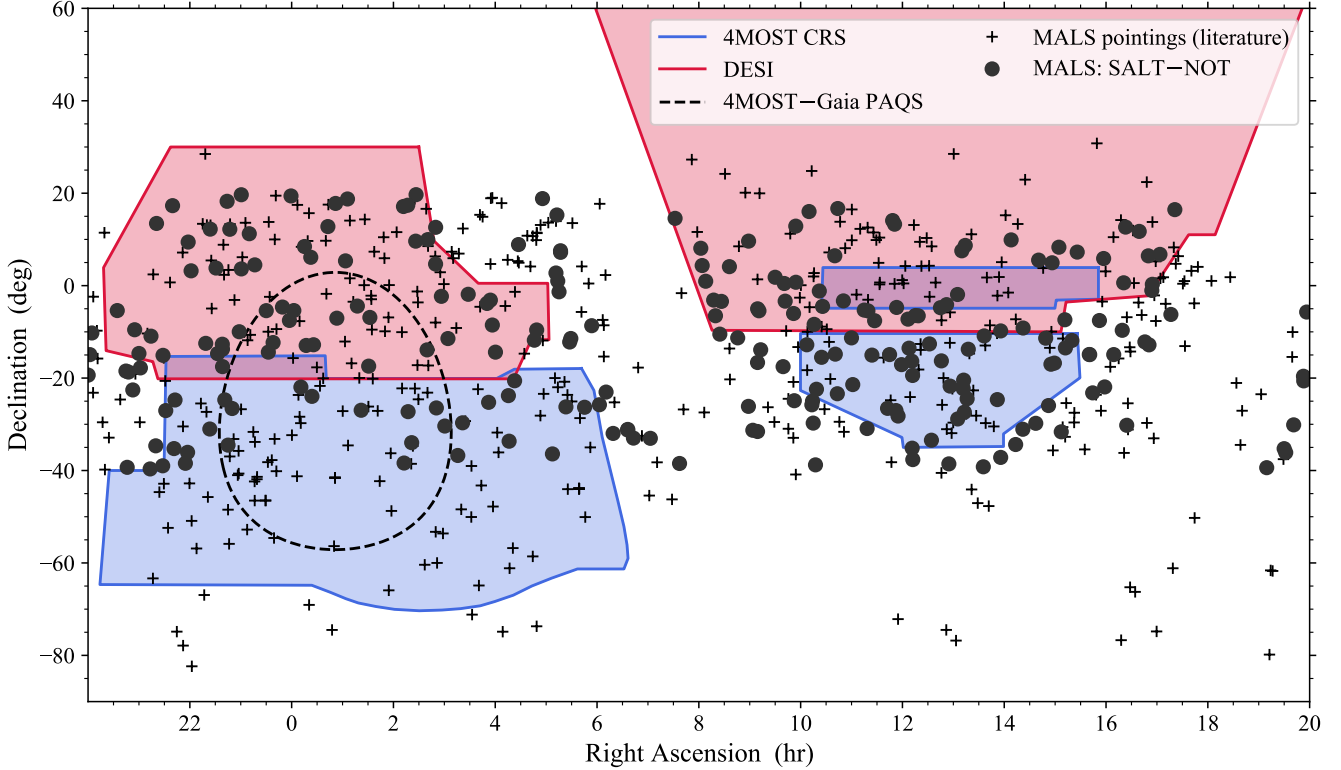


**Figure 13.** Compilation of MALS pointings from the literature (black crosses) and from our dedicated SALT and NOT observations (solid circles). Overlaid are the footprints of a few upcoming spectroscopic surveys: DESI (red), 4MOST Cosmology Redshift Survey (CRS; blue) and the 4MOST–Gaia Purely Astrometric Quasar Survey (PAQS; black dashed line). Note that ESO’s 4MOST–Gaia PAQS survey (PI: Krogager) will observe 120,000 targets over 5 years.

representative of a fainter quasar population detected in optical surveys.

About 20% (51/303) of the AGN in our sample only have narrow emission lines. The majority of these (33/51) at  $z < 0.5$ , are galaxies without strong nuclear emission. In two cases the emission line is double peaked and likely corresponds to rare dual AGN. The highest redshift NLAGN (M1513–2524) is at  $z = 3.132$ . The details of this optically faint ( $r > 23$  mag) AGN associated with a large ( $\sim 90$  kpc) and luminous Ly $\alpha$  nebula are presented by Shukla et al. (2021a). The double-lobed radio emission associated with M1513–2524 has an extent of 184 kpc. In general, the NLAGN in our sample exhibit extended radio emission with lobes and in some cases cores – the largest being M0909–3133 ( $z_{em} = 0.884$ ) with a projected linear size of 330 kpc.

Based on the *reference* sample, we expect only 5% of objects in the SALT–NOT sample to be NLAGN. The discrepancy is primarily due to the  $z < 0.5$  contaminants. Excluding these would render the  $z$ -distribution and broad- vs. narrow-line AGN composition of the SALT–NOT sample identical to the *reference* sample. Overall, the application of our WISE-color criteria im-

proves the efficiency of identifying  $z > 1.4$  AGN by a factor of  $\sim 1.7$  (i.e., from  $\sim 30\%$  to  $\sim 50\%$ ).

We discuss in detail the properties of the 110 SALT–NOT AGN at  $1.9 < z < 3.5$ . The four NLAGN in this sub-sample show emission line ratios similar to high- $z$  radio galaxies. The radio emission associated with two of these (M1315–2745 and M1513–2524) are among the largest at these redshifts (280 and 184 kpc, respectively). We estimate Bolometric luminosities, radio-loudness parameters ( $R = f_{5\text{GHz}}/f_{2500\text{\AA}}$ ), black hole masses ( $M_{\text{BH}}$ ) and Eddington ratios of the remaining 106 AGN in this sub-sample. In comparison to the optically selected core-dominated SDSS quasars from Shen et al. (2011), the SALT–NOT quasars are fainter ( $\sim 0.5$  dex lower  $L_{1350}$ ) and, consequently, have lower ( $\sim 0.4$  dex)  $M_{\text{BH}}$ . It is intriguing to note that despite representing the most radio-loud quasars (median  $R = 3685$ ), the Eddington ratios of our objects are similar to the less radio-loud (median  $R = 100$ ) SDSS quasars. In fact, we do not find any dependence between radio loudness and Eddington ratio in the SALT–NOT and SDSS quasar samples spanning four orders of magnitude in  $R$ . This confirms the saturation of radio loudness observed at

low Eddington ratios (Sikora et al. 2007), and the significance of physical parameters such as black hole spin and the in-situ magnetic field in influencing the overall appearance of AGN.

Among  $1.9 < z < 3.5$  AGN, we also detect 4 C IV BAL quasars. All are associated with objects of least radio loudness, and highest BH masses and Eddington ratios. The low BAL quasar detection rate ( $4^{+3}_{-2}\%$ ) is consistent with that seen in extremely powerful ( $L_{1.4GHz} > 10^{25}$  W Hz $^{-1}$ ) radio loud quasars (Shankar et al. 2008). The systematic H I 21-cm absorption line search in these quasars suggests deficiency of cold atomic gas at host galaxy scales (Gupta et al. 2021b). In this context, it will be interesting to confirm the slight excess of proximate DLAs observed in our sample (Gupta et al. 2021b). The details of gaseous environment of these quasars at larger ( $> 10$  kpc) scales are presented in a separate paper (Shukla et al. 2021b).

Based on detailed optical variability analysis, radio polarization and  $\gamma$ -ray properties we identify 7 high-probability BL Lacs among 26 ELLs in our sample. Better quality optical spectra will likely confirm a larger fraction of these ELLs as bona fide BL Lacs. Finally, we discuss 27 DFs in our sample which could be due to (i) an intrinsically low luminosity; (ii) very large amounts of dust in the foreground (intrinsic or intervening) or (iii) a very high redshift ( $z > 5$ ) such that the continuum is strongly absorbed by the intervening Ly $\alpha$  forest and emission lines are redshifted into the near-infrared; or (iv) a non-quasar origin of the radio/MIR emission.

The selection criteria of SALT-NOT sample are based on the requirements of MALS. The entire MALS footprint of  $\sim 500$  pointings each at L and UHF bands is based on the SALT-NOT sample presented here and additional  $\sim 350$  bright radio sources selected from the literature. The overall properties of this larger pool of 650 AGN are presented in Table 2 (see also Fig. 13 for the survey footprint and overlap with various optical surveys).

The complete details of the MALS sample will be provided in future papers. But, in short, these additional sources are AGN: (i) with known spectroscopic redshift and  $\delta > -40^\circ$  from the literature (see Fig. 1 i.e., the green box with 597 AGN), and (ii) brighter than 200 mJy at 843 MHz and  $\delta < -40^\circ$  in the SUMSS

(Mauch et al. 2003). Further, priority has been given to AGN having excellent multi-wavelength data or close to nearby ( $z < 0.1$ ) galaxies. This extended sky coverage through a larger pool of 650 sources offers flexibility in selecting pointings for the observations, and maximising the scientific output corresponding to various galaxies and AGN detected within the MALS field-of-view (see Gupta et al. 2017, for some of the science cases).

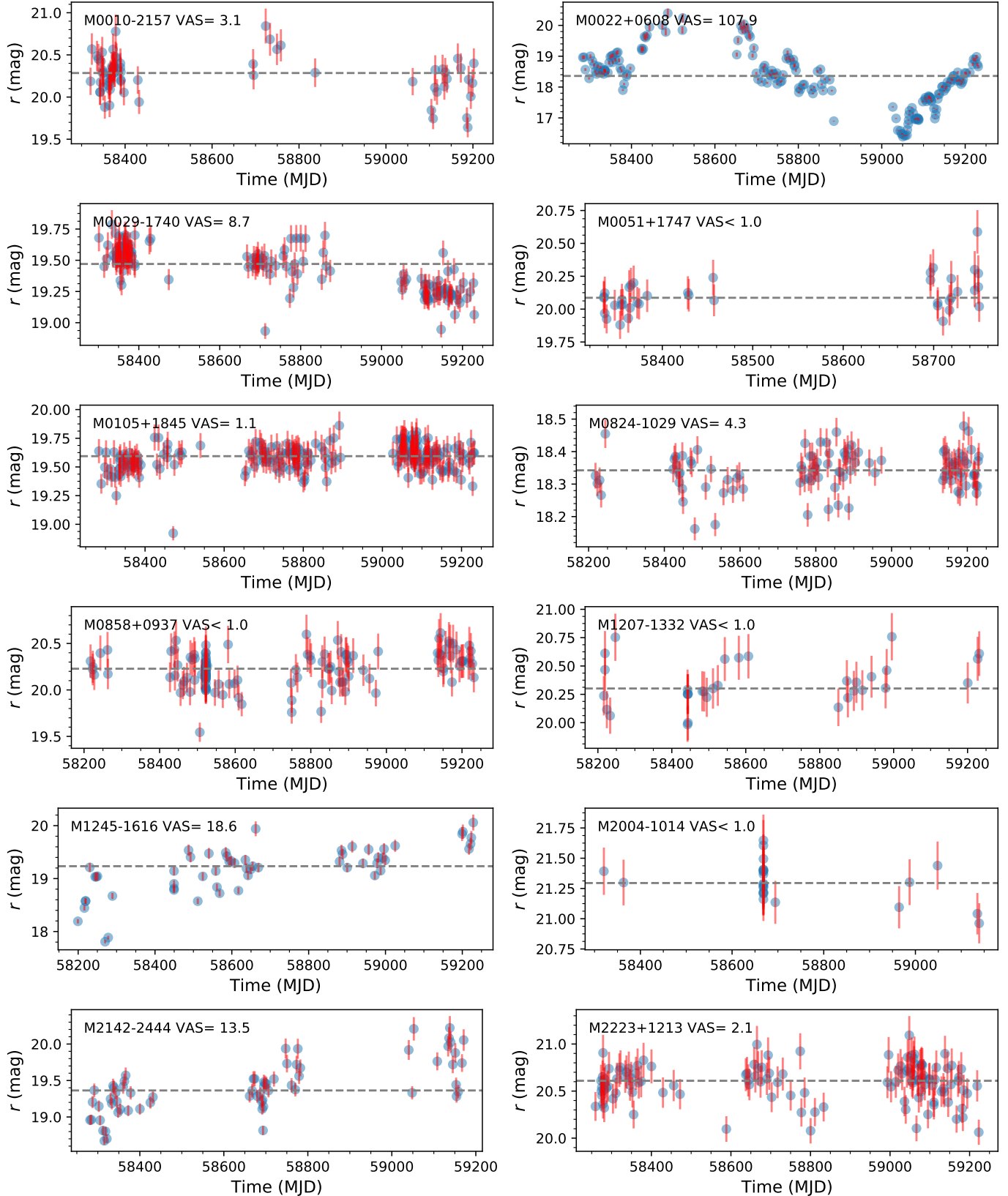
Currently,  $\sim 400$  pointings mostly at L band have already been observed (Fig. 13). Looking forward, MALS will continue to observe with the MeerKAT through 2021-22 and afterwards primarily in the UHF band. We plan to release all radio continuum images and spectra along with the catalogs of detected sources and spectral lines through our survey website: <https://mals.iucaa.in>. This will include multi-wavelength data such as the SALT-NOT spectra presented here. We expect all these to be an excellent resource for the astronomical community for a broad range of galactic and extragalactic applications.

We thank the anonymous referee for useful comments and suggestions. PPJ was supported in part by the French National Research Agency (ANR) under contracts ANR-16-CE31-0021. PPJ thanks Camille Nôus (Laboratoire Cogitamus) for inappreciable and often unnoticed discussions, advice, and support. This work is based on observations made with SALT and NOT. We thank NOT and SALT staff for their support during the observations. The National Radio Astronomy Observatory is a facility of the National Science Foundation operated under cooperative agreement by Associated Universities, Inc. Based on observations obtained with the Samuel Oschin Telescope 48-inch and the 60-inch Telescope at the Palomar Observatory as part of the Zwicky Transient Facility project. ZTF is supported by the National Science Foundation under Grant No. AST-2034437 and a collaboration including Caltech, IPAC, the Weizmann Institute for Science, the Oskar Klein Center at Stockholm University, the University of Maryland, Deutsches Elektronen-Synchrotron and Humboldt University, the TANGO Consortium of Taiwan, the University of Wisconsin at Milwaukee, Trinity College Dublin, Lawrence Livermore National Laboratories, and IN2P3, France. Operations are conducted by COO, IPAC, and UW.

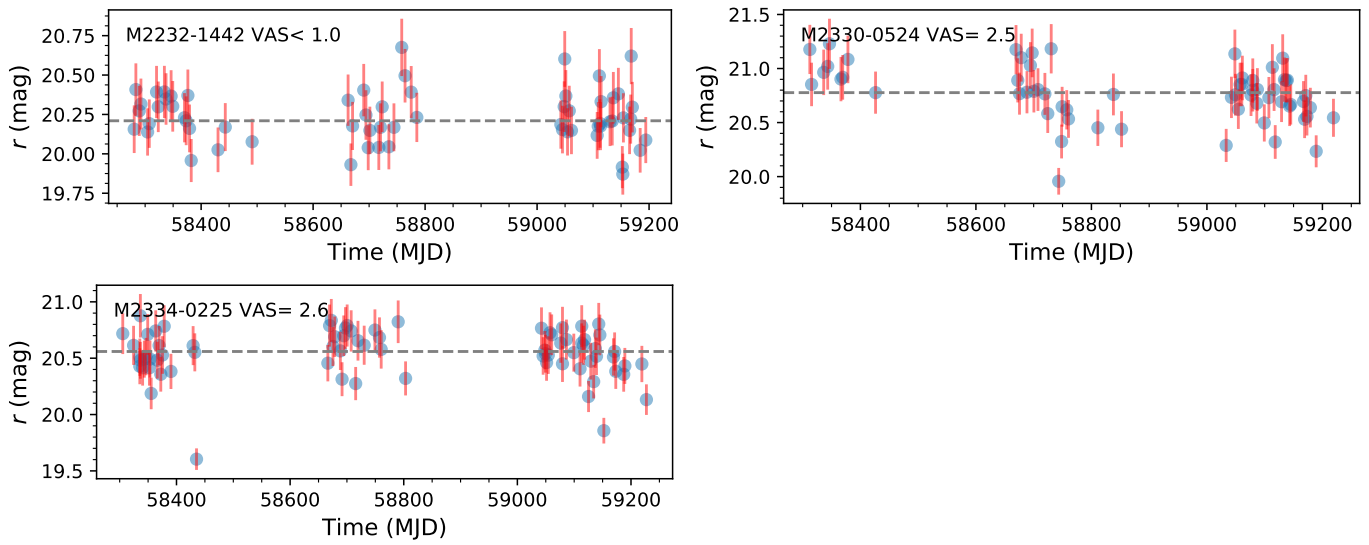
## APPENDIX

### A. PROPERTIES OF MALS SALT-NOT SAMPLE

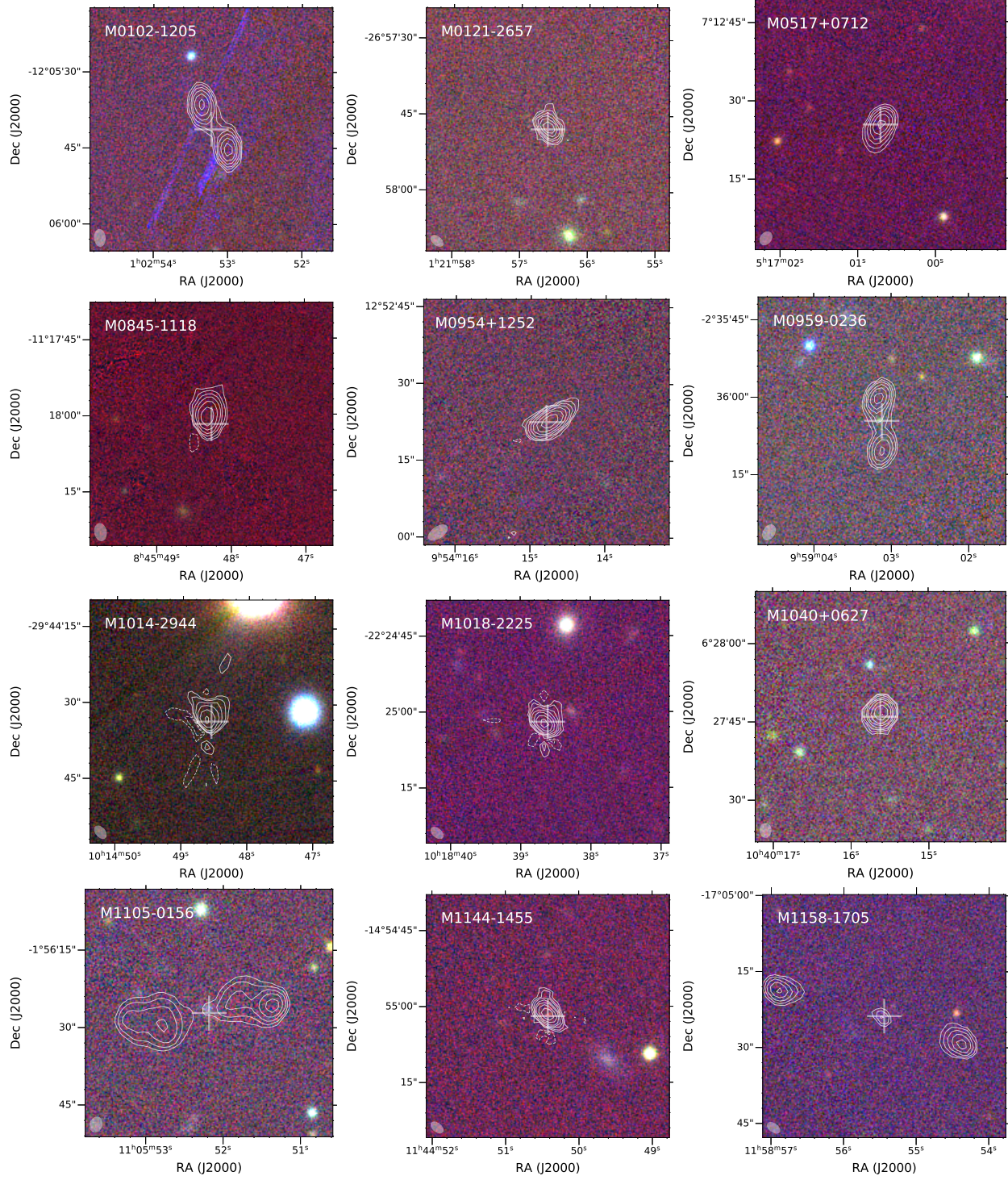
The properties of AGNs in the SALT-NOT sample are provided here. The ZTF light curves and radio-optical overlays for ELLs and DFs, respectively, are also provided.



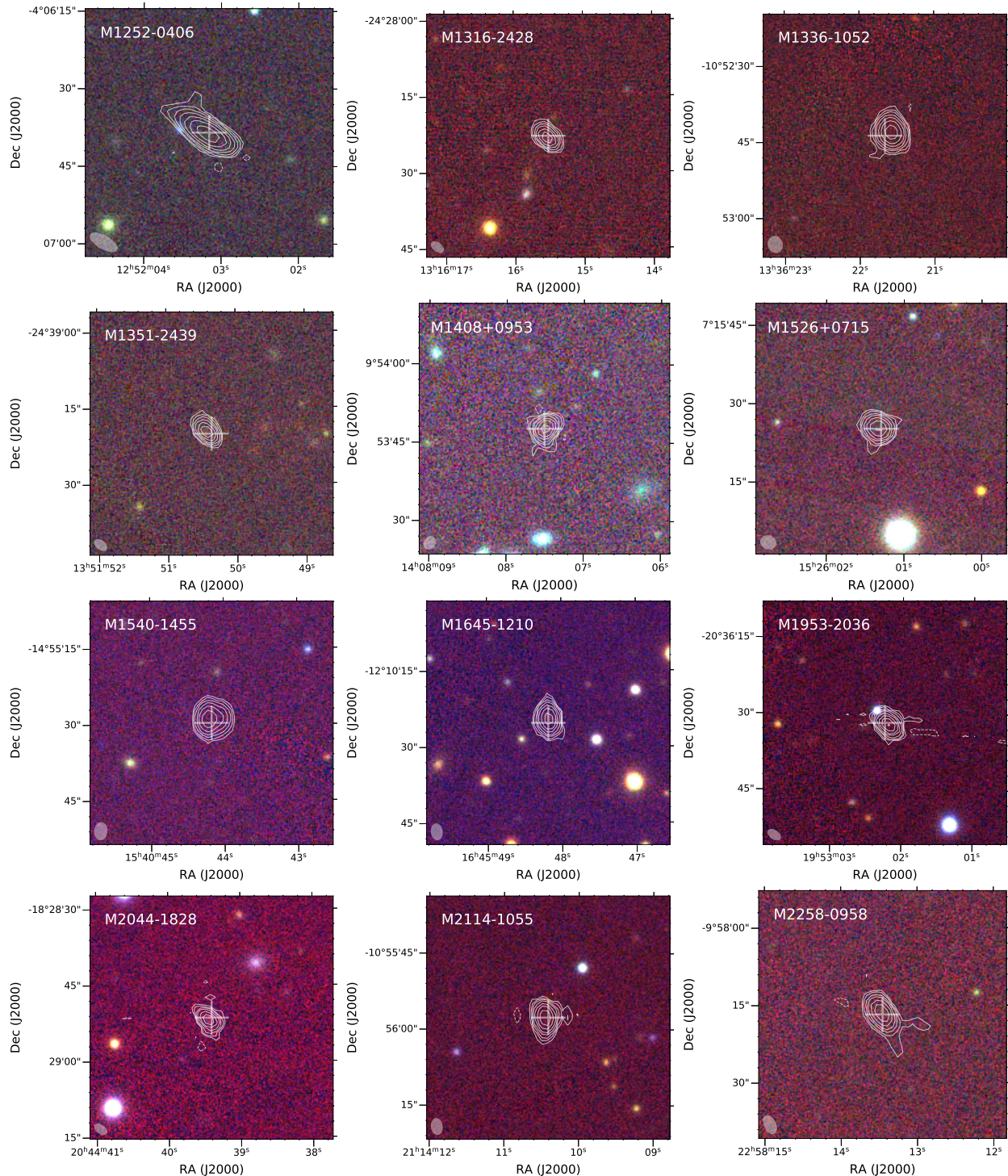
**Figure A.1.** ZTF light curves ( $r$ -band) and the variability amplitude strength (VAS) for targets with no emission lines. The horizontal dashed line represents the median value.



**Figure A.1** *continued.*



**Figure A.2.** VLASS (3 GHz) contours overlaid on PS1 *yig* color composite images. The contour levels are shown at  $1.5 \times (-1, 1, 2, 4, 8, \dots)$  mJy beam $^{-1}$ . The synthesized beam is shown at the bottom left corner. The position of WISE source is marked with a cross.

**Figure A.2** *continued.*

**Table 3** Sample of radio sources for the uGMRT survey.

NVSS-ID	Flux	$B_{maj}$	$B_{min}$	$B_{pa}$	Redshift	Telescope	AGN-type	
WISE-ID	$R_{AW}$	$Dec_W$	W1	$\delta W_1$	W2	$\delta W_2$	W3	$\delta W_3$
PS1-ID	nStackDets	nDetections	g	$\delta g$	r	$\delta r$	i	$\delta i$
(1)	(2)	(3)	(4)	(5)	(6)	(7)	(8)	$\delta y$
(9)	(10)	(11)	(12)	(13)	(14)	(15)	(16)	(17)
(18)	(19)	(20)	(21)	(22)	(23)	(24)	(25)	(26)
(27)	(28)	(29)	(30)					
Spectra with emission lines (250)								
M000234.52-052324.5	235.4	<16.7	<15.9	-	0.306	SALT	G	
PSO J000234.55-052324.0	0.6439997	-5.3900227	15	0.04	14.18	0.05	10.96	0.14
PSO J000.6440-05.3900	5	77	21.26	0.08	20.31	0.02	19.95	0.02
M000920.42-074057.5	269.9	<18.8	<16.7	-	1.672	SALT	Q	
PSO J000920.43-074057.3	2.3351346	-7.6826025	16.26	0.07	15.07	0.09	11.65	0.25
PSO J002.3351-07.6826	5	76	20.16	0.02	19.97	0.02	19.47	0.03
M000923.07-282153.9	205.8	<19.0	<18.0	-	1.796	SALT	Q	
PSO J000923.18-282152.0	2.3466024	-28.3644449	15.77	0.05	14.51	0.06	11.19	0.15
PSO J002.3465-28.3645	10	65	20.02	0.02	19.34	0.02	18.92	0.01
M001508.49+082803.8 <sup>a,b</sup>	384	<18.6	<17.4	-	1.710	SALT	Q	
PSO J001508.62+082802.2	3.7859185	8.4672841	15.06	0.04	14.26	0.05	10.95	0.14
PSO J003.7858+08.4674	5	49	19.46	0.02	19.02	0.04	18.67	0.02
M001708.03-125624.9	929.7	<17.1	<16.1	-	0.883	SUGAR	G	
PSO J004.2842-12.9405	5	74	20.46	0.04	19.68	0.03	9.51	0.05
PSO J004.2842-12.9405	211	<17.6	<16.3	-	1.442	SALT	Q	
J002355.79-235719.3	5.9824792	-23.9553806	16.32	0.07	15.41	0.10	12.04	0.31
PSO J005.9820-23.9555	5	44	21.82	0.1	21.13	0.05	20.79	0.04
M002355.84-235717.8 <sup>a,b</sup>								
J002546.68-124724.9	394.4	<17.2	<15.3	-	0.770	SALT	Q	
PSO J006.4444-12.7904	8	22	-999	0.05	15.21	0.10	11.77	-
PSO J006.4444-12.7904	635	<18.3	<16.2	-	2.150	NOT	Q	
M004243.06+124657.6	J004243.02+124657.2	10.6792742	12.7825612	15.78	0.05	14.54	0.07	11.13
								0.17

*Table 3 continued*

Table 3 (continued)

SALT-NOT SURVEY OF MIR-SELECTED AGN												
NVSS-ID	Flux	B <sub>maj</sub>	B <sub>min</sub>	B <sub>pa</sub>	Redshift	Telescope	AGN-type	W3	δW3	W2	δW2	DecW
WISE-ID	R <sub>Aw</sub>	W1	δW1	r	δr	i	δi	z	δz	y	δy	nStackDets
(1)	(2)	(3)	(4)	(5)	(6)	(7)	(8)					
(9)	(10)	(11)	(12)	(13)	(14)	(15)	(16)	(17)				
(18)	(19)	(20)	(21)	(22)	(23)	(24)	(25)	(26)	(27)	(28)	(29)	(30)
M005315.65-070233.4	PSO J010.6793+12.7826 248.2 <17.7	10	68	20.12	0.03	19.95	0.04	19.54	0.02	19.41	0.04	19.28
J005315.67-070232.5	13.3153062 PSO J013.3154-07.0424	5	-7.0423807 <16.0	16.31 65	0.07 20.83	15.25	0.10	11.95	0.3			
M010329.05+052131.2	589.1 J010329.05+052132.4	15.871081 PSO J015.8710+05.3588	5 <18.2	5.3590232 74	0.09 20.87	15.57	0.12	11.79	-			
M010628.74-343409.0	259.8 J010628.71-343410.5	16.6196616 -	<16.0 -	-	0.04 0.116	20.68	0.06	20.14	0.02	19.99	0.03	19.89
M011727.84-042511.5	421.4 J011727.86-042510.4	<19.2 19.3661239	<16.8 -4.4195713	16.05 66	0.06 20.3	1.720 0.04	NOT -	-	-	-	-	-
M013047.38-172505.6	250.3 J013047.31-172506.2	<17.5 22.697147	<16.1 -17.4183991	-	2.528	SALT	Q					
M013212.20-065236.8*c	1258.9 J013212.24-065236.0	<18.3 23.0510009	<16.2 -6.8766872	42 15.95	0.04 0.05	16.01 1.511	0.18	12.09	-			
M013355.99-025635.2	270.2 J013355.91-025633.3	<19.2 23.4829682	<16.9 -2.9426108	-	0.261	SALT	Q					
M013721.79+072059.0	314.8 PSO J023.4830-02.9426	5 44.7	73 <18.4	13.58 3.3	0.03 0.255	12.67	0.03	9.56	0.04			
PSO J024.3406+07.3495	0	7	7.3494561	14.35	0.03	13.29	0.03	10.03	0.05			
M015647.53-361608.3	1296.9 J015647.59-361610.1	<16.6 29.1983255	<16.4 -36.2694836	-	-	-	-	-999	19.87	0.14	19.36	0.07
	-	-	-	-	-	-	-	-	-	-	-	-

Table 3 continued

**Table 3 (continued)**

NVSS-ID	Flux	$B_{maj}$	$B_{min}$	$B_{pa}$	Redshift	Telescope	AGN-type	
WISE-ID	$R_{Aw}$	$Dec_W$	W1	$\delta W1$	W2	$\delta W2$	W3	$\delta W3$
PS1-ID	nStackDets	nDetections	g	$\delta g$	r	$\delta r$	i	$\delta i$
(1)	(2)	(3)	(4)	(5)	(6)	(7)	(8)	
(9)	(10)	(11)	(12)	(13)	(14)	(15)	(16)	(17)
(18)	(19)	(20)	(21)	(22)	(23)	(24)	(25)	(26)
J021148.77+170723.2	539.8	<19.3	<17.9	-	1.980	NOT	Q	
	J021148.78+170722.6	32.9532841	17.1229521	16.22	0.06	15.42	0.10	11.82
	PSO J032.3532+17.1230	5	45	20.24	0.07	20.12	0.03	19.88
M021231.86-382256.6	244.5	<18.6	<16.4	-	2.260	SALT	Q	
	J021231.72-382256.9	33.1321971	-38.382499	17.16	0.09	16.33	0.15	12.32
	-	-	-	-	-	-	-	-
M021650.70+172404.9	395.2	<17.5	<17.2	-	1.530	NOT	Q	
	J021650.74+172405.7	34.2114448	17.4016026	15.99	0.06	15.09	0.10	11.91
	PSO J034.2114+17.401	5	54	20.73	0.05	20.16	0.04	19.8
M021715.31-271555.4	265.1	<18.7	<15.3	-	1.950	SALT	Q	
	J021715.33-271555.4	34.3138823	-27.265405	16.7	0.07	15.54	0.09	12.09
	PSO J034.3138-27.2654	5	62	19.91	0.01	19.84	0.02	19.61
M022128.93-335527.0	219.8	<17.9	<16.0	-	0.524	SALT	Q	
	J022128.90-335526.8	35.3704341	-33.9741367	15.67	0.04	14.29	0.05	10.33
	-	-	-	-	-	-	-	-
M022613.72+093726.3	374.6	<17.1	<16.4	-	2.605	SUGAR	Q	
	J022613.71+093726.7	36.5571491	9.6240874	15.03	0.04	14.11	0.05	10.74
	PSO J036.55571+09.6241	5	55	18.33	0.01	18.01	0.01	17.89
M022639.92+194110.1	209.8	<15.9	<14.0	-	2.190	NOT	Q	
	J022639.93+194110.5	36.6663794	19.686268	16.52	0.09	15.46	0.12	11.9
	PSO J036.6665+19.6862	5	69	20.46	0.02	20.36	0.02	20.06
M022924.85-243600.9 <sup>a,b</sup>	276.7	14.1	<17.6	68.1	2.003	SALT	Q	
	J022924.93-243600.9	37.35338803	-24.6002552	16.04	0.05	15.28	0.07	12.21
	PSO J037.3539-24.6003	5	11	-999	-999	-999	21.61	0.04
M023939.11-135409.4	214	<18.3	<16.6	-	1.947	SALT	Q	
	J023939.14-135409.5	39.9131075	-13.9026396	16.04	0.05	14.95	0.06	11.66
	PSO J039.9130-13.9026	5	44	19.66	0.02	19.55	0.02	19.38
M024027.19+095713.0	521.2	14.7	<19.0	-50.1	1.874	SALT	Q	

Table 3 continued

**Table 3 (continued)**

NVSS-ID	Flux	$B_{maj}$	$B_{min}$	$B_{pa}$	Redshift	Telescope	AGN-type	
WISE-ID	$R_{Aw}$	$Dec_W$	W1	$\delta W1$	W2	$\delta W2$	W3	$\delta W3$
PS1-ID	nStackDets	nDetections	g	$\delta g$	r	$\delta r$	i	$\delta i$
(1)	(2)	(3)	(4)	(5)	(6)	(7)	(8)	
(9)	(10)	(11)	(12)	(13)	(14)	(15)	(16)	(17)
(18)	(19)	(20)	(21)	(22)	(23)	(24)	(25)	(26)
							(27)	(28)
							(29)	(30)
M024046.80+083258.3	J024027.16+095713.4 PSO J040.1135+09.9537	40.113197 5	9.9537378 44	16.36 21.01	0.07 0.05	15.49 20.98	0.12 0.04	12.43 20.48
		305.4	<19.6	<16.4	-	1.100	NOT Q	0.05 -999
M024106.56-171640.3	J024046.81+083259.9 PSO J040.1951+08.5500	40.1950492 5	8.5499839 61	15.57 19.74	0.04 0.02	14.59 19.41	0.06 0.01	11.49 19.2
		453.9	<17.7	<16.6	-	0.365	SALT G	0.21 0.01
M024939.93+044028.9	J024106.57-171641.5 PSO J040.2774-17.2782	40.2774033 5	-17.2782204 81	15.26 21.03	0.04 0.07	14.64 19.88	0.05 0.02	11.81 19.62
		420.5	<17.0	<16.2	-	2.008	SUGAR Q	0.25 0.02
M025035.54-262743.1	J024939.97+044028.3 PSO J042.4165+04.6745	42.4165498 5	4.6745332 60	16.15 20.61	0.06 0.03	15.10 20.32	0.07 0.06	11.68 19.88
		389.2	<16.6	<15.3	-	2.918	SALT Q	0.19 0.01
M025630.36-021844.5	J025035.56-262742.4 PSO J042.6482-26.4618	42.6481981 5	-26.4617331 78	16.08 19.1	0.05 0.01	15.06 18.97	0.07 0.02	11.63 18.9
		260.3	<17.3	<15.6	-	1.970	NOT Q	0.16 0.02
M030032.15-302243.8	J025630.37-021844.2 PSO J044.1296-02.3123	44.1265641 5	-2.312278 72	15.21 18.85	0.03 0.03	13.88 18.63	0.04 0.01	10.27 18.46
		371.4	<16.6	<15.4	-	0.310	SALT G	0.06 0.01
M030413.80-112653.5	J030032.19-302242.4 -	45.1341357 -	-30.37846 -	14.66 -	0.03 -	13.8 -	10.26 -	0.05 -
		335	<16.6	<15.3	-	1.552	SUGAR Q	0.12 -
M031022.90+055552.6	J030413.74-112653.3 PSO J046.0574-11.4480	46.0572895 5	-11.4481531 82	16.98 20.33	0.09 0.02	15.84 20.02	0.12 0.03	12.34 19.76
		200.5	21.2	<17.8	52.5	0.399	SALT G	0.04 0.04
M031407.94-090946.9	J031023.01+055552.4 PSO J047.5959+05.9313	47.5958935 5	5.9312433 49	15.12 -999	0.03 21.17	13.89 0.07	10.27 20.35	0.08 0.03
		226.8	44.5	<18.7	84.1	0.312	NOT G	19.63 20.12
		J031407.90-090948.5	48.532931	-9.1634772	15.25	0.04	14.61	0.05
							11.72	0.24

Table 3 continued

**Table 3 (continued)**

NVSS-ID	Flux	$B_{maj}$	$B_{min}$	$B_{pa}$	Redshift	Telescope	AGN-type	
WISE-ID	$R_{Aw}$	$Dec_W$	W1	$\delta W1$	$W2$	$\delta W2$	W3	$\delta W3$
PS1-ID	nStackDets	nDetections	g	$\delta g$	r	$\delta r$	i	$\delta i$
(1)	(2)	(3)	(4)	(5)	(6)	(7)	(8)	
(9)	(10)	(11)	(12)	(13)	(14)	(15)	(16)	(17)
(18)	(19)	(20)	(21)	(22)	(23)	(24)	(25)	(26)
(18)	(19)	(20)	(21)	(22)	(23)	(24)	(25)	(26)
(18)	(19)	(20)	(21)	(22)	(23)	(24)	(25)	(26)
M031551.28-364450.8	PSO J048.5329-09.1635	10 462.4	<19.6 48.9639505	64 <15.6 -36.7469393	21.38 15.8	0.07 0.04	20.1 14.84	0.02 0.05
	J031551.34-364448.9	-	-	-	-	-	-	19.67 11.74
M031706.76+065550.3	247.9	23.9	<17.2	70.8	0.275	NOT	G	0.17 -
	J031706.74+065549.6	49.2781024	6.9304589	14.78 61	0.03 21.41	14.12 0.08	0.05 20	11.13 0.04
PSO J049.2781+06.9305	5	5	<16.5	<15.6	-	0.583	SALT	0.16 19.46
M032128.78-294047.4 <sup>a,d</sup>	2061.7	<16.5	-29.6795529	13.97	0.03	12.85	Q	0.02 18.95
	J032128.80-294046.3	50.3700396	50	20.68	0.02	19.96	Q	0.04 0.04
PSO J050.3701-29.6796	5	<18.3	<15.9	-	2.679	SUGAR	Q	0.03 18.98
M032808.59-015220.2	221.9	52.0361812	-1.8725096	15.46	0.04	14.55	Q	0.03 0.02
	J032808.68-015221.0	5	76	18.7	0.01	18.53	Q	18.83 19.32
PSO J052.0363-01.8726	200.4	<17.5	<15.1	-	1.699	NOT	Q	0.02 0.02
J034157.69+151925.5	230.5	55.4903908	15.3236243	16.32	0.08	15.22	0.09	11.77 20.18
	PSO J055.4904+15.3235	5	60	20.87	0.05	20.58	0.04	- 0.05
M034157.75+151925.5	J035016.85-035111.3	57.5702271	-3.8531559	15.21	0.04	14	0.04	18.48 18.36
	PSO J057.5702-03.8632	5	75	19.25	0.02	19.06	0.02	0.01 0.01
M035016.86-035111.3	J035211.06-251449.8	<17.0	<16.4	-	1.675	SALT	Q	18.33 20.04
	PSO J058.0461-25.2473	5	73	19.52	0.02	13.68	0.03	0.03 19.04
M035414.70-030804.3	725.6	<18.7	<18.1	-	0.442	SALT	G	19.85 10.12
	J035414.72-030804.8	58.5613708	-3.1346696	14.79	0.03	13.98	0.04	0.06 10.82
PSO J058.5614-03.1348	5	58	20.58	0.03	19.87	0.02	0.02 19.18	
M035633.46+190034.6	1051.3	<17.7	<17.0	-	1.480	NOT	Q	0.05 0.01
	J035633.48+190034.3	59.1395029	19.0095492	15.76	0.05	14.95	0.08	18.54 11.73
PSO J059.1394+19.0090	3	31	-999	-999	-999	-999	0.02 20.64	0.03 19.9
								0.05 19.42

Table 3 continued

Table 3 (continued)

NVSS-ID	Flux	$B_{maj}$	$B_{min}$	$B_{pa}$	Redshift	Telescope	AGN-type	
WISE-ID	$R_{Aw}$	$Dec_W$	W1	$\delta W1$	W2	$\delta W2$	W3	$\delta W3$
PS1-ID	nStackDets	nDetections	g	$\delta g$	r	$\delta r$	i	$\delta i$
(1)	(2)	(3)	(4)	(5)	(6)	(7)	(8)	
(9)	(10)	(11)	(12)	(13)	(14)	(15)	(16)	(17)
(18)	(19)	(20)	(21)	(22)	(23)	(24)	(25)	(26)
(19)	(20)	(21)	(22)	(23)	(24)	(25)	(26)	(27)
(20)	(21)	(22)	(23)	(24)	(25)	(26)	(27)	(28)
(21)	(22)	(23)	(24)	(25)	(26)	(27)	(28)	(29)
(22)	(23)	(24)	(25)	(26)	(27)	(28)	(29)	(30)
M035634.55-083121.3	239.7	<18.3	<16.8	-	1.447	NOT	Q	
	J035634.52-083122.3	59.1438555	-8.522875	16.52	0.08	15.34	0.10	11.84
	PSO J059.1439-08.5229	5	60	21.15	0.04	20.47	0.03	20.23
M040015.06-142328.0 <sup>c</sup>	409.7	<19.1	<15.8	-	1.136	SALT	Q	
	J040015.04-142328.2	60.0626992	-14.391167	15.81	0.05	15.16	0.08	12.11
	PSO J060.0627-14.3911	10	73	19.38	0.01	19.14	0.01	19.22
M041530.42-234750.2	262	<17.4	<16.0	-	0.366	SALT	G	
	J041530.38-234751.3	63.8765933	-23.7975834	15.59	0.04	14.8	0.06	11.61
	PSO J063.8767-23.7975	5	65	20.74	0.02	19.63	0.01	19.53
M041620.54-333931.3	264.1	<20.0	<15.8	-	3.045	SALT	Q	
	J041620.47-333931.6	64.0853255	-33.6587934	16.08	0.05	15.19	0.08	11.66
	-	-	-	-	-	-	-	-
M042248.53-203456.6	224.3	<17.2	<16.7	-	2.582	SALT	Q	
	J042248.43-203455.8	65.7017923	-20.5821781	16.73	0.08	15.96	0.14	12.09
	PSO J065.7019-20.5822	5	60	20.84	0.04	20.46	0.05	20.52
M042725.05+085330.3 <sup>c</sup>	937.7	<13.9	<13.9	-	1.215	SALT	Q	
	J042725.11+085329.9	66.8546587	8.8916425	15.91	0.06	14.9	0.08	11.64
	PSO J066.85346+08.8916	5	52	20.79	0.08	20.13	0.04	19.75
M044604.72-114813.4	273.8	<17.7	<15.8	-	1.668	SALT	Q	
	J044604.67-114812.8	71.5194971	-11.8035664	15.12	0.03	14.28	0.04	11.08
	PSO J071.5196-11.8035	5	82	18.78	0.01	18.52	0.01	18.22
M044849.48-093531.3	240.9	<17.9	<15.5	-	2.079	SALT	Q	
	J044849.47-093531.4	72.2061409	-9.5920798	14.57	0.03	13.64	0.03	10.27
	PSO J072.2061-09.5921	10	76	18.3	0	17.88	0.01	17.59
M045541.91+185010.9	328.1	<16.3	<14.5	-	0.548	NOT	Q	
	J045541.81+185009.1	73.9242412	18.8358874	14.61	0.04	13.86	0.04	10.79
	PSO J073.9245+18.8359	5	92	20.21	0.04	19.69	0.01	19.06
M050725.04-362442.9	212.4	<17.1	<14.7	-	2.930	SALT	Q	

SALT-NOT SURVEY OF MIR-SELECTED AGN

**Table 3 (continued)**

NVSS-ID	Flux	$B_{maj}$	$B_{min}$	$B_{pa}$	Redshift	Telescope	AGN-type	
WISE-ID	$R_{Aw}$	$Dec_W$	W1	$\delta W1$	W2	$\delta W2$	W3	$\delta W3$
PS1-ID	nStackDets	nDetections	g	$\delta g$	r	$\delta r$	i	$\delta i$
(1)	(2)	(3)	(4)	(5)	(6)	(7)	(8)	(9)
(10)	(11)	(12)	(13)	(14)	(15)	(16)	(17)	(18)
(19)	(20)	(21)	(22)	(23)	(24)	(25)	(26)	(27)
(28)	(29)	(30)						
J050725.06-362443.1	76.8544416	-36.411939	15.66	0.04	14.63	0.04	11.14	0.09
M051024.23-1955050.3	336.2	15.2	<16.6	89.5	0.472	NOT	G	-
PSO J051024.07-195949.9	77.6003298	-19.9971964	14.95	0.03	14.15	0.04	11.16	0.12
PSO J077.6003-19.9972	10	65	20.61	0.12	20.31	0.03	19.76	0.04
M051134.05+024416.0	351.4	<18.3	<17.1	-	1.366	SALT	Q	-
PSO J051134.13+024416.5	77.8922114	2.7379244	16.3	0.07	15.31	0.09	12.16	0.37
PSO J077.8921+02.7377	5	33	21.74	0.15	21.17	0.03	21.23	0.04
M051240.99+151723.8	966.5	<17.1	<15.3	-	2.568	NOT	Q	-
PSO J051241.02+151723.4	78.1709541	15.289858	15.53	0.05	14.45	0.06	10.99	0.19
PSO J078.1709+15.2899	5	78	20.3	0.06	19.75	0.06	19.62	0.05
M051340.03+010023.6	447	<19.0	<17.0	-	2.673	SALT	Q	-
PSO J051340.03+010021.7	78.4168243	1.0060487	15.73	0.05	14.88	0.07	11.56	0.27
PSO J078.4168+01.0060	10	87	19.14	0.01	18.83	0.01	18.8	0.02
M051511.18-012002.4	288.8	<17.5	<15.7	-	2.287	SALT	Q	-
PSO J051511.18-012001.9	78.7965932	-1.3338644	15.79	0.05	14.81	0.07	11.35	0.17
PSO J078.7965-01.3339	10	62	18.81	0.01	18.66	0	18.6	0.02
M051656.35+073252.7	231.7	<17.7	<16.4	-	2.594	SUGAR	G	-
PSO J051656.28+073251.6	79.2345275	7.5476931	14.18	0.03	13.53	0.03	10.65	0.15
M052318.55-261409.6	1354.9	<18.9	<15.7	-	3.110	SALT	Q	-
PSO J052318.50-261409.2	80.8270963	-26.2359125	14.65	0.03	13.91	0.04	10.79	0.09
PSO J080.8270-26.2360	10	90	18.83	0.01	18.71	0.01	18.63	0.01
M052744.71-121153.7	335.6	<17.7	<16.2	-	0.316	SALT	G	-
PSO J052744.69-121153.9	81.936226	-12.1983995	15.4	0.04	14.66	0.06	11.72	0.24
PSO J081.9362-12.1983	5	64	21.24	0.04	20.12	0.03	19.75	0.02
M052905.55-112607.5	455.8	<17.8	<16.0	-	1.007	SUGAR	Q	-
J052905.51-112607.8	82.2729967	-11.4355102	14.99	0.04	14.3	0.05	11.3	0.14

GUPTA ET AL.

**Table 3** (*continued*)

NVSS-ID	Flux	$B_{maj}$	$B_{min}$	$B_{pa}$	Redshift	Telescope	AGN-type	
WISE-ID	$R_{\text{Aw}}$	$Dec_W$	W1	$\delta W1$	$W2$	$\delta W2$	$W3$	$\delta W3$
PS1-ID	nStackDets	nDetections	g	$\delta g$	r	$\delta r$	i	$\delta i$
(1)	(2)	(3)	(4)	(5)	(6)	(7)	(8)	
(9)	(10)	(11)	(12)	(13)	(14)	(15)	(16)	(17)
(18)	(19)	(20)	(21)	(22)	(23)	(24)	(25)	(26)
							(27)	(28)
							(29)	(30)
M054518.09-261857.3	PSO J082.2730-11.4355 236.9	5 <19.3	61 <16.3	20.3 <16.3	0.07 -0.800	19.71 SALT	0.06 Q	19.52 0.02
J054518.01-261856.3	86.33250527	-26.3156623	15.71	0.04	14.81	0.06	11.73	0.23
PSO J086.3251-26.3156	5	53	19.69	0.06	19.52	0.04	19.6	0.03
M055007.33+002731.5	208.7 <17.6	<17.0	-	0.279	SALT	G	19.51	0.06
J055007.28+002731.6	87.5303628	0.4587796	14.06	0.03	13.13	0.03	9.98	0.06
PSO J087.5304+00.4588	5 280	64 <17.8	20.91 <15.4	0.03 -1.777	19.88 SALT	0.03 G	19.33 0.01	18.67 0.03
M055205.32-345956.6	J055205.47-345958.1	88.0227953	-34.9994984	17.78	0.18	16.28	0.16	12.62
M060248.09-254602.2 <sup>d</sup>	- 555.3	- <17.8	- <15.0	- -0.602	- SALT	- Q	- 0.2	- -
J060248.05-254602.6	90.7002434	-25.7673954	15.5	0.04	14.87	0.06	11.69	0.06
PSO J090.7002-25.7674	5	66	21.5	0.04	21.4	0.4	20.23	0.02
M060958.94+021727.1	201.5 <17.7	<17.0	-	0.174	SALT	G	20.07	0.05
J060958.97+021726.5	92.4957371	2.2907017	13.38	0.03	12.22	0.02	8.29	0.02
PSO J092.4957+02.2907	5	69	21.31	0.06	19.85	0.03	18.6	0.02
M061038.80-230145.6	360.2 <16.5	<16.0	-	2.829	SALT	Q	10.74	0.1
J061038.78-230145.7	92.66615979	-23.0293781	15.33	0.04	14.36	0.05	18.35	0
PSO J092.6616-23.0294	5	67	18.62	0.01	18.47	0	18.27	0.01
M061856.02-315835.2	346.1 J061856.00-315835.0	<16.5 94.7333346	<15.7 -31.97639	-	2.134 0.04	SALT 14.75	0.05	11.25
M063602.28-311312.5	262.1	<16.6	<14.3	-	- 2.654	- SALT	- Q	- -
J063602.35-311311.8	99.0098305	-31.2199453	13.88	0.03	12.77	0.03	9.39	0.03
M063613.53-310646.3	208 J063613.49-310644.1	<17.7 99.0562279	<15.4 -31.1122649	-	- 2.757	- SALT	- Q	- 12.37
	-	-	-	-	-	-	-	-

Table 3 *continued*

**Table 3 (continued)**

NVSS-ID	Flux	$B_{maj}$	$B_{min}$	$B_{pa}$	Redshift	Telescope	AGN-type	
WISE-ID	$R_{Aw}$	$Dec_W$	W1	$\delta W1$	W2	$\delta W2$	W3	$\delta W3$
PS1-ID	nStackDets	nDetections	g	$\delta g$	r	$\delta r$	i	$\delta i$
(1)	(2)	(3)	(4)	(5)	(6)	(7)	(8)	
(9)	(10)	(11)	(12)	(13)	(14)	(15)	(16)	(17)
(18)	(19)	(20)	(21)	(22)	(23)	(24)	(25)	(26)
(27)	(28)	(29)	(30)					
M065254.73-323022.6	322.1	25.4	<17.7	-34.8	2.239	SALT	Q	
	J065254.55-323020.7	103.2273249	-32.5057682	14.86	0.03	14.08	0.04	10.9
		-	-	-	-	-	-	-
M070249.30-330205.0	314.6	<16.9	<15.8	-	2.410	SALT	Q	
	J070249.28-330204.2	105.7053378	-33.0345087	16.36	0.06	15.57	0.10	11.91
		-	-	-	-	-	-	-
M073159.01+143336.3	316.5	<17.9	<15.8	-	2.632	NOT	Q	
	J073158.97+143335.8	112.9957193	14.5599667	15.49	0.05	14.76	0.07	11.01
	PSO J112.9958+14.5601	5	58	18.54	0.02	18.43	0.01	18.28
M073714.60-382841.9	219.3	14.2	<16.7	-17	2.107	SALT	Q	
	J073714.61-382839.3	114.3108811	-38.4776064	15.41	0.04	14.19	0.04	10.88
		-	-	-	-	-	-	-
M073748.06-381259.0	2436.5	18.2	<18.9	35.4	0.318	SALT	G	
	J073748.12-381257.6	114.4505408	-38.2160133	14.25	0.03	13.14	0.03	9.9
		-	-	-	-	-	-	-
M080217.91+080525.4	210.5	<18.3	<15.9	-	0.995	SALT	Q	
	J080217.84+080524.7	120.5743551	8.0902184	16.24	0.07	15.44	0.11	12.45
	PSO J120.5743+08.0903	5	63	20.99	0.12	20.86	0.05	20.73
M080356.46+042102.8 <sup>c</sup>	318.1	<17.0	<16.4	-	1.252	SALT	Q	
	J080356.43+042102.6	120.9851521	4.3507431	15.27	0.04	14.14	0.04	10.86
	PSO J120.9852+04.3508	5	76	19.22	0.02	18.94	0.02	18.87
M080804.34+005708.2	317	<17.2	<16.5	-	3.133	SALT	Q	
	J080804.34+005707.6	122.0181055	0.9521212	15.31	0.04	14.38	0.05	10.58
	PSO J122.0181+00.9521	5	72	18.47	0.01	18.27	0.01	18.07
M081727.59-030737.7	502.7	<16.6	<15.4	-	1.785	SALT	Q	
	J081727.45-030737.2	124.3644078	-3.1270117	14.9	0.03	14.21	0.04	10.95
	PSO J124.3645-03.1270	5	42	18.61	0.08	18.69	0.01	18.25
M081936.62-063047.9 <sup>a</sup>	280	<18.1	<16.3	-	2.507	SALT	Q	

Table 3 *continued*

**Table 3 (continued)**

NVSS-ID	Flux	$B_{maj}$	$B_{min}$	$B_{pa}$	Redshift	Telescope	AGN-type	
WISE-ID	$R_{Aw}$	$Dec_W$	W1	$\delta W1$	$W2$	$\delta W2$	W3	$\delta W3$
PS1-ID	nStackDets	nDetections	g	$\delta g$	r	$\delta r$	i	$\delta i$
(1)	(2)	(3)	(4)	(5)	(6)	(7)	(8)	
(9)	(10)	(11)	(12)	(13)	(14)	(15)	(16)	(17)
(18)	(19)	(20)	(21)	(22)	(23)	(24)	(25)	(26)
							(27)	(28)
							(29)	(30)
	J081936.63-063048.4	124.9026465	-6.5134706	15.56	0.04	14.66	0.06	11.11
	PSO J124.9027-06.5134	5	65	19.79	0.06	19.88	0.03	19.38
M082638.44-032426.4	221.9	<18.3	<16.9	-	0.437	SALT	G	
	J082638.42-032427.2	126.6601067	-3.407575	15.49	0.04	14.77	0.07	11.63
M083601.35+040636.0	PSO J126.6601-03.4076	0	79	20.29	0.05	20.36	0.03	19.57
	435.3	<18.2	<15.7	-	0.743	SUGAR	G	
	J083601.33+040637.4	129.005552	4.1104025	15.52	0.05	14.91	0.07	11.86
M083601.35+040636.0	PSO J129.0057+04.1100	5	28	-999	-999	21.52	0.07	-
	919.2	48	<18.2	-63	0.160	SALT	G	
	J083608.56-134634.3	129.0356672	-13.6095406	14.01	0.03	13.18	0.03	9.82
M083608.59-133635.1	PSO J129.0356-13.6095	5	78	19.56	0.03	18.65	0.03	18.23
	404.5	<18.6	<17.2	-	2.036	SALT	Q	
	J085826.85-260720.9	134.6118804	-26.12249	15.47	0.04	14.33	0.04	11.04
M085826.92-260721.0	PSO J134.6118-26.1225	5	67	19.27	0.02	19.09	0.02	18.72
	209.5	<16.6	<15.7	-	1.670	SALT	Q	
M090337.99-311739.0	J090337.92-311739.0	135.9080123	-31.2941691	16.68	0.08	15.76	0.12	12.12
	-	-	-	-	-	-	-	-
M090910.66-163753.8	340.1	<15.7	<13.9	-	2.475	SUGAR	Q	
	J090910.56-163756.3	137.2940394	-16.6323287	15.87	0.06	15.2	0.09	11.84
M090911.33-313334.1	PSO J137.2937-16.6327	6	2	-999	-999	-999	-999	21.67
	610.1	50	<16.7	-65.4	0.884	SALT	G	
	J090911.50-313335.3	137.2979271	-31.5598218	16.98	0.1	16.27	0.19	12.63
	-	-	-	-	-	-	-	-
M090916.99-050053.2	457.2	<16.7	<15.4	-	0.404	SUGAR	G	
	J090917.01-050052.5	137.3208807	-5.0146108	15.68	0.05	15	0.08	11.75
M091051.01-052626.8	PSO J137.3209-05.0147	5	41	22.05	0.06	20.77	0.1	20.21
	337.9	15.8	<15.5	2.8	2.395	SUGAR	Q	
	J091050.99-052629.1	137.7124859	-5.4414291	14.57	0.03	13.61	0.04	10.46

Table 3 continued

**Table 3 (continued)**

NVSS-ID	Flux	$B_{maj}$	$B_{min}$	$B_{pa}$	Redshift	Telescope	AGN-type	
WISE-ID	$R_{Aw}$	$Dec_W$	W1	$\delta W1$	$W2$	$\delta W2$	$W3$	$\delta W3$
PS1-ID	nStackDets	nDetections	g	$\delta g$	r	$\delta r$	i	$\delta i$
(1)	(2)	(3)	(4)	(5)	(6)	(7)	(8)	(9)
(10)	(11)	(12)	(13)	(14)	(15)	(16)	(17)	(18)
(19)	(20)	(21)	(22)	(23)	(24)	(25)	(26)	(27)
(28)	(29)	(30)						
M091253.34-135241.9*c	PSO J137.7125-05.4414	5	83	18.24	0.01	18.03	0.02	17.86
	255.7	<16.5	<16.3	-	1.088	SALT	Q	0.01
J091253.36-135242.1	138.2223389	-13.8783827	15.62	0.04	14.98	0.07	11.9	0.24
PSO J138.2222-13.8785	5	38	21.29	0.07	20.83	0.09	20.62	0.13
M092902.69-293020.8	899.6	<18.8	<17.4	-	0.749	SALT	G	19.99
J092902.70-293019.9	142.2612874	-29.5053398	15.52	0.04	14.48	0.05	9.44	0.04
PSO J142.2613-29.5055	5	27	21.67	0.08	20.75	0.05	20.78	0.07
M092956.48+014843.8	248.7	<18.2	<17.2	-	2.331	SALT	Q	20.17
J092956.47+014844.2	142.485295	1.8123026	15.19	0.04	14.34	0.05	11.18	0.14
PSO J142.4852+01.8123	5	59	20.2	0.05	19.9	0.03	19.23	0.03
M093919.21-173135.4	263.3	<16.1	<15.3	-	1.831	SUGAR	Q	18.64
J093919.19-173135.6	144.8299719	-17.5265332	15.19	0.04	14.07	0.04	10.67	0.08
PSO J144.8300-17.5266	10	48	21.63	0.1	19.88	0.14	21	0.05
M094040.47-002800.1	359.3	<17.1	<16.1	-	2.383	SALT	Q	20.7
J094040.47-002801.4	145.1686386	-0.4670779	16.51	0.09	15.88	0.16	12	-
PSO J145.1686-00.4670	5	56	19.45	0.02	20	0.07	19.89	0.05
M094146.01-032121.7	346.2	<18.5	<17.5	-	1.848	SUGAR	Q	19.54
J094145.98-032121.7	145.4415998	-3.3560372	16.59	0.09	15.77	0.14	11.94	-
PSO J145.4417-03.3561	4	17	21.22	0.09	21.01	0.01	20.6	0.02
M095138.34-060138.0	378.8	<18.4	<16.1	-	1.844	SUGAR	Q	20.53
PSO J147.9098-06.0271	5	51	20.38	0.02	20.18	0.06	19.6	0.02
M095231.66-245349.1	209.5	<15.0	<14.0	-	2.626	SALT	Q	11.95
J095231.67-245351.0	148.1319654	-24.8975143	15.98	0.05	15.13	0.08	12.01	0.27
PSO J148.1319-24.8975	5	62	19.18	0.02	19.01	0.01	19.06	0.01
M095423.67+004350.5*b	291.6	<19.8	<17.6	-	1.712	SALT	Q	-999
J095423.72+004351.3	148.5988716	0.7309207	15.93	0.06	14.88	0.08	11.71	0.26
PSO J148.5989+00.7310	5	62	20.67	0.04	20	0.06	19.74	0.04
								19.63
								0.05
								19.52
								0.14

Table 3 continued

Table 3 (*continued*)

SALT-NOT SURVEY OF MIR-SELECTED AGN													
NVSS-ID	Flux	B <sub>maj</sub>	B <sub>min</sub>	B <sub>pa</sub>	Redshift	Telescope	AGN-type	W3	δW3	z	δz	y	δy
	WISE-ID	R <sub>AW</sub>	Dec <sub>W</sub>	W1	δW1	W2	δW2	i	δi				
(1)	PS1-ID	nStackDets	nDetections	g	δg	r	δr						
(2)	(3)	(4)	(5)	(6)	(7)	(8)							
(9)	(10)	(11)	(12)	(13)	(14)	(15)	(16)	(17)					
(18)	(19)	(20)	(21)	(22)	(23)	(24)	(25)	(26)	(27)	(28)	(29)	(30)	
M095654.60-131718.1*c	216	26	<16.6	-86.4	1.198	SALT	Q						
PSO J095654.65-131718.7	149.2277088	-13.2885524	16.19	0.05	15.24	0.08	12.04	0.48					
PSO J149.2276-13.2884	0	4	-999	-999	21.42	0.16	21.69	0.2	-999	-999	-999	-999	-999
M100715.18-124746.7	381.1	<15.7	<15.4	-	2.113	SALT	Q						
PSO J100715.22-124745.9	151.8134506	-12.7961	15.38	0.04	14.24	0.05	11.01	0.12					
PSO J151.8134-12.7961	10	74	18.4	0.01	18.28	0	18.18	0.01	18	0.01	18.07	0.02	
M100743.51-181732.4	205.2	49.2	<19.5	84.6	0.493	NOT	G						
PSO J100743.58-181731.1	151.9316084	-18.2919748	14.96	0.03	14.22	0.05	10.16	0.06					
PSO J151.9316-18.2919	5	60	21.56	0.06	20.37	0.05	19.63	0.03	19.54	0.04	19.29	0.03	
M100802.27-095919.3	645.3	15.7	<18.6	-82	1.688	NOT	Q						
PSO J100802.30-095919.8	152.0095896	-9.9888589	15.7	0.05	14.55	0.06	11.24	0.19					
PSO J152.0098-09.9888	10	78	19.34	0.02	19.35	0.04	19.3	0.04	19.04	0.01	19.01	0.02	
M100954.53+160203.8	201.9	<15.9	<15.2	-	1.770	NOT	Q						
PSO J152.4773+16.0343	5	83	20.88	0.02	20.74	0.02	20.55	0.02	20.36	0.03	20	0.06	
M101313.10-254654.7	248.8	<16.0	<14.0	-	2.965	SALT	Q						
PSO J101313.09-254654.7	153.3045753	-25.7818673	17.14	0.12	15.98	0.15	11.57	0.25					
M101357.73-245933.6	255	<18.7	<15.6	-	1.814	SALT	Q						
PSO J101357.81-245932.9	153.4908974	-24.9924937	16.67	0.09	15.53	0.10	12.07	-					
M101555.33-082245.7	250.5	<18.6	<16.4	-	1.430	SALT	Q						
PSO J101555.39-082245.5	153.9808222	-8.3793266	17.95	0.27	16.04	0.19	11.74	0.27					
M102159.78-011002.4	500.6	<16.1	<14.0	-	1.493	SALT	Q						
PSO J102159.77-011002.5	155.4990517	-1.1673705	15.72	0.05	15.01	0.09	11.92	0.33					
PSO J155.4990-01.1674	3	44	21.6	0.07	20.97	0.08	20.49	0.04	20.13	0.04	19.54	0.09	
M102441.29-153025.2	226.3	<16.9	<16.7	-	0.792	SALT	Q						

Table 3 *continued*

**Table 3 (continued)**

NVSS-ID	Flux	$B_{maj}$	$B_{min}$	$B_{pa}$	Redshift	Telescope	AGN-type	
WISE-ID	$R_{Aw}$	$Dec_W$	W1	$\delta W1$	W2	$\delta W2$	W3	$\delta W3$
PS1-ID	nStackDets	nDetections	g	$\delta g$	r	$\delta r$	i	$\delta i$
(1)	(2)	(3)	(4)	(5)	(6)	(7)	(8)	
(9)	(10)	(11)	(12)	(13)	(14)	(15)	(16)	(17)
(18)	(19)	(20)	(21)	(22)	(23)	(24)	(25)	(26)
(18)	(19)	(20)	(21)	(22)	(23)	(24)	(25)	(26)
(18)	(19)	(20)	(21)	(22)	(23)	(24)	(25)	(26)
J102444.61-085206.4	PSO J156.1721-15.5073	156.1720931	-15.5073221	15.39	0.04	14.44	0.05	11.25
	463.8	5	58	20.23	0.03	19.88	0.02	19.67
		39.3	<19.1	-29.8	0.455	SUGAR	G	
M102548.78-042933.7	PSO J156.1857-08.8684	156.1856868	-8.8633093	16.36	0.07	15.58	0.12	12.51
	363.5	5	44	-999	-999	21.28	0.04	20.57
		<16.5	<15.9	-	2.292	SALT	Q	
M103051.52-092535.0 <sup>*d</sup>	PSO J156.4532-04.4924	156.4531736	-4.4925229	16.25	0.07	15.47	0.11	12.11
	890.9	5	75	19.57	0.01	19.75	0.03	19.66
		<17.5	<15.5	-	0.413	SALT	G	
M103335.61-121032.1	J103051.50-092523.8	157.7146096	-9.4232841	16.16	0.06	15.32	0.09	12.03
	-	-	-	-	-	-	-	-
M104051.07-144919.4	J103335.62-121032.0	158.3984486	-12.1755657	16.59	0.08	1.328	NOT	G
	PSO J158.3981-12.1757	5	47	21.1	0.03	21.01	0.03	20.97
	269.6	<17.4	<17.0	-	1.526	SALT	Q	
M104314.53-232317.5	J104051.04-144918.9	160.2126978	-14.8219317	17.2	0.13	16.44	0.25	12.61
	PSO J160.2126-14.8219	5	54	21.41	0.05	20.95	0.05	20.72
		<19.7	<14.7	-	2.881	SALT	Q	
M104347.34+164106.9	J104314.52-232319.3	160.8105239	-23.3886967	16.57	0.08	15.95	0.16	12.14
	PSO J160.8104-23.3886	5	54	19.9	0.05	19.72	0.03	19.72
	259.1	<16.4	<15.7	-	0.399	NOT	G	
M105024.43-031808.8	J104347.32+164107.4	160.9471896	16.6854078	15.82	0.05	15.19	0.12	11.74
	PSO J160.9472+16.6854	5	58	22.21	0.05	21.24	0.05	20.54
	243.5	<18.3	<16.3	-	1.813	SUGAR	Q	
M105024.49-031808.4	J105024.49-031808.4	162.6020829	-3.302339	15.25	0.04	14.06	0.04	10.77
	PSO J162.6021-03.3023	5	59	19.07	0.01	18.85	0.01	18.54
	314.5	<16.5	<14.1	-	1.939	SUGAR	Q	
M105955.36-1111818.7	J105955.37-1111818.2	164.9807386	-11.3050771	16.6	0.09	15.71	0.14	12.18

Table 3 continued

**Table 3** (*continued*)

NVSS-ID	Flux	$B_{maj}$	$B_{min}$	$B_{pa}$	Redshift	Telescope	AGN-type	
WISE-ID	$R_{\text{Aw}}$	$Dec_W$	W1	$\delta W1$	$W2$	$\delta W2$	W3	$\delta W3$
PS1-ID	nStackDets	nDetections	g	$\delta g$	r	$\delta r$	i	$\delta i$
(1)	(2)	(3)	(4)	(5)	(6)	(7)	(8)	
(9)	(10)	(11)	(12)	(13)	(14)	(15)	(16)	(17)
(18)	(19)	(20)	(21)	(22)	(23)	(24)	(25)	(26)
(27)	(28)	(29)	(30)					
M111820.61-305459.0	PSO J164.9808-11.3051 233.2	5 <16.9	62 <15.6	20.43 -	0.05 2.352	20.61 SALT	0.06 Q	20.2 0.02
J111820.61-305458.5	169.5859042	-30.9162666	14.8	0.03	13.99	0.04	10.63	0.1
M111917.36-052707.9	-	-	-	-	-	-	-	-
J111917.40-052707.5	1174.4	14.7	<18.6	38.7	2.651	SUGAR	Q	
PSO J169.8226-05.4520	169.8225305	-5.4521081	16.58	0.09	15.94	0.17	11.65	-
M112402.56-150159.1	261.9	5	54	20.47	0.02	20.26	0.03	20.2
PSO J171.0107-15.0330	171.0105586	<17.0	<16.4	-	2.551	SUGAR	Q	
J112402.53-150158.7	171.0105586	-15.0329758	16.65	0.09	15.77	0.15	11.87	0.3
M113750.46-153458.7	241.1	5	57	19.79	0.05	19.61	0.01	19.72
PSO J174.4603-15.5827	174.4604049	-15.5827307	16.46	0.08	15.15	0.09	11.78	0.26
J113750.49-153457.8	174.4604049	-15.5827307	16.46	0.08	15.15	0.09	11.78	0.26
M114226.58-263313.7	294.7	<18.1	<15.9	-	3.237	SALT	Q	
J114226.59-263313.0	175.6107945	-26.5536221	15.6	0.04	14.86	0.07	11.54	0.21
PSO J175.6107-26.5536	10	56	18.9	0.02	18.73	0.01	18.76	0.01
M114825.45+140449.7	322	<17.8	<17.1	-	0.727	NOT	G	
J114825.54+140451.1	177.106422	14.0808677	16.27	0.07	15.61	0.14	11.79	-
PSO J177.1060+14.0803	3	15	-999	-999	21.65	0.16	21.68	0.04
M115043.70+131736.1	254.4	<17.5	<16.5	-	1.530	NOT	Q	
J115043.60+131735.3	177.6817055	13.2931528	16.31	0.07	15.24	0.10	12.02	0.36
PSO J177.6817+13.2931	5	71	19.76	0.04	19.77	0.04	19.51	0.04
M115222.04-270126.3	238.2	<17.7	<15.4	-	2.703	SALT	Q	
J115222.02-270126.1	178.0917554	-27.0239355	16.93	0.1	16.16	0.18	12.4	-
PSO J178.0919-27.0238	5	37	21.01	0.04	20.97	0.07	20.9	0.05
M115306.72-044254.5	684.8	<19.3	<17.9	-	2.591	SALT	Q	
J115306.66-044255.8	178.2777737	-4.7155199	14.96	0.04	14.04	0.04	10.41	0.08
PSO J178.2777-04.7155	5	76	18.68	0.02	18.33	0.02	18.29	0.01
							17.89	0.01

Table 3 *continued*

**Table 3 (continued)**

NVSS-ID	Flux	$B_{maj}$	$B_{min}$	$B_{pa}$	Redshift	Telescope	AGN-type	
WISE-ID	$R_{Aw}$	$Dec_W$	W1	$\delta W1$	$W2$	$\delta W2$	W3	$\delta W3$
PS1-ID	nStackDets	nDetections	g	$\delta g$	r	$\delta r$	i	$\delta i$
(1)	(2)	(3)	(4)	(5)	(6)	(7)	(8)	
(9)	(10)	(11)	(12)	(13)	(14)	(15)	(16)	(17)
(18)	(19)	(20)	(21)	(22)	(23)	(24)	(25)	(26)
(18)	(19)	(20)	(21)	(22)	(23)	(24)	(25)	(26)
(18)	(19)	(20)	(21)	(22)	(23)	(24)	(25)	(26)
M115450.38-281249.7*c	444.5	<18.3	<17.2	-	0.897	SALT	Q	
	J115450.43-281251.0	178.7101313	-28.2141796	16.47	0.08	15.54	0.11	12.08
	PSO J178.7101-28.2141	5	53	20.48	0.06	20.32	0.03	19.98
M120632.23-071452.6	698.8	<16.9	<15.6	-	2.263	NOT	Q	
	J120632.18-071453.1	181.6341117	-7.2480922	16.03	0.06	15.41	0.13	11.68
	PSO J181.6341-07.2481	5	68	19.69	0.01	19.67	0.03	19.57
M121059.72-162042.7	328.3	<19.2	<17.0	-	1.083	SALT	Q	
	J121059.64-162043.4	182.7485411	-16.345399	16.83	0.11	15.99	0.17	12.43
	PSO J182.7487-16.3454	5	55	21.63	0.04	21.27	0.04	20.68
M121211.89-373826.9	343.4	<18.1	<16.4	-	1.9243	SALT	Q	
	J121211.96-373826.5	-37.6407047	183.0498351	15.89	0.04	15.01	0.06	11.77
	-	-	-	-	-	-	-	-
M121514.42-062803.5	360.4	<18.5	<13.9	-	3.218	SUGAR	Q	
	J121514.39-062803.7	183.8099607	-6.4677219	15.78	0.06	15.01	0.11	11.76
	PSO J183.8100-06.4678	5	50	19.88	0.02	19.74	0.03	19.68
M121836.18-063115.8	409.1	<17.2	<16.6	-	0.658	SUGAR	Q	
	J121836.19-063116.9	184.6508305	-6.5213777	14.35	0.03	13.5	0.04	10.41
	PSO J184.6508-06.5213	5	63	18.84	0.03	18.84	0.02	18.71
M121905.45-180911.2	300.3	<17.5	<15.6	-	0.189	NOT	G	
	J121905.43-180910.9	184.7726392	-18.1530363	14.8	0.03	14.15	0.04	11.26
	PSO J184.7726-18.1531	5	76	20.16	0.02	19.19	0.02	18.73
M122123.49-123724.1	343.7	14.5	<15.7	85.1	1.882	NOT	Q	
	J122123.57-123723.0	185.3482462	-12.6230677	15.67	0.05	14.79	0.07	11.77
	PSO J185.3482-12.6230	5	59	19.77	0.02	19.47	0.04	19.01
M123150.30-123637.5	276	<16.3	<15.6	-	2.106	SUGAR	Q	
	J123150.26-123636.8	187.9594437	-12.6102438	15	0.04	13.86	0.04	10.42
	PSO J187.9594-12.6103	5	66	19.07	0.02	18.83	0.01	18.58
M123410.08-332638.5	297.9	<19.9	<16.1	-	2.820	SALT	Q	

GUPTA ET AL.

Table 3 continued

**Table 3** (*continued*)

NVSS-ID	Flux	$B_{maj}$	$B_{min}$	$B_{pa}$	Redshift	Telescope	AGN-type	
WISE-ID	$R_{Aw}$	$Dec_W$	W1	$\delta W1$	W2	$\delta W2$	W3	$\delta W3$
PS1-ID	nStackDets	nDetections	g	$\delta g$	r	$\delta r$	i	$\delta i$
(1)	(2)	(3)	(4)	(5)	(6)	(7)	(8)	
(9)	(10)	(11)	(12)	(13)	(14)	(15)	(16)	(17)
(18)	(19)	(20)	(21)	(22)	(23)	(24)	(25)	(26)
							(27)	(28)
							(29)	(30)
	J123409.97-332638.7	188.5415468	-33.4441047	17.59	0.15	16.75	0.29	12.83
	-	-	-	-	-	-	-	-
M124448.99-044610.2	384.9	<16.8	<13.9	-	3.104	SALT	Q	
	J124449.01-044608.8	191.2042373	-4.7691286	16.25	0.07	15.58	0.12	11.92
	PSO J191.2043-04.7692	5	55	20.84	0.02	20.58	0.02	20.46
M125215.28-310351.2	331.6	<17.9	<16.0	-	1.943	SALT	Q	
	J125215.17-310351.2	193.0632173	-31.0642344	16.47	0.07	15.44	0.09	12.14
	-	-	-	-	-	-	-	-
M125442.98-383356.4	219.2	<18.8	<17.6	-	2.776	SALT	Q	
	J125443.00-383357.3	193.6791669	-38.5659343	17.07	0.1	16.07	0.15	12.52
	-	-	-	-	-	-	-	-
M125611.49-214411.7	260.7	<15.2	<15.2	-	2.178	SALT	Q	
	J125611.41-214410.9	194.0475791	-21.7363772	14.55	0.03	13.77	0.04	10.8
	PSO J194.0476-21.7363	5	73	18.8	0.01	18.32	0.01	17.96
M130457.29-015457.7	325.8	<17.0	<15.6	-	2.100	SALT	Q	
	J130457.38-015458.6	196.2391148	-1.9162803	16.68	0.1	15.76	0.17	12.49
	PSO J196.2389-01.9163	5	46	20.6	0.02	20.67	0.02	20.54
M130958.32+073217.5	205	<16.8	<15.2	-	0.487	SALT	G	
	J130958.33+073217.3	197.4930738	7.5381498	16.2	0.06	15.21	0.09	11.38
	PSO J197.4931+07.5382	5	16	-999	-999	21.63	0.15	21.41
M131139.29-221641.2 <sup>d</sup>	4093	<17.7	<16.6	-	0.885	SALT	Q	
	J131139.34-221642.1	197.913957	-22.2783632	15.63	0.04	14.97	0.07	11.94
	PSO J197.9139-22.2782	5	39	21.86	0.17	21.56	0.09	20.73
M131207.86-202652.4 <sup>f</sup>	778.1	<19.6	<16.5	-	0.977	SALT	G	
	J131207.85-202652.8	198.032746	-20.448026	16.51	0.08	15.76	0.13	12.64
	PSO J198.0328-20.4480	3	4	-999	-999	-999	21.58	0.19
M131301.41-272258.6	239.3	14.9	<16.3	41.8	1.567	SALT	Q	
	J131301.42-272258.7	198.2559293	-27.3829913	15.54	0.05	14.47	0.05	11.16
								0.13

Table 3 *continued*

Table 3 (continued)

NVSS-ID	Flux	$B_{maj}$	$B_{min}$	$B_{pa}$	Redshift	Telescope	AGN-type	
WISE-ID	$R_{Aw}$	$Dec_W$	W1	$\delta W1$	$W2$	$\delta W2$	W3	$\delta W3$
PS1-ID	nStackDets	nDetections	g	$\delta g$	r	$\delta r$	i	$\delta i$
(1)	(2)	(3)	(4)	(5)	(6)	(7)	(8)	
(9)	(10)	(11)	(12)	(13)	(14)	(15)	(16)	(17)
(18)	(19)	(20)	(21)	(22)	(23)	(24)	(25)	(26)
(27)	(28)	(29)	(30)					
M131517.56-274504.0	PSO J198.2559-27.3830	5	38	21.45	0.05	21.03	0.12	20.77
	468.4	40.1	<18.0	17	1.912	SALT	G	0.08
	J131517.61-274505.1	198.823416	-27.7514337	16.86	0.09	15.96	0.15	12.12
	-	-	<16.3	-	-	SALT	Q	0.28
M131736.55-134532.8	244.5	<19.3	-13.7590663	15.64	0.04	14.47	0.05	11.1
	J131736.56-134532.6	199.4023338	5	20.55	0.06	20.22	0.02	20.21
	PSO J199.4022-13.7591	20.1	<17.8	51.3	0.632	NOT	Q	0.05
M131856.01-144155.0	J131856.07-144154.4	199.7336621	-14.6984528	15.14	0.03	14.08	0.04	10.67
	PSO J199.7336-14.6985	5	68	19.73	0.07	19.63	0.02	19.28
M132333.24-223934.5	J132333.24-223934.0	200.8885365	-22.6594475	16.18	0.06	15.2	0.08	11.91
	PSO J200.8885-22.6595	5	63	20.73	0.06	20.24	0.05	20.01
M132657.20-280831.4	404.5	<18.9	<17.2	-	2.238	SALT	Q	0.04
	J132657.18-280832.6	201.738268	-28.1424123	16.35	0.06	15.53	0.11	12.45
	PSO J201.7379-28.1420	5	51	20.54	0.03	20.67	0.14	20.11
M133520.56-391144.6	306.2	<17.1	<15.5	-	2.055	SALT	Q	0.06
	J133520.57-391146.0	203.835731	-39.1961354	15.98	0.04	15.14	0.07	11.85
	-	-	-	-	-	SUGAR	Q	0.21
M134309.26-083457.5	241.5	<19.3	<16.5	-	1.076	SUGAR	Q	-
	J134309.30-083456.6	205.7887762	-8.5824088	15.93	0.05	15.09	0.08	11.88
	PSO J205.7887-08.5825	5	64	20.07	0.03	19.73	0.04	19.44
M135131.98-101932.9	726.1	<18.9	<17.4	-	2.999	SUGAR	Q	0.24
	J135131.98-101932.1	207.8832846	-10.3256104	15.02	0.03	14.12	0.04	10.74
	PSO J207.8833-10.3256	5	89	18.15	0.01	17.93	0.01	17.86
M135547.99-370955.5*c	248.8	<18.0	<17.0	-	1.323	SALT	Q	0.09
	J135547.99-370956.3	208.9499945	-37.1656536	16.4	0.06	15.4	-	11.88
	-	-	-	-	-	-	-	-

GUPTA ET AL.

Table 3 (*continued*)

NVSS-ID	Flux	$B_{maj}$	$B_{min}$	$B_{pa}$	Redshift	Telescope	AGN-type	
WISE-ID	$R_{Aw}$	$Dec_W$	W1	$\delta W1$	$W2$	$\delta W2$	W3	$\delta W3$
PS1-ID	nStackDets	nDetections	g	$\delta g$	r	$\delta r$	i	$\delta i$
(1)	(2)	(3)	(4)	(5)	(6)	(7)	(8)	
(9)	(10)	(11)	(12)	(13)	(14)	(15)	(16)	(17)
(18)	(19)	(20)	(21)	(22)	(23)	(24)	(25)	(26)
(18)	(19)	(20)	(21)	(22)	(23)	(24)	(25)	(26)
(18)	(19)	(20)	(21)	(22)	(23)	(24)	(25)	(26)
M141327.20-342235.1	274.7	<17.1	<14.9	-	2.812	SALT	Q	
	J141327.16-342235.6	213.3631998	-34.3765388	15.42	0.04	14.35	0.05	10.81
		-	-	-	-	-	-	0.09
M141338.15-071625.3	232.7	17.2	<16.7	-88.6	0.416	SALT	G	
	J141338.23-071624.5	213.4093225	-7.2734885	17.16	0.12	16.29	0.21	12.37
	PSO J213.4090-07.2735	5	32	22.15	0.01	21.48	0.11	20.68
M142155.55-310427.9	732.6	<18.0	<17.7	-	1.568	SALT	Q	
	J142155.57-310425.1	215.48157	-31.07366	16.96	0.12	16.06	0.20	12.3
		-	-	-	-	-	-	-
M142213.87-091018.4	398.7	<18.8	<16.8	-	0.876	SALT	G	
	J142213.88-091018.2	215.5578602	-9.1717354	15.82	0.05	15.14	0.09	11.09
	PSO J215.5579-09.1717	4	11	-999	-999	-999	21.38	0.13
M143709.04-294718.5	273.8	<18.6	<17.3	-	2.331	SALT	Q	
	J143708.95-294718.7	219.2873327	-29.7885418	16.23	0.08	15.36	0.14	12.17
	PSO J219.2874-29.7885	5	21	19.6	0.05	19.54	0.03	19.37
M144032.09+053120.7	214.9	<18.6	<18.1	-	0.754	SALT	Q	
	J144032.02+053122.4	220.1334503	5.5229058	15.39	0.04	14.52	0.05	11.44
	PSO J220.1335+05.5229	5	69	20.33	0.04	20.31	0.04	20.17
M144851.10-112215.6	455.5	<13.9	<13.9	-	2.630	SALT	Q	
	J144851.15-112215.6	222.2131474	-11.3710267	14.95	0.04	14.18	0.05	10.87
	PSO J222.2132-11.3710	5	72	18.21	0.02	18.07	0.02	18.03
M145212.06-255639.8 <sup>a,b</sup>	229.9	<16.2	<15.8	-	1.693	SALT	Q	
	J145212.09-255639.5	223.050385	-25.9443099	15.88	0.05	14.75	0.07	11.3
	PSO J223.0503-25.9444	5	64	20.11	0.01	19.82	0.01	19.45
M145342.95-132738.2	254.5	<19.6	<17.3	-	2.370	SALT	Q	
	J145342.94-132735.8	223.4289562	-13.4599571	14.6	0.03	13.51	0.04	10.13
	PSO J223.4290-13.4600	5	59	18.4	0.01	17.98	0.02	17.86
M145502.84-170014.2 <sup>a</sup>	294.7	<17.1	<15.8	-	2.291	SALT	Q	

SALT-NOT SURVEY OF MIR-SELECTED AGN

Table 3 *continued*

**Table 3** (*continued*)

NVSS-ID	Flux	$B_{maj}$	$B_{min}$	$B_{pa}$	Redshift	Telescope	AGN-type	
WISE-ID	$R_{Aw}$	$Dec_W$	W1	$\delta W1$	$W2$	$\delta W2$	W3	$\delta W3$
PS1-ID	nStackDets	nDetections	g	$\delta g$	r	$\delta r$	i	$\delta i$
(1)	(2)	(3)	(4)	(5)	(6)	(7)	(8)	
(9)	(10)	(11)	(12)	(13)	(14)	(15)	(16)	(17)
(18)	(19)	(20)	(21)	(22)	(23)	(24)	(25)	(26)
							(27)	(28)
							(29)	(30)
M145536.16-095709.2	PSO J223.7617-17.0039	5	<18.8	<17.1	33	21.21	0.08	15.7
	J145536.14-095707.4	223.9005923	-9.9520677	17.3	-	1.992	21.04	0.06
	-	-	-	-	-	SALT	0.06	20.82
M145625.83+045645.2	J145625.81+045644.5	287.9	<18.7	<17.8	-	15.87	0.15	G
	PSO J224.1075+04.9458	224.1075561	4.9457114	16.21	0.06	-	11.31	0.12
M145908.92-164542.3	J145908.90-164541.9	378.9	<16.9	<15.4	-	2.134	SUGAR	-
	PSO J224.7871-16.7621	10	59	20.3	0.03	15.5	0.10	-
M150425.30+081858.6	J150425.26+081858.7	210.8	<14.4	<14.0	-	2.006	SALT	0.01
	PSO J226.1054+08.3163	226.1052909	8.3163078	16.4	0.09	20.01	12.62	0.42
M150712.88-313729.6	J150712.97-313731.8	226.8040709	-31.6255152	15.88	0.06	21.25	19.73	0.01
	-	-	-	-	-	SALT	0.01	19.38
M151129.01-072255.3	J151128.97-072256.1	326.3	<18.6	<15.2	-	15.4	0.11	0.02
	PSO J227.8707-07.3823	5	227.8707292	-7.3822515	15.62	0.04	20.8	0.04
M151204.81-132833.0 <sup>a,b</sup>	J151204.73-132833.0	295	<17.1	<16.1	-	1.737	SALT	-
	PSO J228.0198-13.4758	228.0197468	-13.4758439	16.35	0.08	14.98	Q	-
M151304.72-252439.7	J151304.76-252439.7	217.6	26.4	<16.0	-	18.79	0.01	-
	-	-	-	-	-	SALT	0.01	-
M151944.77-115144.6 <sup>a</sup>	J151944.76-115144.8	441	<15.8	<15.2	-	2.014	SALT	0.01
		229.9365081	-11.862463	16.54	0.09	15.36	Q	18.46
		-	-	-	-	0.12	11.99	0.06

GUPTA ET AL.

Table 3 *continued*

Table 3 (continued)

NVSS-ID	Flux	$B_{maj}$	$B_{min}$	$B_{pa}$	Redshift	Telescope	AGN-type	
WISE-ID	$R_{Aw}$	$Dec_W$	W1	$\delta W1$	W2	$\delta W2$	W3	$\delta W3$
PS1-ID	nStackDets	nDetections	g	$\delta g$	r	$\delta r$	i	$\delta i$
(1)	(2)	(3)	(4)	(5)	(6)	(7)	(8)	
(9)	(10)	(11)	(12)	(13)	(14)	(15)	(16)	(17)
(18)	(19)	(20)	(21)	(22)	(23)	(24)	(25)	(26)
							(27)	(28)
							(29)	(30)
M154015.23-145341.5	PSO J229.9366-11.8624	5	61	20.99	0.05	20.93	0.12	20.29
	203.3	<17.9	<16.4	-	2.098	SALT	Q	20.1
	J154015.24-145341.9	235.0635366	-14.8949753	16.41	0.09	15.48	0.14	11.58
	PSO J235.0634-14.8952	5	62	20.68	0.02	20.42	0.03	19.98
M154414.23-231200.8*c	296.4	<16.3	<16.0	-	1.026	SALT	Q	0.02
	J154414.17-231200.7	236.0590426	-23.2002035	16.52	0.11	15.85	0.21	11.62
	PSO J236.0591-23.2004	10	50	21.12	0.08	20.53	0.07	20.31
M155212.77-073246.5*c	222.3	<17.3	<16.6	-	1.015	SALT	Q	0.04
	J155212.76-073246.5	238.0532006	-7.54632598	17.16	0.14	16.52	-	12.11
	PSO J238.0532-07.5462	5	59	20.48	0.02	20.25	0.03	20.35
M155709.44+055216.1*d	231.7	<18.6	<16.8	-	0.668	SALT	G	0.01
	J155709.42+055215.4	239.2892897	5.870947	16.34	0.07	15.51	0.10	11.27
	PSO J239.2893+05.8709	5	51	-999	-999	21.53	0.07	20.99
M155825.35-215511.5	206.9	<19.5	<15.6	-	2.760	SALT	Q	0.04
	J155825.36-215511.1	239.6056955	-21.9197627	14.6	0.03	13.52	0.04	10.17
	PSO J239.6057-21.9198	5	53	20.4	0.01	19.95	0.03	19.43
M160903.37-145457.6*d	213.6	<17.2	<14.0	-	0.931	SALT	G	0.02
	J160903.34-145458.2	242.2639473	-14.9161735	15.98	0.06	15.19	0.10	12.13
	PSO J242.2641-14.9162	5	4	-999	-999	-999	-999	21.65
M161454.47-154550.7	473.8	<16.9	<14.7	-	0.920	SALT	Q	0.11
	J161454.39-154549.1	243.7266435	-15.7636422	15.19	0.04	14.27	0.05	11.17
	PSO J243.7267-15.7637	5	75	20.6	0.02	19.74	0.12	19.6
	340.3	<16.5	<15.6	-	2.891	SALT	Q	0.04
M161907.44-093953.1	J161907.44-093952.5	244.7810354	-9.6646096	15.87	0.05	14.8	0.07	11.29
	PSO J244.7810-09.6647	5	62	19.97	0.02	19.5	0.02	19.17
M162047.94+003653.2	317.8	<16.7	<15.7	-	2.438	SALT	Q	0.01
	J162047.96+003653.1	245.1998398	0.6147621	14.77	0.03	14.05	0.04	11.13
	PSO J245.1998+00.6148	10	71	18.92	0.01	18.7	0.01	18.61

Table 3 continued

**Table 3** (*continued*)

NVSS-ID	Flux	$B_{maj}$	$B_{min}$	$B_{pa}$	Redshift	Telescope	AGN-type	
WISE-ID	$R_{Aw}$	$Dec_W$	W1	$\delta W1$	$W2$	$\delta W2$	$W3$	$\delta W3$
PS1-ID	nStackDets	nDetections	g	$\delta g$	r	$\delta r$	i	$\delta i$
(1)	(2)	(3)	(4)	(5)	(6)	(7)	(8)	
(9)	(10)	(11)	(12)	(13)	(14)	(15)	(16)	(17)
(18)	(19)	(20)	(21)	(22)	(23)	(24)	(25)	(26)
(18)	(19)	(20)	(21)	(22)	(23)	(24)	(25)	(26)
(18)	(19)	(20)	(21)	(22)	(23)	(24)	(25)	(26)
M164950.51+062653.3	389.2	<18.0	<16.8	-	2.144	SUGAR	Q	
	J164950.54+062652.8	252.4606031	6.4480267	14.75	0.04	13.64	0.03	10.4
	PSO J252.4604+06.4482	5	77	18.87	0.02	18.73	0.02	18.54
M165038.03-124854.5	275.5	<18.5	<15.5	-	2.527	SUGAR	Q	
	J165038.01-124853.2	252.6584023	-12.8147998	16.23	0.07	15.07	0.09	11.27
	PSO J252.6585-12.8149	5	68	21.06	0.05	20.58	0.04	20.37
M165357.67-010214.2	317.4	<17.9	<15.5	-	1.088	SUGAR	Q	
	J165357.67-010213.4	253.4903148	-1.0370705	15.71	0.05	14.8	0.06	11.67
	PSO J253.4904-01.0371	5	73	21.04	0.03	20.48	0.04	20.09
M165435.38+001719.5	255.3	<17.9	<15.3	-	2.363	SALT	Q	
	J165435.38+001719.2	253.6474532	0.2886674	16.92	0.11	15.92	0.16	12.49
	PSO J253.6474+00.2888	5	71	20.08	0.04	20.01	0.03	19.84
M170333.50+064539.7	236.6	<17.9	<16.7	-	0.399	SALT	G	
	J170333.53+064539.3	255.8897404	6.7609306	15.24	0.04	14.07	0.04	10.66
	PSO J255.8898+06.7609	5	55	22.02	0.21	21.18	0.03	20.35
M171627.09-061356.5	229.9	17.6	<20.0	-48.4	1.840	NOT	Q	
	J171627.07-061356.3	259.1128304	-6.2323088	14.03	0.03	12.82	0.03	9.49
	PSO J259.1128-06.2323	5	67	19.95	0.01	19.07	0.03	18.41
M172105.79+162649.1	507.9	<17.8	<16.5	-	1.814	NOT	Q	
	J172105.77+162649.4	260.2740504	16.4470577	16.11	0.05	15.31	0.08	11.8
	PSO J260.2741+16.4470	5	85	19.95	0.03	19.97	0.01	19.58
M172214.09+044316.8	765.5	19.9	<16.8	64.3	0.603	SALT	G	
	J172214.07+044317.0	260.5586294	4.7213966	15.01	0.04	14.29	0.05	11.1
	PSO J260.5586+04.7214	4	35	-999	-999	21.62	0.09	20.6
M172507.45+062242.1	213.4	<18.5	<16.2	-	1.355	SUGAR	Q	
	J172507.43+062240.9	261.280972	6.3780555	15.4	0.04	14.49	0.05	11.36
	PSO J261.2812+06.3781	10	73	19.45	0.02	19.05	0.02	18.8
M190923.40-392311.7	204.9	<18.9	<16.2	-	2.513	SALT	Q	

Table 3 *continued*

**Table 3** (*continued*)

NVSS-ID	Flux	$B_{maj}$	$B_{min}$	$B_{pa}$	Redshift	Telescope	AGN-type	
WISE-ID	$R_{Aw}$	$Dec_W$	W1	$\delta W1$	W2	$\delta W2$	W3	$\delta W3$
PS1-ID	nStackDets	nDetections	g	$\delta g$	r	$\delta r$	i	$\delta i$
(1)	(2)	(3)	(4)	(5)	(6)	(7)	(8)	(9)
(10)	(11)	(12)	(13)	(14)	(15)	(16)	(17)	(18)
(19)	(20)	(21)	(22)	(23)	(24)	(25)	(26)	(27)
(28)	(29)	(30)						
J190923.31-392312.1	287.3471522	-39.3867043	16.62	0.1	15.54	0.14	11.57	0.25
M192956.85-351619.6	276.4	<19.0	<19.0	-	-	-	-	-
J192956.83-351619.7	292.4867973	-35.2721648	14.25	0.03	13.52	0.04	10.24	0.09
M193147.88-360659.1	779.6	<17.6	<16.9	-	-	-	-	-
J193147.94-360658.1	292.9497658	-36.1161433	14.73	0.04	13.85	0.04	9.84	0.05
M194110.28-300720.9	315	<19.5	<15.1	-	-	-	-	-
J194110.25-300720.5	295.2927432	-30.1223853	13.65	0.03	12.88	0.03	9.94	0.06
M195243.90-193623.7	596.3	<19.3	<18.2	-	-	-	-	-
J195243.87-193622.1	298.1828116	-19.6061565	16.06	0.08	14.85	0.10	11.24	0.18
PSO J298.1828-19.6064	10	67	20.65	0.03	20.48	0.02	20.16	0.02
M195629.92-054246.9	351.3	<18.0	<16.8	-	1.103	SALT	Q	0
J195630.01-054247.4	299.1250677	-5.7131809	14.79	0.04	13.84	0.04	10.52	0.09
PSO J299.1250-05.7130	5	66	18.91	0.01	18.47	0.01	18.31	0.01
M200008.58-192138.3 <sup>c</sup>	896.7	<16.3	<16.1	-	1.187	SALT	Q	
J200008.56-192138.3	300.0356945	-19.3606496	16.17	0.07	15.04	0.10	11.59	-
PSO J300.0357-19.3604	5	80	20.2	0.03	19.74	0.03	19.54	0.02
M200209.37-145531.8	620.3	<17.0	<15.6	-	2.192	SALT	Q	
PSO J300.5390-14.9255	300.539052	-14.9256698	16.41	0.08	15.46	0.12	12.34	0.45
M201708.96-293354.7	327.2	<17.1	<15.8	-	2.617	SALT	Q	
J201708.95-293355.2	304.2873084	-29.5653586	15.91	0.06	14.89	0.08	11.42	0.21
PSO J304.2873-29.5653	5	67	19.79	0.02	19.37	0.01	19.51	0.02
M201952.74-394808.3 <sup>c</sup>	234.6	<19.2	<17.2	-	1.194	SALT	Q	
J201952.68-394809.1	304.9695021	-39.8025426	16.17	0.06	15.32	0.10	12.15	0.32

*Table 3 continued*

**Table 3** (*continued*)

NVSS-ID	Flux	$B_{maj}$	$B_{min}$	$B_{pa}$	Redshift	Telescope	AGN-type	
WISE-ID	$R_{Aw}$	$Dec_W$	W1	$\delta W1$	W2	$\delta W2$	W3	$\delta W3$
PS1-ID	nStackDets	nDetections	g	$\delta g$	r	$\delta r$	i	$\delta i$
(1)								
(2)		(3)	(4)	(5)	(6)	(7)	(8)	
(9)		(10)	(11)	(12)	(13)	(14)	(15)	(17)
(18)		(19)	(20)	(21)	(22)	(23)	(24)	(26)
(30)								
M203425.65-052332.2	-	-	-	-	-	-	-	-
J203425.62-052331.8	419.7	14.9	<18.0	58.5	2.070	NOT	Q	
PSO J308.6067-05.3922	308.6067642	-5.3921681	15.58	0.05	14.61	0.06	11.18	0.16
M204608.17-391840.7	250	<17.0	66	18.67	0.01	18.64	0.02	18.41
J204607.98-391841.9	311.5332541	-39.3116438	16.63	0.08	2.619	SALT	Q	
M204737.66-184141.6	-	-	-	-	-	-	-	-
J204737.67-184141.2	241.7	<17.2	<16.1	-	2.994	SALT	Q	
PSO J311.9069-18.6948	311.9069909	-18.6947958	15.26	0.04	14.37	0.06	10.73	0.11
M205245.03-223410.6	330.9	<18.1	<15.9	-	2.072	SALT	Q	
J205244.97-223410.3	313.1873933	-22.569539	15.11	0.04	14.08	0.04	10.82	0.12
PSO J313.1874-22.5695	5	96	18.36	0.01	18.17	0.01	18.07	0.01
M205456.08-093240.8	313.6	<18.1	<15.5	-	1.373	SUGAR	Q	
J205456.07-093241.0	313.733661	-9.5447295	16.42	0.08	15.44	0.13	11.74	0.38
PSO J313.7336-09.5447	5	61	20.76	0.08	20.06	0.04	20.1	0.03
M205548.51-190545.6**c	227.3	<18.6	<16.0	-	0.809	SALT	Q	
J205548.49-190546.1	313.9520661	-19.096164	16.41	0.09	15.38	0.12	12.2	0.46
PSO J313.9521-19.0961	10	73	21.15	0.07	21.1	0.09	20.63	0.02
M205842.96-173649.9	332.5	<17.6	<17.0	-	0.754	SALT	G	
J205842.93-173650.6	314.6789027	-17.614082	15.63	0.05	14.8	0.08	11.6	-
PSO J314.6789-17.6141	5	46	22.43	0.19	21.69	0.06	21.07	0.03
M205959.61-144043.1	1018.1	<19.3	<16.7	-	0.689	SUGAR	G	
J205959.57-144042.0	314.9982203	-14.6783558	14.63	0.03	13.63	0.04	10.45	0.11
PSO J314.9982-14.6783	10	68	21.28	0.05	20.54	0.05	20.05	0.02
M210143.29-174759.2	959.5	<16.5	<16.2	-	2.803	SALT	Q	
J210143.32-174759.2	315.4305276	-17.7997963	17.31	0.15	16.48	0.29	12.35	0.48
PSO J315.4303-17.7997	5	68	21.2	0.03	20.84	0.05	20.98	0.02
								-999

GUPTA ET AL.

## SALT-NOT SURVEY OF MIR-SELECTED AGN

Table 3 (*continued*)

NVSS-ID	Flux	$B_{maj}$	$B_{min}$	$B_{pa}$	Redshift	Telescope	AGN-type	
WISE-ID	$R_{Aw}$	$Dec_W$	W1	$\delta W1$	W2	$\delta W2$	W3	$\delta W3$
PS1-ID	nStackDets	nDetections	g	$\delta g$	r	$\delta r$	i	$\delta i$
(1)	(2)	(3)	(4)	(5)	(6)	(7)	(8)	
(9)	(10)	(11)	(12)	(13)	(14)	(15)	(16)	(17)
(18)	(19)	(20)	(21)	(22)	(23)	(24)	(25)	(26)
(27)	(28)	(29)	(30)					
M211311.86-393933.7	554.2	<18.4	<16.0	-	0.843	SALT	Q	
J211311.86-393934.6	318.2994201	-39.6596198	15.12	0.04	14.13	0.04	10.89	0.11
M211949.40-343938.6	287.2	<17.7	<17.1	-	-	-	-	-
J211949.37-343939.1	319.9557426	-34.6608848	15.43	0.04	0.452	SALT	G	
M212042.48+132724.2	401.5	<18.1	<16.5	-	1.110	NOT	Q	
J212042.48+132727.1	320.177014	13.4575549	14.68	0.03	13.91	0.04	10.56	0.07
PSO J320.1771+13.4580	5	66	21.16	0.02	20.11	0.01	19.52	0.02
M212758.87-385856.3	355.8	<16.9	<15.8	-	2.663	SALT	Q	
J212758.91-385855.9	321.9954748	-38.9821988	16.81	0.1	16.01	0.17	11.58	0.21
M212821.83-150453.2	245.5	<16.2	<14.7	-	-	-	-	-
J212821.89-150453.1	322.0912098	-15.0814335	15.84	0.06	14.97	0.08	11.91	0.39
PSO J322.0912-15.0813	5	86	19.32	0.01	19.16	0.02	19.19	0.01
M213135.55-270159.0 <sup>b</sup>	205.9	<18.5	<15.9	-	1.921	SALT	Q	
J213135.55-270159.1	322.8981403	-27.0331064	15.85	0.05	14.71	0.07	11.4	0.2
PSO J322.8981-27.0331	5	86	19.02	0.01	18.93	0.02	18.78	0.01
M213937.03+171826.9	219.4	20.3	<17.5	-63	1.700	NOT	Q	
J213937.14+171825.9	324.90478	17.3072104	15.43	0.04	14.23	0.05	10.88	0.09
PSO J324.9048+17.3072	5	79	19.16	0.01	18.9	0.02	18.58	0.01
M214120.76-351516.9	371.3	<18.7	<16.0	-	2.599	SALT	Q	
J214120.77-351517.1	325.33655774	-35.2547519	17.21	0.12	16.09	0.17	12.74	0.5
M215445.08-382632.5	759.8	<18.5	<15.0	-	-	-	-	-
J215445.04-382632.5	328.6876684	-38.4423862	13.5	0.03	12.64	0.03	9.46	0.04
M215800.88+092546.4	437.7	<15.5	<14.4	-	0.447	SUGAR	G	

Table 3 *continued*

**Table 3** (*continued*)

NVSS-ID	Flux	$B_{maj}$	$B_{min}$	$B_{pa}$	Redshift	Telescope	AGN-type	
WISE-ID	$R_{Aw}$	$Dec_W$	W1	$\delta W1$	W2	$\delta W2$	W3	$\delta W3$
PS1-ID	nStackDets	nDetections	g	$\delta g$	r	$\delta r$	i	$\delta i$
(1)	(2)	(3)	(4)	(5)	(6)	(7)	(8)	(9)
(10)	(11)	(12)	(13)	(14)	(15)	(16)	(17)	(18)
(19)	(20)	(21)	(22)	(23)	(24)	(25)	(26)	(27)
(28)	(29)	(30)						
J215800.86+092546.0	329.5036223	9.4294464	15.19	0.04	14.33	0.05	9.91	0.06
PSO J329.5037+09.4294	5	68	21.27	0.05	20.16	0.03	19.77	0.03
M220127.50+031215.6	300.5	<18.4	<15.7	-	2.181	SUGAR	Q	
J220127.47+031215.6	330.3644887	3.2043567	16.31	0.07	15.61	0.12	11.78	
PSO J330.3646+03.2042	8	48	20.46	0.2	21.04	0.08	20.95	0.05
M221843.50-122912.9 <sup>c</sup>	230.4	<16.7	<15.6	-	1.156	SALT	Q	
J221843.45-122913.6	334.081072	-12.4871191	16.99	0.13	15.99	0.20	11.74	
PSO J334.6810-12.4870	5	76	20.99	0.04	20.59	0.04	20.17	0.03
M222004.97+130712.1	812	21.8	<17.2	-5.7	0.760	NOT	Q	
J222005.10+130710.9	335.0212696	13.1197105	14.94	0.04	14.19	0.05	11.11	0.17
PSO J335.0212+13.1197	5	74	20.59	0.02	20.31	0.03	20.11	0.01
M222332.81-310117.3	231.7	<16.1	<15.4	-	3.206	SALT	Q	
J222332.79-310117.7	335.8866347	-31.0216	16.15	0.05	15.18	0.08	11.91	0.31
M222420.03+130450.2	-	-	-	-	-	-	-	-
J222420.06+130450.7	294.5	<17.3	<16.8	-	0.685	NOT	Q	
PSO J336.0835+13.0807	336.0836105	13.0807776	16.15	0.06	15.13	0.10	11.67	
M223050.19+034836.8	242.8	<17.8	<16.7	-	1.330	SUGAR	Q	
J223050.19+034835.8	337.7091503	3.8099591	16.53	0.08	15.92	0.15	12.15	-
PSO J337.7092+03.8101	5	60	21.1	0.04	20.64	0.04	20.23	0.05
M223816.27-124036.4	213.6	<18.4	<16.2	-	2.623	SALT	Q	
J223816.28-124036.6	339.5678681	-12.6768403	16.31	0.07	15.47	0.12	11.83	0.32
PSO J339.5676-12.6768	5	86	21.21	0.06	20.56	0.02	20.53	0.03
M223826.48-134422.6	241.2	14.7	<16.6	-50.1	0.257	NOT	G	
J223826.55-134421.5	339.6106451	-13.7393129	14.78	0.03	13.97	0.04	10.78	0.12
PSO J339.6104-13.7396	5	73	20.94	0.06	19.81	0.03	19.46	0.02
M223831.50-173119.1	348.8	<19.3	<16.0	-	1.831	SALT	Q	
J223831.46-173117.7	339.6311027	-17.5215972	15.77	0.06	14.9	0.08	11.66	0.25

GUPTA ET AL.

Table 3 *continued*

Table 3 (continued)

NVSS-ID	Flux	$B_{maj}$	$B_{min}$	$B_{pa}$	Redshift	Telescope	AGN-type	
WISE-ID	$R_{Aw}$	$Dec_W$	W1	$\delta W1$	W2	$\delta W2$	W3	$\delta W3$
PS1-ID	nStackDets	nDetections	g	$\delta g$	r	$\delta r$	i	$\delta i$
(1)	(2)	(3)	(4)	(5)	(6)	(7)	(8)	
(9)	(10)	(11)	(12)	(13)	(14)	(15)	(16)	(17)
(18)	(19)	(20)	(21)	(22)	(23)	(24)	(25)	(26)
(18)	(19)	(20)	(21)	(22)	(23)	(24)	(25)	(26)
(18)	(19)	(20)	(21)	(22)	(23)	(24)	(25)	(26)
(18)	(19)	(20)	(21)	(22)	(23)	(24)	(25)	(26)
(18)	(19)	(20)	(21)	(22)	(23)	(24)	(25)	(26)
M224018.74+022030.0 <sup>c</sup>	PSO J339.6310-17.5215 211	5 <17.0	64 <15.8	18.88 -	0.01 0.694	18.79 SALT	0.01 Q	18.57 0.21
	J224018.90+022028.5	340.0787841 5	2.3412684 75	15.63 19.7	0.05 0.05	14.98 19.41	0.09 0.02	11.16 19.34
	PSO J340.0781+02.3415	5 <16.7	<15.3 -24.710643	-24.710643 15.54	0.05 0.05	2.242 14.44	SALT NOT	0.02 0.01
M224111.48-244239.0	J224111.50-244238.3	340.2979416 5	89 <16.5	18.8 -	0.04 0.760	18.47 14.48	0.01 0.05	19.17 18.58
	PSO J340.2980-24.7107	5 <17.9	<16.5 18.2457301	18.2457301 15.94	0.05 0.05	NOT G	G	0.01 0.02
M224354.81+181445.9	J224354.81+181444.6	340.9784026 5	53 53	21.07 21.07	0.02 0.02	20.29 20.29	0.01 0.01	18.41 10.34
	PSO J340.9785+18.2457	5 <16.9	<16.7 12.1977348	12.1977348 17.27	0.14 0.14	2.185 16.66	NOT Q	0.08 0.08
M224705.52+121151.4	J224705.55+121151.8	341.7731632 5	35 35	21.43 21.43	0.05 0.05	21.22 21.22	- 0.06	20.04 21.03
	PSO J341.7731+12.1976	5 <16.3	<15.8 -26.5832163	-26.5832163 16.23	0.07 0.07	2.174 15.26	SALT NOT	0.09 0.09
M224950.57-263459.6	J224950.57-263459.5	342.4607113 5	61 14	20.23 <16.9	0.02 -47.5	20.04 0.624	0.05 0.05	20.7 12.06
	PSO J342.4607-26.5832	5 515.3	14 14	<16.9 -33.1827883	15.15 0.04	14.46 14.46	Q 0.05	0.07 19.98
M225137.19-331056.9	J225137.20-331056.0	342.9050396 -	- -	- -	- -	- -	- -	19.42 0.03
M225236.48-030551.4	J225236.46-030550.4	343.1519288 5	<16.5 75	<14.8 19.7	- 0.03	1.633 19.66	SALT NOT	0.09 0.08
	PSO J343.1519-03.0973	5 14.9	<16.1 19.6670443	-29.6 15.94	2.160 0.06	Q 15.22	Q 0.09	20.7 12.19
M230036.41+194002.9	J230036.35+194001.3	345.1514973 5	64 <17.3	19.63 <15.3	0.02 1.861	19.58 SUGAR	0.01 Q	19.05 19.31
	PSO J345.1515+19.6671	5 509	67 <17.3	19.5 15.54	0.03 0.05	14.45 19.48	0.02 0.02	19.05 19.31
M230040.87+033710.3	J230040.89+033710.8	345.1703754 5	67 67	19.5 15.54	0.03 0.03	10.89 19.48	0.01 0.02	19.05 19.31
	PSO J345.1704+03.6197	5 -	- -	- -	- -	- -	- -	0.05 0.05

Table 3 (continued)

**Table 3** (*continued*)

NVSS-ID	Flux	$B_{maj}$	$B_{min}$	$B_{pa}$	Redshift	Telescope	AGN-type	
WISE-ID	$R_{Aw}$	$Dec_W$	W1	$\delta W1$	$W2$	$\delta W2$	W3	$\delta W3$
PS1-ID	nStackDets	nDetections	g	$\delta g$	r	$\delta r$	i	$\delta i$
(1)	(2)	(3)	(4)	(5)	(6)	(7)	(8)	
(9)	(10)	(11)	(12)	(13)	(14)	(15)	(16)	(17)
(18)	(19)	(20)	(21)	(22)	(23)	(24)	(25)	(26)
(18)	(19)	(20)	(21)	(22)	(23)	(24)	(25)	(26)
(18)	(19)	(20)	(21)	(22)	(23)	(24)	(25)	(26)
M230805.25-114945.7	256.8	<18.2	<16.3	-	1.940	NOT	Q	
	J230805.22-114945.2	347.0217611	-11.8292281	16.66	0.1	15.9	0.22	12.07
	PSO J347.0218-11.8292	5	58	20.37	0.02	20.29	0.03	20.18
M231002.89+111403.6	248.1	<16.8	<16.3	-	1.550	NOT	Q	
	J231002.90+111404.6	347.5121118	11.2346199	16.55	0.08	15.39	0.11	12.12
	PSO J347.5121+11.2346	5	70	19.69	0.01	19.77	0.03	19.51
M231634.61+042940.2	214	<19.0	<16.6	-	2.180	SUGAR	Q	
	J231634.61+042939.8	349.1442147	4.4943985	15.72	0.05	14.46	0.06	11.15
	PSO J349.1442+04.4944	5	78	19.35	0.01	19.2	0.03	18.89
M233231.61-142318.8	234.1	25.5	16	-46.8	0.524	NOT	Q	
	J233231.76-142320.7	353.132351	-14.3890852	14.79	0.03	14.1	0.05	11.06
	PSO J353.1324-14.3891	10	47	20.97	0.05	20.28	0.04	19.64
M233808.04-121851.4	450.9	14.9	<16.5	6.4	1.185	NOT	Q	
	J233808.06-121850.5	354.5336244	-12.3140449	16.01	0.06	15.04	0.08	11.81
	PSO J354.5336-12.3141	5	57	19.95	0.02	19.45	0.04	19.44
M234159.52-400856.2	460.7	<15.2	<13.9	-	0.562	SALT	Q	
	J234159.50-400854.4	355.4979212	-40.1484663	14.8	0.03	14.02	0.04	10.93
	-	-	-	-	-	SALT	Q	
M234207.38-092346.5	451.2	<19.5	<16.6	-	1.723	SALT	Q	
	J234207.43-092346.4	355.5309878	-9.3962396	15.69	0.05	14.46	0.06	10.99
	PSO J355.5310-09.3962	5	40	21.6	0.07	21.48	0.09	20.7
M234910.12-043803.2	206.1	<16.4	<16.2	-	2.240	SALT	Q	
	J234910.16-043803.2	357.2923581	-4.632274	15.77	0.05	14.99	0.09	11.61
	PSO J357.2924-04.6343	5	72	18.68	0.01	18.76	0.01	18.6
M235722.47-073134.3	235.5	<16.9	<15.9	-	2.764	SALT	Q	
	J235722.56-073134.1	359.3440369	-7.5261639	16.24	0.07	15.62	0.17	12.28
	PSO J359.3438-07.5261	5	79	19.97	0.03	19.58	0.01	19.38

Table 3 *continued*

Table 3 (*continued*)

## SALT-NOT SURVEY OF MIR-SELECTED AGN

NVSS-ID	Flux	$B_{maj}$	$B_{min}$	$B_{pa}$	Redshift	Telescope	AGN-type	
WISE-ID	$R_{Aw}$	$Dec_W$	W1	$\delta W1$	W2	$\delta W2$	W3	$\delta W3$
PS1-ID	nStackDets	nDetections	g	$\delta g$	r	$\delta r$	i	$\delta i$
(1)	(2)	(3)	(4)	(5)	(6)	(7)	(8)	
(9)	(10)	(11)	(12)	(13)	(14)	(15)	(16)	(17)
(18)	(19)	(20)	(21)	(22)	(23)	(24)	(25)	(26)
							(27)	(28)
							(29)	(30)
No emission lines (26)								
M001053.65-215703.9	387.8	<18.9	<16.3	-	-	SALT		
J001053.64-215704.2	2.7235144	-21.9511886	14.8	0.03	13.79	0.04	10.57	0.08
PSO J002.7235-21.9512	5	43	21.07	0.05	20.38	0.06	20.01	0.16
M002232.46+060804.6	339.7	<17.7	<15.5	-	-	NOT	20.11	0.06
J002232.44+060804.2	5	6.6351816	6.1345179	13.23	0.03	12.21	0.02	9.03
PSO J005.6352+06.1345	5	83	18.45	0.04	18.52	0.02	18.54	0.06
M002945.04-174043.6	394.3	<19.5	<16.3	-	-	SALT		
J002945.09-174042.4	7.4378894	-17.6784528	15.65	0.05	14.57	0.06	11.25	0.18
PSO J007.4379-17.6786	5	58	19.17	0.01	19.15	0.02	18.91	0.01
M005147.15+174710.3	1367.5	<17.9	<16.1	-	-	NOT		
J005147.15+174710.4	12.9464982	17.786248	15.59	0.04	14.65	0.06	11.42	0.19
PSO J012.9465+17.7863	5	49	21.17	0.02	20.3	0.01	19.69	0.02
M010549.69+184507.1	339.5	<16.6	<15.2	-	-	NOT		
J010549.66+184506.6	16.4569295	18.7518446	15.61	0.04	14.81	0.06	11.66	0.20
PSO J016.4569+18.7521	5	69	20.21	0.02	19.7	0.02	19.56	0.01
M055341.91-084003.3	273.8	<19.3	<13.9	-	-	SALT		
J055341.91-084002.4	88.4246476	-8.6673536	15.78	0.05	14.75	0.07	11.55	0.18
PSO J088.4246-08.6672	20	0	23.21	0.16	22.04	0.08	21.15	0.03
M082444.81-102943.6	345.4	<16.0	<15.5	-	-	SUGAR		
J082444.78-102943.4	126.1866017	-10.4954068	15.42	0.04	14.70	0.06	11.28	0.16
PSO J126.1867-10.4951	5	82	18.72	0.01	18.36	0.01	18.23	0.01
M085838.19+093745.2	421.5	<17.7	<17.3	-	-	SALT		
J085838.21+093745.8	134.6592162	9.6293919	15.94	0.06	14.86	0.07	11.6	0.21
PSO J134.6591+09.6292	5	59	20.79	0.04	20.29	0.03	19.79	0.02
M110125.00-212429.4	215.3	<17.5	<14.0	-	-	SALT		
J110125.01-212429.6	165.3542383	-21.4082386	16.21	0.06	15.52	0.116	11.95	-

Table 3 *continued*

**Table 3** (*continued*)

NVSS-ID	Flux	$B_{maj}$	$B_{min}$	$B_{pa}$	Redshift	Telescope	AGN-type	
WISE-ID	$R_{Aw}$	$Dec_W$	W1	$\delta W1$	W2	$\delta W2$	W3	$\delta W3$
PS1-ID	nStackDets	nDetections	g	$\delta g$	r	$\delta r$	i	$\delta i$
(1)	(2)	(3)	(4)	(5)	(6)	(7)	(8)	
(9)	(10)	(11)	(12)	(13)	(14)	(15)	(16)	(17)
(18)	(19)	(20)	(21)	(22)	(23)	(24)	(25)	(26)
(18)	(19)	(20)	(21)	(22)	(23)	(24)	(25)	(26)
(18)	(19)	(20)	(21)	(22)	(23)	(24)	(25)	(26)
M111457.57-051721.4	PSO J165.3542-21.4083	31	7	-21.61	0.05	21.41	0.04	20.98
	J111457.53-051721.8	325.7	<17.3	<14.3	-	-	SALT	0.04
		168.7397484	-5.2893949	17.81	0.23	16.06	0.20	11.96
		-	-	-	-	-	-	0.31
M112712.45-073512.7	459.5	14.6	<17.6	57.9	-	-	-	-
	J112712.40-073512.2	171.8016899	-7.5867435	14.8	0.03	14.03	0.04	10.96
	PSO J171.8018-07.5867	10	40	21.35	0.09	20.97	0.11	20.76
M120746.68-133201.0	203.2	<17.7	<17.1	-	-	SALT	-	0.11
	J120746.69-133200.3	181.9445650	-13.5334438	17.34	0.16	16.42	0.26	12.08
	PSO J181.9446-13.5335	5	37	21.14	0.07	20.6	0.1	20.48
M121157.77-192607.5	479.8	14.0	<17.2	63.2	-	SALT	-	0.11
	J121157.73-192607.7	182.9905819	-19.4354923	15.89	0.05	15.1	0.08	11.89
	PSO J182.9906-19.4355	5	39	-999	-999	21.47	0.05	20.67
M124553.81-161645.2	516.2	<17.2	<16.7	-	-	SALT	-	0.05
	J124553.74-161645.7	191.4739578	-16.2793658	15.13	0.04	13.99	0.04	10.56
	PSO J191.4739-16.2794	5	66	20.66	0.05	20.2	0.05	20.03
M130508.50-285042.0	328.4	<17.0	<15.8	-	-	SALT	-	0.05
	J130508.44-285041.8	196.2851755	-28.8449497	16.05	0.05	15.05	0.07	11.81
	PSO J196.2853-28.8450	5	7	22.15	0.07	21.69	0.18	-999
M131403.21+084209.5	267.1	<16.6	<16.3	-	-	SALT	-	0.21
	J131403.18+084209.2	198.5132651	8.7025622	15.72	0.04	14.73	0.06	11.62
	PSO J198.5133+08.7025	5	36	21.55	0.06	21.21	0.05	20.35
M135547.91-094756.5	322.7	<19.0	<15.9	-	-	SALT	-	0.18
	J135547.87-094754.7	208.9494924	-9.7985281	17.72	0.21	16.35	0.25	12.33
	PSO J208.9406-09.7987	5	38	21.73	0.05	21.4	0.03	21.06
M162422.33-301252.0	282.6	<15.5	<14.1	-	-	SALT	-	0.06
	J162422.36-301251.8	246.0931921	-30.2143945	15.56	0.05	14.59	0.06	11.48
	-	-	-	-	-	-	-	0.18

GUPTA ET AL.

Table 3 *continued*

Table 3 (*continued*)

Table 3 *continued*

Table 3 (continued)

NVSS-ID	Flux	$B_{maj}$	$B_{min}$	$B_{pa}$	Redshift	Telescope	AGN-type	
WISE-ID	$R_{Aw}$	$Dec_W$	W1	$\delta W1$	W2	$\delta W2$	W3	$\delta W3$
PS1-ID	nStackDets	nDetections	g	$\delta g$	r	$\delta r$	i	$\delta i$
(1)	(2)	(3)	(4)	(5)	(6)	(7)	(8)	
(9)	(10)	(11)	(12)	(13)	(14)	(15)	(16)	(17)
(18)	(19)	(20)	(21)	(22)	(23)	(24)	(25)	(26)
(18)	(19)	(20)	(21)	(22)	(23)	(24)	(25)	(26)
(18)	(19)	(20)	(21)	(22)	(23)	(24)	(25)	(26)
J010253.22-120541.2	15.7217535	-12.0948007	16.76	0.10	16.04	0.20	11.99	-
PSO J015.7218-12.0948	1	0	22.99	0.17	23.25	0.16	22.82	0.13
M012156.62-265747.8	244	<18.2	<17.7	-	-	SALT	-	-
J012156.60-265747.7	20.485842	-26.9632715	16.75	0.09	15.68	0.12	11.89	-
M051700.70+071225.2	203.4	<16.3	<14.9	-	-	SALT	-	-
J051700.70+071225.3	79.2529287	7.2070517	16.44	0.08	15.33	0.10	11.6	-
PSO J079.2529+07.2070	3	0	23.54	0.31	22.31	0.09	21.99	0.08
M064255.16-325917.6	240.6	<18.7	<16.2	-	-	SALT	-	-
J064255.14-325918.2	100.7297545	-32.9883921	16.17	0.05	14.86	0.05	11.19	0.11
M084548.34-111800.1	264.4	<16.6	<16.4	-	-	SUGAR	-	-
J084548.25-111801.7	131.4510672	-11.300489	16.18	0.06	15.29	0.09	12.03	0.30
PSO J131.4512-11.3001	0	0	23.88	0.85	23.26	0.30	23.2	0.15
M095414.75+125222.6	355.7	<17.3	<16.2	-	-	NOT	-	-
J095414.78+125222.5	148.5616137	12.8729286	16.95	0.13	15.74	0.143	11.79	-
M095903.16-023604.5	269.1	<19.1	<16.6	-	-	SALT	-	-
J095903.12-023604.5	149.7630038	-2.6012773	16.75	0.10	15.61	0.129	12.12	-
M101448.67-294433.7	229	<16.8	<14.7	-	-	SALT	-	-
J101448.55-294433.5	153.7023142	-29.7426467	16.19	0.06	15.41	0.09	12.35	-
M101730.54-384643.7	336.5	<18.7	<17.0	-	-	SALT	-	-
J101730.47-384643.8	154.3769644	-38.7788386	16.41	0.07	15.57	0.11	11.92	0.25
M101838.68-222502.4	288.1	<17.9	<16.9	-	-	SALT	-	-
J101838.61-222501.9	154.6608814	-22.4172125	16.29	0.06	15.43	0.10	11.91	-

GUPTA ET AL.

Table 3 (continued)

NVSS-ID	Flux	$B_{maj}$	$B_{min}$	$B_{pa}$	Redshift	Telescope	AGN-type	
WISE-ID	$R_{Aw}$	$Dec_W$	W1	$\delta W1$	W2	$\delta W2$	W3	$\delta W3$
PS1-ID	nStackDets	nDetections	g	$\delta g$	r	$\delta r$	i	$\delta i$
(1)	(2)	(3)	(4)	(5)	(6)	(7)	(8)	
(9)	(10)	(11)	(12)	(13)	(14)	(15)	(16)	(17)
(18)	(19)	(20)	(21)	(22)	(23)	(24)	(25)	(26)
(27)	(28)	(29)	(30)					
M104015.57+062747.0	600.4	< 18.4	< 16.7	-	-	-	-	-
J104015.61+062745.9	160.0650746	6.4627552	17.32	0.17	16.42	0.273	11.96	-
-	-	-	-	-	-	-	-	-
M110552.25-015628.1	477.5	26.6	< 16.8	-76.3	-	SALT	-	-
J110552.18-015627.1	166.4674275	-1.9408789	15.49	0.04	14.45	0.05	10.73	0.101
PSO J166.4675-01.9408	11	1	22.29	0.07	22.10	0.07	21.61	0.08
M114450.43-145502.7	444	14.4	< 16.9	57.1	-	SALT	-	-
J114450.42-145501.9	176.2100931	-14.9171983	16.05	0.06	15.45	0.137	12.27	-
PSO J176.2101-14.9172	3	0	23.45	0.25	23.01	0.12	22.09	0.07
M115855.44-170524.7	359.5	48.1	< 16.6	75.2	-	SALT	-	-
J115855.44-170523.7	179.7310087	-17.0899371	16.41	0.07	15.40	0.12	12.10	0.42
PSO J179.7312-17.0901	2	1	22.74	0.15	22.47	0.11	23.14	0.32
M121128.51-351003.4	280.1	< 16.4	< 15.3	-	-	SALT	-	-
J121128.44-351002.5	182.8685401	-35.1673751	14.9	0.03	14.17	0.041	11.25	0.14
-	-	-	-	-	-	-	-	-
M125203.09-040638.5	392.6	< 18.7	< 16.5	-	-	SALT	-	-
J125203.15-040638.4	193.01315	-4.1106828	16.69	0.09	16.02	0.19	12.45	-
-	-	-	-	-	-	-	-	-
M131615.50-242824.1	234.7	< 15.9	< 15.3	-	-	SALT	-	-
J131615.51-242822.8	199.0646338	-24.4730071	16.56	0.07	15.90	0.14	12.50	0.36
PSO J199.0646-24.4733	0	0	22.77	0.13	22.61	0.13	22.51	0.13
M133621.59-105243.4	397.3	14.7	< 16.7	50.5	-	SALT	-	-
J133621.66-105243.7	204.090252	-10.8788322	17.43	0.16	16.43	0.23	12.44	-
-	-	-	-	-	-	-	-	-
M135150.53-243921.3	225.5	< 18.0	< 15.7	-	-	SALT	-	-
J135150.35-243920.1	207.9598266	-24.6555845	16.05	0.06	15.3	0.10	12.27	-
PSO J207.9601-24.6557	1	0	25.19	1.32	23.24	0.26	22.39	0.18
							21.28	0.08
							20.97	0.16

Table 3 continued

**Table 3** (*continued*)

NVSS-ID	Flux	$B_{maj}$	$B_{min}$	$B_{pa}$	Redshift	Telescope	AGN-type
WISE-ID	$R_{Aw}$	$Dec_W$	W1	$\delta W1$	W2	$\delta W2$	W3
PS1-ID	nStackDets	nDetections	g	$\delta g$	r	$\delta r$	i
(1)	(2)	(3)	(4)	(5)	(6)	(7)	(8)
(9)	(10)	(11)	(12)	(13)	(14)	(15)	(16)
(18)	(19)	(20)	(21)	(22)	(23)	(24)	(25)
(30)							
M140807.52+095348.1	261.9	< 18.7	< 15.3	-	-	SALT	
	J140807.50+095347.6	212.031289	9.8965777	16.27	0.06	15.43	0.10
	PSO J212.0314+09.8964	1	0	25.18	1.30	25.19	1.11
M152601.27+071525.5	288.2	< 16.4	< 14.7	-	-	SALT	
	J152601.29+071525.2	231.5053995	7.2570161	17.42	0.14	16.46	0.23
	PSO J231.5054+07.2570	0	0	25.64	1.55	23.43	0.29
M154044.18-145528.3	313.1	< 16.9	< 16.1	-	-	SALT	
	J154044.17-145529.7	235.1840445	-14.9249201	16.94	0.13	16.12	0.24
	-	-	-	-	-	-	-
M164548.19-121024.8	386.1	< 16.6	< 16.0	-	-	SALT	
	J164548.18-121025.3	251.4507554	-12.1736957	16.46	0.09	15.59	0.13
	PSO J251.4509-12.1734	2	0	25.70	1.61	23.29	0.24
M195302.23-203633.0	516.4	< 18.6	< 17.0	-	-	SALT	
	J195302.24-203631.7	298.2593374	-20.6088241	16.68	0.10	15.61	0.17
	-	-	-	-	-	-	-
M204439.43-182852.2	219.5	< 17.7	< 16.5	-	-	SALT	
	J204439.40-182851.4	311.1641793	-18.4809453	16.42	0.08	15.38	0.107
	PSO J311.1644-18.4812	4	0	-999.0	-999.0	22.63	0.10
M211410.44-105558.3	280.3	< 17.5	< 16.1	-	-	SALT	
	J211410.40-105557.6	318.5433725	-10.93268	16.51	0.09	15.76	0.16
	PSO J318.5431-10.9326	0	0	-999.0	0.65	24.06	0.67
M225813.47-095817.2	225.7	< 19.7	< 16.5	-	-	SUGAR	
	J225813.45-095816.7	344.5560625	-9.9713208	17.37	0.17	16.52	0.34
	-	-	-	-	-	-	-

Table 3 *continued*

Table 3 (*continued*)

NVSS-ID	Flux	$B_{maj}$	$B_{min}$	$B_{pa}$	Redshift	Telescope	AGN-type	
WISE-ID	$R_{Aw}$	$Dec_W$	W1	$\delta W1$	W2	$\delta W2$	W3	$\delta W3$
PS1-ID	nStackDets	nDetections	g	$\delta g$	r	$\delta r$	i	$\delta i$
(1)	(2)	(3)	(4)	(5)	(6)	(7)	(8)	
(9)	(10)	(11)	(12)	(13)	(14)	(15)	(16)	(17)
(18)	(19)	(20)	(21)	(22)	(23)	(24)	(25)	(26)
							(27)	(28)
							(29)	(30)

NOTE— Column 1: NVSS ID based on Right Ascension and Declination (J2000); M stands for MALS SALT-NOT survey. Column 2: 20 cm flux density from NVSS. Columns 3 - 5: deconvolved radio sources size from NVSS (major and minor axes in arcseconds, and position angle in degrees). Column 6: spectroscopic redshift based on SALT-NOT spectra. Column 7: telescope used for spectroscopy. SUGAR = observed with both SALT and NOT. Column 8: AGN-type (G or Q corresponds to narrow or broad line AGN). Columns 9 - 17 : WISE ID and W1, W2 and W3 magnitudes (mag) with errors. Column 18 - 30: PS1 ID, number of stack detections, number of single epoch detections in all filters, and g, r, i, z and y magnitudes with errors from PS1-mean for sources with redshifts and ELLs, and PS1-stack for DFs.

List of targets excluded from the NOT sample presented in Table 1 of Krogager et al. (2018): M024944.50+123706.3, M051938.34+174641.2, M163906.46+114409.2, M162303.03+123958.4, M060012.92-071037.9, M162539.34-041616.3 and M172423.07+032632.5 (see also Section 2.2).

## B. NOTES ON INDIVIDUAL TARGETS

Here we briefly summarize the properties of interesting individual targets relevant to discussions in Sections 5.2 to 5.5.

### B.1. AGN at $z < 0.5$

1. M0314-0909 ( $z_{\text{em}} = 0.312$ ) and M1024-0852 ( $z_{\text{em}} = 0.455$ ): The associated radio emission has projected linear sizes of  $240 - 250$  kpc.
2. M0133-0256 ( $z_{\text{em}} = 0.259$ ) and M1703+0645 ( $z_{\text{em}} = 0.399$ ): These show double peaked emission lines. For the former, the AGN host also shows signs of interaction with a nearby galaxy.
3. J0609+0217 ( $z_{\text{em}} = 0.174$ ) and M1219-1809 ( $z_{\text{em}} = 0.189$ ): The host galaxies are part of an interacting group of galaxies.

### B.2. AGN at $0.5 < z < 1.0$

1. M0909-3133 ( $z_{\text{em}} = 0.884$ ): The radio emission associated with this NLAGN has an extent of 330 kpc. The optical spectrum is shown in Fig. 5).
2. M2220+1307 ( $z_{\text{em}} = 0.760$ ): The projected linear size of radio emission associated with this BLAGN is 180 kpc.
3. M1440+0531, M2058-1736 and M2059-1440: These have distorted radio morphologies suggesting interaction with the ambient medium.

### B.3. AGN at $1.0 < z < 1.9$

1. M0552-3459 ( $z_{\text{em}} = 1.776$ ): This NLAGN has clear detections of He II, C III], C II] and Ne IV (see Fig. 5). The FWHM measured based on the C III] emission line is  $835 \text{ km s}^{-1}$ . At 3 GHz, the associated radio emission is resolved into two lobes separated by  $8.3''$ (71 kpc).
2. M1033-1210 ( $z_{\text{em}} = 1.328$ ): Krogager et al. (2018) identified this as a NLAGN based on the presence of narrow [O II] line and the absence of broad emission lines like Mg II and C III]. In this case too the radio emission is resolved into a double lobed morphology with a separation of  $3.2''$ (28 kpc).
3. M0956-1317 ( $z_{\text{em}} = 1.198$ ): The associated radio emission has an extent of  $23.3''$ (194 kpc), which

is the largest in our sample among the AGN at  $1.0 < z < 1.9$ .

### B.4. AGN at $1.9 < z < 3.5$

1. M0516+0732 ( $z_{\text{em}} = 2.594$ ): The radio emission associated with this NLAGN is compact with a deconvolved size of  $< 0.5''$ , i.e.,  $< 4$  kpc. It also shows strong continuum emission in the optical spectrum. The C IV emission profile may be affected by the associated absorption. We measure the Ly $\alpha$  to C IV emission line ratio,  $f_{\text{Ly}\alpha}/f_{\text{C IV}} = 2.40 \pm 0.10$ . This is similar to the ratios observed in high- $z$  radio galaxies.
2. M1315-2745 ( $z_{\text{em}} = 1.911$ ): The radio emission associated with this NLAGN exhibits a double-lobed morphology with an extent of  $32.8''$ (280 kpc). We detect emission lines of C IV, He II, C III], C II] and Ne IV. The optical continuum emission is very weak. While we do not clearly detect the AGN in PS1 images, it is clearly seen in the WISE image. The deconvolved velocity width of the C IV emission line is  $375 \text{ km s}^{-1}$ . The ratio  $f_{\text{C IV}}/f_{\text{He II}}$  is found to be  $1.88 \pm 0.34$ . This is typical of ratios observed in high- $z$  radio galaxies (see for example figure 6 of Shukla et al. 2021a, and references therein) but more than what is seen in typical quasars.
3. M1455-0957 ( $z_{\text{em}} = 1.995$ ): The double-lobed radio emission associated with this NLAGN has an extent of  $8.1''$ (i.e., 69 kpc). The optical and IR characteristics are also very similar to M1315-2745. The C IV, He II, C III], C II] and Ne IV emission lines are clearly detected. The deconvolved velocity width of the C IV emission line is  $430 \text{ km s}^{-1}$ . We estimate  $f_{\text{C IV}}/f_{\text{He II}} = 0.69 \pm 0.14$ , which is again typical of the ratios observed in high- $z$  radio galaxies.
4. M1513-2524 ( $z_{\text{em}} = 3.132$ ): This NLAGN is associated with a double-lobed radio emission with an extent of  $23.7''$  (184 kpc). It exhibits extended Ly $\alpha$ , C IV and He II emission. The detailed analysis of this object is presented by Shukla et al. (2021a).

## REFERENCES

- Assef, R. J., Kochanek, C. S., Brodwin, M., et al. 2010, ApJ, 713, 970, doi: [10.1088/0004-637X/713/2/970](https://doi.org/10.1088/0004-637X/713/2/970)
- Balashev, S. A., & Noterdaeme, P. 2018, MNRAS, 478, L7, doi: [10.1093/mnrasl/sly067](https://doi.org/10.1093/mnrasl/sly067)
- Ballet, J., Burnett, T. H., Digel, S. W., & Lott, B. 2020, arXiv e-prints, arXiv:2005.11208. <https://arxiv.org/abs/2005.11208>
- Barrows, R. S., Comerford, J. M., Stern, D., & Assef, R. J. 2021, arXiv e-prints, arXiv:2107.02815. <https://arxiv.org/abs/2107.02815>
- Becker, R. H., White, R. L., Gregg, M. D., et al. 2000, ApJ, 538, 72, doi: [10.1086/309099](https://doi.org/10.1086/309099)
- Becker, R. H., White, R. L., & Helfand, D. J. 1995, ApJ, 450, 559, doi: [10.1086/176166](https://doi.org/10.1086/176166)
- Boettcher, E., Chen, H.-W., Zahedy, F. S., et al. 2021, ApJ, 913, 18, doi: [10.3847/1538-4357/abf0a0](https://doi.org/10.3847/1538-4357/abf0a0)
- Burgh, E. B., Nordsieck, K. H., Kobulnicky, H. A., et al. 2003, in Society of Photo-Optical Instrumentation Engineers (SPIE) Conference Series, Vol. 4841, Proc. SPIE, ed. M. Iye & A. F. M. Moorwood, 1463–1471
- Chambers, K. C., Magnier, E. A., Metcalfe, N., et al. 2016, arXiv e-prints, arXiv:1612.05560. <https://arxiv.org/abs/1612.05560>
- Chang, Y. L., Arsioli, B., Giommi, P., & Padovani, P. 2017, A&A, 598, A17, doi: [10.1051/0004-6361/201629487](https://doi.org/10.1051/0004-6361/201629487)
- Coatman, L., Hewett, P. C., Banerji, M., & Richards, G. T. 2016, MNRAS, 461, 647, doi: [10.1093/mnras/stw1360](https://doi.org/10.1093/mnras/stw1360)
- Combes, F., Gupta, N., Muller, S., et al. 2021, arXiv e-prints, arXiv:2101.00188. <https://arxiv.org/abs/2101.00188>
- Condon, J. J., Cotton, W. D., Greisen, E. W., et al. 1998, AJ, 115, 1693, doi: [10.1086/300337](https://doi.org/10.1086/300337)
- Crawford, S. M., Still, M., Schellart, P., et al. 2010, in Proc. SPIE, Vol. 7737, Observatory Operations: Strategies, Processes, and Systems III, 773725
- Cutri, R. M., & et al. 2014, VizieR Online Data Catalog, II/328
- D'Abrusco, R., Álvarez Crespo, N., Massaro, F., et al. 2019, ApJS, 242, 4, doi: [10.3847/1538-4365/ab16f4](https://doi.org/10.3847/1538-4365/ab16f4)
- Denney, K. D., Peterson, B. M., Pogge, R. W., et al. 2010, ApJ, 721, 715, doi: [10.1088/0004-637X/721/1/715](https://doi.org/10.1088/0004-637X/721/1/715)
- Ellison, S. L., Yan, L., Hook, I. M., et al. 2001, A&A, 379, 393, doi: [10.1051/0004-6361:20011281](https://doi.org/10.1051/0004-6361:20011281)
- Ellison, S. L., York, B. A., Pettini, M., & Kanekar, N. 2008, MNRAS, 388, 1349, doi: [10.1111/j.1365-2966.2008.13482.x](https://doi.org/10.1111/j.1365-2966.2008.13482.x)
- Fabian, A. C. 2012, ARA&A, 50, 455, doi: [10.1146/annurev-astro-081811-125521](https://doi.org/10.1146/annurev-astro-081811-125521)
- Frank, S., & Péroux, C. 2010, MNRAS, 406, 2235, doi: [10.1111/j.1365-2966.2010.16848.x](https://doi.org/10.1111/j.1365-2966.2010.16848.x)
- Ghisellini, G., Celotti, A., Tavecchio, F., Haardt, F., & Sbarro, T. 2014, MNRAS, 438, 2694, doi: [10.1093/mnras/stt2394](https://doi.org/10.1093/mnras/stt2394)
- Gupta, N., Srianand, R., & Saikia, D. J. 2005, MNRAS, 361, 451, doi: [10.1111/j.1365-2966.2005.09169.x](https://doi.org/10.1111/j.1365-2966.2005.09169.x)
- Gupta, N., Srianand, R., Baan, W., et al. 2017, ArXiv e-prints. <https://arxiv.org/abs/1708.07371>
- Gupta, N., Jagannathan, P., Srianand, R., et al. 2021a, ApJ, 907, 11, doi: [10.3847/1538-4357/abcb85](https://doi.org/10.3847/1538-4357/abcb85)
- Gupta, N., Srianand, R., Shukla, G., et al. 2021b, arXiv e-prints, arXiv:2103.09437. <https://arxiv.org/abs/2103.09437>
- Heckman, T. M., & Best, P. N. 2014, ARA&A, 52, 589, doi: [10.1146/annurev-astro-081913-035722](https://doi.org/10.1146/annurev-astro-081913-035722)
- Hickox, R. C., & Alexander, D. M. 2018, ARA&A, 56, 625, doi: [10.1146/annurev-astro-081817-051803](https://doi.org/10.1146/annurev-astro-081817-051803)
- Jauncey, D. L., Reynolds, J. E., Tzioumis, A. K., et al. 1991, Nature, 352, 132, doi: [10.1038/352132a0](https://doi.org/10.1038/352132a0)
- Jonas, J., & MeerKAT Team. 2016, in Proceedings of MeerKAT Science: On the Pathway to the SKA. 25–27 May, 2016 Stellenbosch, South Africa (MeerKAT2016), 1
- Kapahi, V. K., Athreya, R. M., van Breugel, W., McCarthy, P. J., & Subrahmanyam, C. R. 1998, ApJS, 118, 275, doi: [10.1086/313144](https://doi.org/10.1086/313144)
- Kaspi, S., Smith, P. S., Netzer, H., et al. 2000, ApJ, 533, 631, doi: [10.1086/308704](https://doi.org/10.1086/308704)
- Kobulnicky, H. A., Nordsieck, K. H., Burgh, E. B., et al. 2003, in Society of Photo-Optical Instrumentation Engineers (SPIE) Conference Series, Vol. 4841, Proc. SPIE, ed. M. Iye & A. F. M. Moorwood, 1634–1644
- Krogager, J.-K., Fynbo, J. P. U., Møller, P., et al. 2019, MNRAS, 486, 4377, doi: [10.1093/mnras/stz1120](https://doi.org/10.1093/mnras/stz1120)
- Krogager, J. K., Gupta, N., Noterdaeme, P., et al. 2018, ApJS, 235, 10, doi: [10.3847/1538-4365/aaab51](https://doi.org/10.3847/1538-4365/aaab51)
- Lacy, M., Storrie-Lombardi, L. J., Sajina, A., et al. 2004, ApJS, 154, 166, doi: [10.1086/422816](https://doi.org/10.1086/422816)
- Lacy, M., Baum, S. A., Chandler, C. J., et al. 2020, PASP, 132, 035001, doi: [10.1088/1538-3873/ab63eb](https://doi.org/10.1088/1538-3873/ab63eb)
- Laor, A. 2000, ApJ, 543, L111, doi: [10.1086/317280](https://doi.org/10.1086/317280)
- Ledoux, C., Petitjean, P., & Srianand, R. 2003, MNRAS, 346, 209, doi: [10.1046/j.1365-2966.2003.07082.x](https://doi.org/10.1046/j.1365-2966.2003.07082.x)
- Liu, X., Shen, Y., Strauss, M. A., & Greene, J. E. 2010, ApJ, 708, 427, doi: [10.1088/0004-637X/708/1/427](https://doi.org/10.1088/0004-637X/708/1/427)
- Lu, Y., Wang, T., Zhou, H., & Wu, J. 2007, AJ, 133, 1615, doi: [10.1086/512034](https://doi.org/10.1086/512034)
- Masci, F. J., Laher, R. R., Rusholme, B., et al. 2019, PASP, 131, 018003, doi: [10.1088/1538-3873/aae8ac](https://doi.org/10.1088/1538-3873/aae8ac)
- Massaro, E., Giommi, P., Leto, C., et al. 2009, A&A, 495, 691, doi: [10.1051/0004-6361:200810161](https://doi.org/10.1051/0004-6361:200810161)

- Mateos, S., Alonso-Herrero, A., Carrera, F. J., et al. 2012, MNRAS, 426, 3271, doi: [10.1111/j.1365-2966.2012.21843.x](https://doi.org/10.1111/j.1365-2966.2012.21843.x)
- Mathur, S., & Nair, S. 1997, ApJ, 484, 140, doi: [10.1086/304327](https://doi.org/10.1086/304327)
- Mauch, T., Murphy, T., Buttery, H. J., et al. 2003, MNRAS, 342, 1117, doi: [10.1046/j.1365-8711.2003.06605.x](https://doi.org/10.1046/j.1365-8711.2003.06605.x)
- McConnell, D., Hale, C. L., Lenc, E., et al. 2020, PASA, 37, e048, doi: [10.1017/pasa.2020.41](https://doi.org/10.1017/pasa.2020.41)
- Mullaney, J. R., Alexander, D. M., Fine, S., et al. 2013, MNRAS, 433, 622, doi: [10.1093/mnras/stt751](https://doi.org/10.1093/mnras/stt751)
- Murphy, M. T., & Liske, J. 2004, MNRAS, 354, L31, doi: [10.1111/j.1365-2966.2004.08374.x](https://doi.org/10.1111/j.1365-2966.2004.08374.x)
- Muzahid, S., Srianand, R., & Charlton, J. 2015, MNRAS, 448, 2840, doi: [10.1093/mnras/stv133](https://doi.org/10.1093/mnras/stv133)
- Nandra, K., George, I. M., Mushotzky, R. F., Turner, T. J., & Yaqoob, T. 1997, ApJ, 476, 70, doi: [10.1086/303600](https://doi.org/10.1086/303600)
- Netzer, H., Lutz, D., Schweitzer, M., et al. 2007, ApJ, 666, 806, doi: [10.1086/520716](https://doi.org/10.1086/520716)
- Noterdaeme, P., Ledoux, C., Petitjean, P., & Srianand, R. 2008, A&A, 481, 327, doi: [10.1051/0004-6361:20078780](https://doi.org/10.1051/0004-6361:20078780)
- Noterdaeme, P., Petitjean, P., Ledoux, C., & Srianand, R. 2009, A&A, 505, 1087, doi: [10.1051/0004-6361/200912768](https://doi.org/10.1051/0004-6361/200912768)
- Noterdaeme, P., Srianand, R., Rahmani, H., et al. 2015, A&A, 577, A24, doi: [10.1051/0004-6361/201425376](https://doi.org/10.1051/0004-6361/201425376)
- Onken, C. A., Ferrarese, L., Merritt, D., et al. 2004, ApJ, 615, 645, doi: [10.1086/424655](https://doi.org/10.1086/424655)
- Padovani, P., Alexander, D. M., Assef, R. J., et al. 2017, A&A Rev., 25, 2, doi: [10.1007/s00159-017-0102-9](https://doi.org/10.1007/s00159-017-0102-9)
- Parks, D., Prochaska, J. X., Dong, S., & Cai, Z. 2018, MNRAS, 476, 1151, doi: [10.1093/mnras/sty196](https://doi.org/10.1093/mnras/sty196)
- Pei, Y. C., Fall, S. M., & Bechtold, J. 1991, ApJ, 378, 6, doi: [10.1086/170401](https://doi.org/10.1086/170401)
- Petitjean, P., Srianand, R., & Ledoux, C. 2000, A&A, 364, L26
- Planck Collaboration, Aghanim, N., Akrami, Y., et al. 2020, A&A, 641, A6, doi: [10.1051/0004-6361/201833910](https://doi.org/10.1051/0004-6361/201833910)
- Pontzen, A., & Pettini, M. 2009, MNRAS, 393, 557, doi: [10.1111/j.1365-2966.2008.14193.x](https://doi.org/10.1111/j.1365-2966.2008.14193.x)
- Pramesh Rao, A., & Subrahmanyam, R. 1988, MNRAS, 231, 229, doi: [10.1093/mnras/231.2.229](https://doi.org/10.1093/mnras/231.2.229)
- Rector, T. A., & Stocke, J. T. 2001a, AJ, 122, 565, doi: [10.1086/321179](https://doi.org/10.1086/321179)
- . 2001b, AJ, 122, 565, doi: [10.1086/321179](https://doi.org/10.1086/321179)
- Richards, G. T., Fan, X., Newberg, H. J., et al. 2002, AJ, 123, 2945, doi: [10.1086/340187](https://doi.org/10.1086/340187)
- Richards, G. T., Lacy, M., Storrie-Lombardi, L. J., et al. 2006, ApJS, 166, 470, doi: [10.1086/506525](https://doi.org/10.1086/506525)
- Sanders, D. B., & Mirabel, I. F. 1996, ARA&A, 34, 749, doi: [10.1146/annurev.astro.34.1.749](https://doi.org/10.1146/annurev.astro.34.1.749)
- Satyapal, S., Secrest, N. J., Ricci, C., et al. 2017, ApJ, 848, 126, doi: [10.3847/1538-4357/aa88ca](https://doi.org/10.3847/1538-4357/aa88ca)
- Shankar, F., Dai, X., & Sivakoff, G. R. 2008, ApJ, 687, 859, doi: [10.1086/591488](https://doi.org/10.1086/591488)
- Shen, Y., Richards, G. T., Strauss, M. A., et al. 2011, ApJS, 194, 45, doi: [10.1088/0067-0049/194/2/45](https://doi.org/10.1088/0067-0049/194/2/45)
- Shukla, G., Srianand, R., Gupta, N., et al. 2021a, MNRAS, 501, 5362, doi: [10.1093/mnras/staa3977](https://doi.org/10.1093/mnras/staa3977)
- . 2021b, arXiv e-prints, arXiv:2109.00576. <https://arxiv.org/abs/2109.00576>
- Sikora, M., & Begelman, M. C. 2013, ApJ, 764, L24, doi: [10.1088/2041-8205/764/2/L24](https://doi.org/10.1088/2041-8205/764/2/L24)
- Sikora, M., Stawarz, L., & Lasota, J.-P. 2007, ApJ, 658, 815, doi: [10.1086/511972](https://doi.org/10.1086/511972)
- Srianand, R., Gupta, N., Petitjean, P., et al. 2012, MNRAS, 421, 651, doi: [10.1111/j.1365-2966.2011.20342.x](https://doi.org/10.1111/j.1365-2966.2011.20342.x)
- Srianand, R., & Kembhavi, A. 1997, ApJ, 478, 70, doi: [10.1086/303764](https://doi.org/10.1086/303764)
- Stern, D., Eisenhardt, P., Gorjian, V., et al. 2005, ApJ, 631, 163, doi: [10.1086/432523](https://doi.org/10.1086/432523)
- Stern, D., Assef, R. J., Benford, D. J., et al. 2012, ApJ, 753, 30, doi: [10.1088/0004-637X/753/1/30](https://doi.org/10.1088/0004-637X/753/1/30)
- Stickel, M., Padovani, P., Urry, C. M., Fried, J. W., & Kuehr, H. 1991, ApJ, 374, 431, doi: [10.1086/170133](https://doi.org/10.1086/170133)
- Taylor, A. R., Stil, J. M., & Sunstrum, C. 2009, ApJ, 702, 1230, doi: [10.1088/0004-637X/702/2/1230](https://doi.org/10.1088/0004-637X/702/2/1230)
- Urry, C. M., & Padovani, P. 1995, PASP, 107, 803, doi: [10.1086/133630](https://doi.org/10.1086/133630)
- Vaughan, S., Edelson, R., Warwick, R. S., & Uttley, P. 2003, MNRAS, 345, 1271, doi: [10.1046/j.1365-2966.2003.07042.x](https://doi.org/10.1046/j.1365-2966.2003.07042.x)
- Vestergaard, M., & Peterson, B. M. 2006, ApJ, 641, 689, doi: [10.1086/500572](https://doi.org/10.1086/500572)
- Waters, C. Z., Magnier, E. A., Price, P. A., et al. 2020, ApJS, 251, 4, doi: [10.3847/1538-4365/abb82b](https://doi.org/10.3847/1538-4365/abb82b)
- Wiklind, T., & Combes, F. 1996, Nature, 379, 139, doi: [10.1038/379139a0](https://doi.org/10.1038/379139a0)
- Wolfe, A. M., Gawiser, E., & Prochaska, J. X. 2005, ARA&A, 43, 861
- Wolfe, A. M., & Prochaska, J. X. 2000, ApJ, 545, 591, doi: [10.1086/317860](https://doi.org/10.1086/317860)
- Wright, E. L., Eisenhardt, P. R. M., Mainzer, A. K., et al. 2010, AJ, 140, 1868, doi: [10.1088/0004-6256/140/6/1868](https://doi.org/10.1088/0004-6256/140/6/1868)
- Zahedy, F. S., Chen, H.-W., Boettcher, E., et al. 2020, ApJ, 904, L10, doi: [10.3847/2041-8213/abc48d](https://doi.org/10.3847/2041-8213/abc48d)